SOFT TISSUE HYPERELASTIC PARAMETER RECONSTRUCTION FOR BREAST CANCER ASSESSMENT

(Spine title: Soft Tissue Hyperelastic Parameter Reconstruction)

(Thesis format: Monograph)

by

Hatef Mehrabian

Graduate Program in Engineering Science
Department of Electrical and Computer Engineering

A thesis submitted in partial fulfillment of
the requirements for the degree of Master
of Engineering Science

The School of Graduate and Postdoctoral Studies
The University of Western Ontario
London, Ontario, Canada

THE UNIVERSITY OF WESTERN ONTARIO

SCHOOL OF GRADUATE AND POSTDOCTORAL STUDIES

CERTIFICATE OF EXAMINATION

Supervisor	Examiners
Dr. Abbas Samani	David Holdsworth
	Kenneth McIsaac
	Shaun Salisbury

The thesis by

Hatef Mehrabian

entitled:

Soft Tissue Hyperelastic Parameter Reconstruction Technique for Breast Cancer Assessment

is accepted in partial fulfillment of the

requirements for the degree of

Master of Engineering Science

Date_____ _____

Chair of the Thesis Examination Board

Abstract

In breast elastography, breast tissues usually undergo large compressions resulting in significant geometric and structural changes, and consequently nonlinear mechanical behavior. In this study, an elastography technique is presented where parameters characterizing tissue nonlinear behavior is reconstructed. Such parameters can be used for tumor tissue classification. To model their nonlinear mechanical behavior, tissues are treated as hyperelastic materials. These parameters take into account both types of tissue nonlinearities: intrinsic nonlinearity and geometric nonlinearity. In addition to tissue classification, this elastography technique has other important clinical applications such as measuring normal tissue hyperelastic parameters *in vivo*. Such parameters are essential in computer aided interventional procedures and their planning. The proposed technique uses a constrained iterative inversion. The reconstruction technique can be viewed as an inverse problem, to solve which we use a nonlinear finite element (FE) model for solving the corresponding forward problem. In this research, we applied Veronda-Westmann, Yeoh and Polynomial models to model the tissue hyperelasticity. To validate the proposed technique, we conducted studies involving numerical and tissue mimicking phantoms. The numerical phantom comprises of a hemisphere connected to a cylinder while the tissue mimicking phantom we constructed from Polyvinyl Alcohol (PVA) with freeze-thaw cycles that exhibits non-linear mechanical behavior. Both phantoms consist of three types of soft tissues to mimic adipose and fibroglandular tissues and a tumor. Simulation and experiments results show the feasibility of the proposed method in reconstructing the hyperelastic parameters of the tumor tissue. With tissue mimicking phantom studies, we were able to reconstruct the ratio of the hyperelastic parameters

reasonably accurately. The ratio of the parameters is adequate for classifying tumor types since the difference in the mechanical behavior of the tissues are the basis for tumor detection and not their absolute values.

Keywords: Cancer Characterization, Breast Cancer, Modeling, Elastography, Hyperelastic, Constrained Parameter Reconstruction, Inverse Problem, Polyvinyl Alcohol, Regularization.

Dedication

To my Parents who gave me unconditional love and support

throughout my studies and my entire life

Acknowledgements

I would like to thank my supervisor, Dr. Abbas Samani for giving me the opportunity to join and collaborate with his research group for the past two years, and for inspiring and challenging me during my Master's studies and my research work. The accomplishment of this project would not have been possible without his extensive support and encouragement.

Special thanks go to the NRC London (National Research Council of London), especially Gordon Campbell for letting me construct the PVA phantom and helping me with the experiments throughout my thesis work.

I would also like to thank all of my colleagues at Dr. Samani's Lab who helped me with all aspects of my work and providing great time while I was doing my master studies over the past two years.

Table of Contents

List of Tables

List of Figures

List of Appendices

1. Introduction

Breast cancer is one of the most common forms of cancer in women. Worldwide, breast cancer is the second most common type of cancer after lung cancer (10.4% of all cancer incidence, both sexes counted) [1], and the fifth most common cause of cancer death [2]. In 2005, breast cancer caused 502,000 deaths worldwide (7% of cancer deaths; almost 1% of all deaths). According to Canadian Cancer Society [3], in 2008, an estimated 22,400 Canadian women will be diagnosed with breast cancer and 5,300 will die of it. Also, statistics shows that one in 9 women is expected to develop breast cancer during her lifetime; one in 28 will die of it. Various studies have shown that early breast cancer diagnosis is paramount for effective treatment and survival. Clinical studies have shown that breast screening - especially for women who are genetically prone to the disease - is effective. While breast screening using X-ray mammography has shown to be effective in women after menopause, its value is limited with younger women who have dense breast. Although younger women from the general population are less prone to breast cancer, there is a significant group with hereditary genetic disorder who are highly susceptible to the disease.

1.1. What is cancer?

A part of the body is called cancerous when its cells start to grow in an out of control manner. Healthy cells in the body grow, divide and finally die in an orderly fashion. During one's childhood healthy cells divide and grow rapidly and when he/she becomes an adult the rate of dividing and growing decreases. After childhood the cells in most parts of the body divide only if some cells are dead or if they are worn-out to repair

injuries, while the cancer calls continue to grow and divide. Therefore these cells are considered abnormal cells. The main reason for a cell to be cancerous is damage to its DNA. DNA directs all the activities of the cell and when it is damaged the cell behaves abnormally. In most cases if there is damage to DNA the body is able to repair it. In the case of cancer, the body is incapable of repairing the damaged cell. People may inherit damaged DNA, which accounts for inherited cancers. In most cases the person's DNA becomes damaged by exposure to something in the environment like smoking. The cancer usually manifests as a tumor in the body, but there are situations in which the cancer does not form a tumor, for example in Leukemia the cancer cells involve blood and blood-forming organs and circulate through other tissues. Cancer cells usually travel to other parts of the body where they begin to grow and replace normal tissues. This is called Metastasis. Tumors in the body are classified into benign and malignant tumors. Not all tumors are cancerous. Benign (non-cancerous) tumors do not spread to other parts of the body; therefore they are not life threatening in most cases. Each type of cancer behaves in a particular way and therefore different cancers require different treatments that are aimed at their specific kind of cancer. Cancer is the second leading cause of death in the United States. Nearly half of men and more than one third of women in United Stated develop cancer during their lifetimes. Today, millions of people are living with cancer. Life style is an important factor in reducing the risk of cancer. Lifestyle changes such as quitting smoking or using a better diet can reduce the risk of cancer. The sooner a cancer is detected, the better the chances for recovering from the disease and living for more years. The purpose of this thesis is to introduce a novel method to diagnose breast

cancer in its early stages so that the treatment can start before it is too late and before the cancer has spread throughout the body.

1.2. What is Breast Cancer?

Breast cancer is a tumor that starts from breast cells. Breast tumors can be malignant or benign. As indicated before, benign tumors are not life threatening in most cases. Therefore, only malignant breast tumors are addressed as breast cancer. A malignant tumor is a group of cancer cells that invade surrounding tissues or spread to distant areas of the body. This cancer is specific for women but it rarely occurs in men too. To understand breast cancer, first we need to learn about the structure of normal breast tissue.

Female breast is made up of three different parts as shown in Figure 1-1. Lobules are the milk producing glands in the breast. The tiny tubes in the breast that carry the milk from the lobules to the nipple are called the Ducts. Stroma is the fatty tissue and connective tissue surrounding the ducts and lobules, blood vessels, and lymphatic vessels. Breast cancers that occur in ducts are called ductal cancers and cancers that occur in the lobules are called the lobular cancers. Most breast cancers are ductal cancers, some are lobular and there are some other cancers that occur in other tissues in the breast.

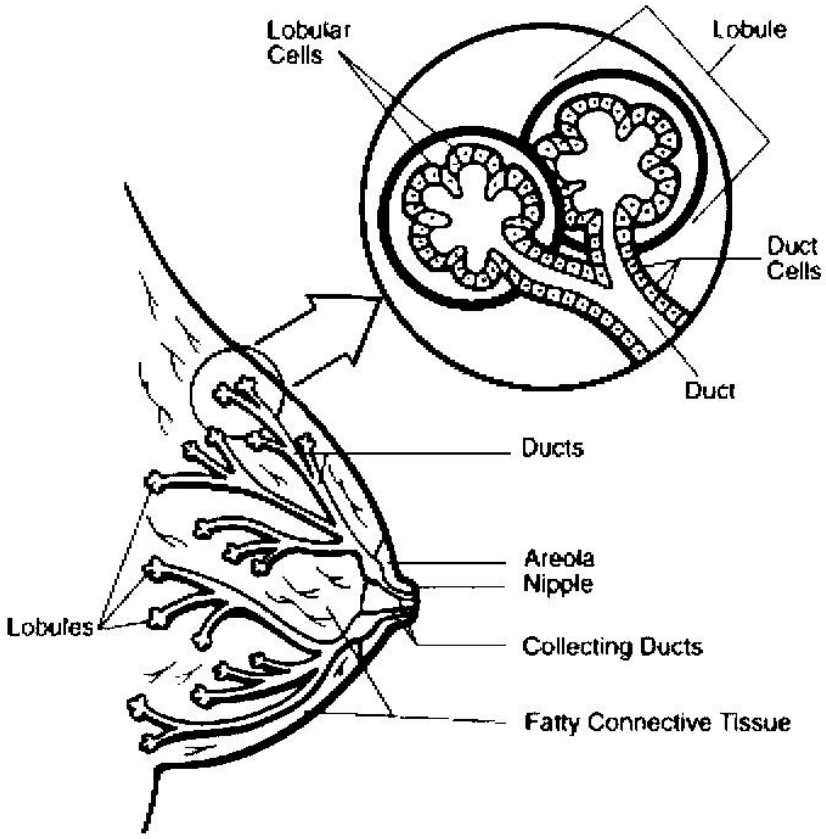

Figure 1-1: Structure of normal breast tissue

1.3. Benign Breast Lumps

Not all lumps in the breast are cancerous. Noncancerous lumps are called benign tumors. Benign tumors are abnormal growths in the breast such as fibroadenomas or intraductal papillomas tumors. These abnormalities cannot spread outside of the breast to other organs, thus they are not considered as cancer. For instance fibrocystic changes in the breast are assumed as benign lumps. The term fibrocystic refers to fibrosis and cysts. Cysts are fluid filled sacs and fibrosis is the formation of fibrous tissue. These changes may cause swelling and pain in the breast.

1.4. Clinical Exams for Breast Cancer Diagnosis

There are several tests to diagnose breast cancer in women. In these tests the physician looks for any abnormality in the breast such as changes in shape or color, etc.

Breast self exam (BSE) is a test that women older than 20 are recommended to use as a first test to diagnose any abnormality in their breasts. Since they know how their breasts normally look and feel they can detect changes in their breast and report it to a health care professional. If any abnormality is detected in the breast it is required to perform more advanced tests and clinical exams.

1.5. Mammography

A mammogram is an X-ray exam of the breast. There are two different categories of mammograms, screening mammograms and diagnostic mammograms. Both mammograms are the same and differ only in the people they are applied to. If mammography is used for women with no symptoms or pain and is being used to look for cancers, it is called screening mammogram. If it is being used with a woman who has symptoms and problems in the breast such as lumps, pain or nipple discharge, it is called diagnostic mammogram. Mammography has been used for breast cancer detection for more than 90 years since the first X-ray machines became available.

Breast mammography uses low energy X-ray beams so that it does not penetrate the tissue as easily as it does for chest X-ray or arm X-ray while improving the image contrast.

For mammography, the breast tissue is squeezed between 2 plastic plates attached to the mammogram machine as shown in Figure 1-2. This compression last just for a few seconds and must be such that the breast tissue spreads apart. This high compression is

required to have little movement, sharp image and lower X-ray dose. Mammography is a black and white image of the breast.

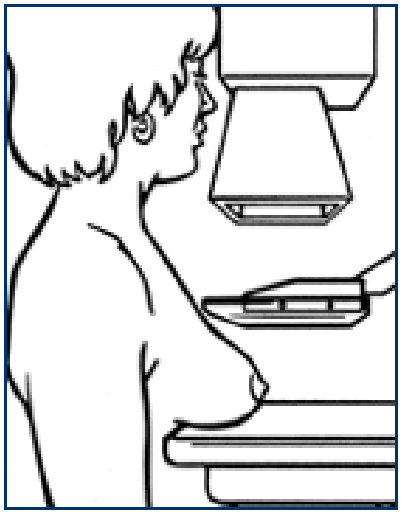

Figure 1-2: Schematic of breast mammography process

1.6. Magnetic Resonance Imaging (MRI)

Magnetic Resonance Imaging is a noninvasive imaging technique that exploits differences in magnetic properties of atomic nuclei. This technique uses magnets and RF (radio frequency) waves to construct cross-sectional images of the breast. MRI machines use a strong magnet to align spins of the nucleons in nuclei of hydrogen atoms in the tissue. While the spins are all aligned, an RF pulse is used to excite them. This pulse is an external magnetic field at Larmor frequency. This RF pulse causes the spins to tilt away from their alignment direction. MRI provides various image contrasts (T1–weighted and T2–weighted) of the tissue according to the relaxation of spins to their aligned direction. Each image exploits a specific magnetic property of the tissue.

Breast MRI is not a common breast screening method; it is usually used for women with high risk of breast cancer. To get a better image of the tissue, some contrast material

(Gadolinium DTPA) is usually injected to the patient. This method is used in cases where a cancer is diagnosed and further investigation is required on the cancerous area, or if a suspicious area is detected in the mammogram.

Although breast MRI provides a detailed 2D or 3D image of the breast and is very sensitive to cancer, it may miss some cancers that mammograms can detect. In other words the false-positive rate (where the test finds something that turns out not to be cancer) of breast MRI is high. This results in unneeded breast biopsies. Thus, breast MRI is used as a compliment to mammogram and not as a replacement, especially for women with average risk of cancer. MRI provides very detailed images of the breast tissue; a typical breast tissue image using magnetic resonance imaging technique in two different positions are shown in Figure 1-3.

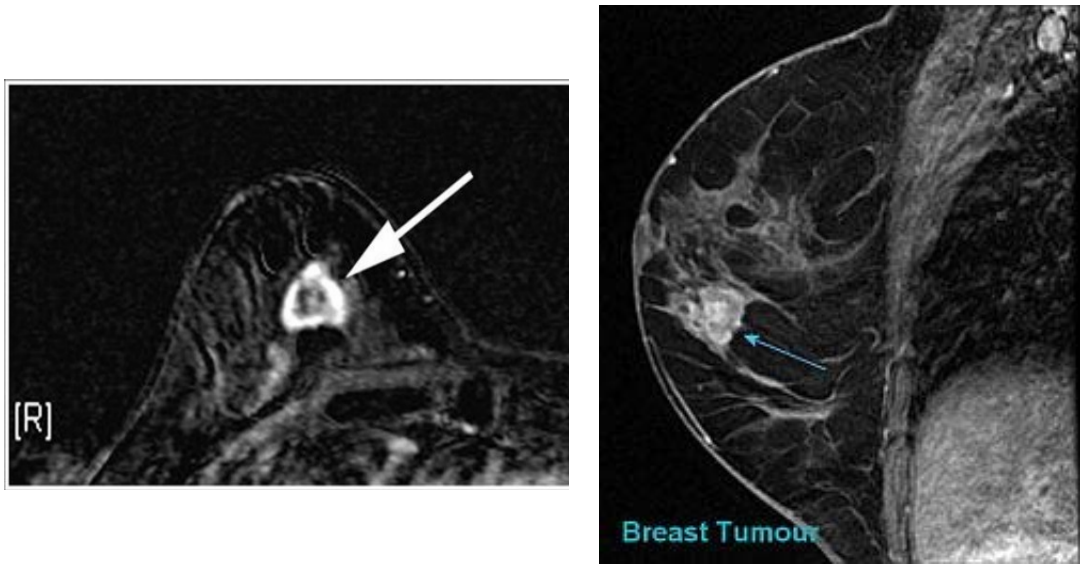

(a) **(b)**

Figure 1-3: A typical breast tissue image using Magnetic Resonance Imaging (MRI) technique in two different positions.

1.7. Breast Ultrasound

Ultrasound, also known as sonography is an imaging technique that is used for breast cancer screening. Ultrasound system sends high frequency sound waves through the body using an ultrasound probe. This sound wave attenuates as it passes through different tissues and its echoes return to the probe. The attenuation rate of the ultrasound wave differs as it passes through different tissues. The probe collects all the echoes from the body and calculates the attenuation coefficient of each tissue type in addition to the distance of the point in the body that the echo comes from. Since each tissue type has a specific attenuation coefficient, the tissue type and its distance from the probe can be calculated. The Ultrasound machine forms an image of the tissue according to the attenuation coefficients of every point.

As the Ultrasound transducer emits a high frequency wave (2 - 15 MHz), the wave travels through the tissue with a specific velocity. This wave reflects when it encounters a boundary in the tissue. The reflection returns back to the transducer at a time delay t (the total elapsed time since the wave was first emitted). If the velocity of ultrasound wave in the tissue is v, the distance from the probe to the point from which the wave was reflected d can be calculated using Equation (1-1),

$$d = 0.5 \times v \times t, \qquad (1-1)$$

The sound velocity in a tissue depends on the physical characteristics of the tissue, for simplicity in ultrasound imaging machines this velocity is assumed to be constant. This speed for soft tissues is 1540 m/s.

Breast Ultrasound is usually used for breast screening along with regular mammograms. Like MRI, this diagnostic technique does not replace mammogram and is an additional

tool for better detection of any abnormality in the breast. Ultrasound is the only way to distinguish a tumor from a cyst without placing a needle in it. Cysts cannot be accurately diagnosed using physical exams. Ultrasound images are very difficult to interpret. They consist of a large number of speckles and are dependent on the position of the probe. Figure 1-4 shows an ultrasound image of a breast.

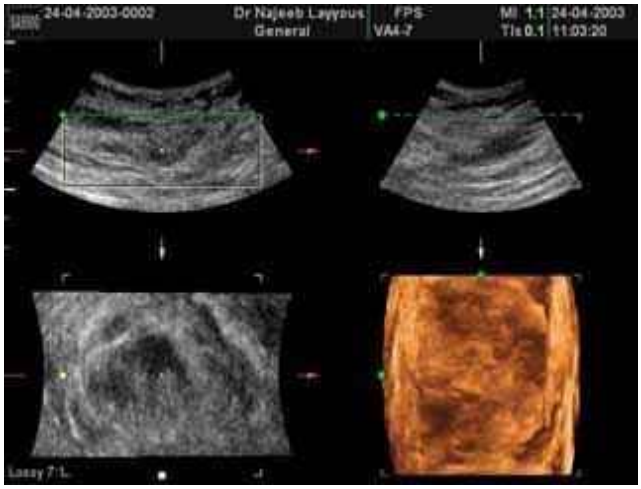

Figure 1-4: A typical ultrasound image of a breast tissue

1.8. Elastography

It is known that pathologies in soft tissues are associated with changes in their elastic properties. Tumor tissues are usually stiffer than the normal tissues. This property of abnormal tissues is the basis for manual palpation that is usually used as a self examination for breast cancer diagnosis. Elastography has a higher degree of sensitivity (the ability of the method to detect an abnormality and separate it from healthy tissues) and specificity (the ability of the method in detecting the type of abnormality once it is detected, for example if the tumor is malignant or benign, etc.) [4]. Low sensitivity and specificity are the main weaknesses of many other imaging techniques. This new imaging

modality was first introduced by J. Ophir *et al* [5] and is discussed in detail in the following chapter. From tissue mechanical behavior perspective, there are two different approaches to Elastography, the first one usually known as classic Elastography assumes that the tissue's elastic behavior is linear (Hooke's law). The other approach assumes that the tissue exhibits nonlinear behavior when a compression is applied to the tissue. This approach will be referred to as Hyperelastic Elastography. In this thesis, the nonlinear or Hyperelastic Elastography approach is used to formulate a technique for breast cancer diagnosis.

1.9. Research Objectives

Elastography can be used to improve both sensitivity and specificity of the current cancer detection techniques. There has been a lot of research in both detecting presence of abnormality (sensitivity) and also detecting type of the abnormality (specificity) using elastography. Considering the fact that the sensitivity of other detection methods is relatively high, the main advantage of using elastography is its higher specificity.

Linear elastography has shown promising results in detecting presence of abnormality. There have been a lot of research efforts in specifying the type of abnormalities according to literature Ophir *et al* [5]. The main problem with the current linear elastography is different groups have reported a wide range of values for the Young's modulus of each type of pathological tissues. Presence of these discrepancies in the measurements of different research groups makes the results of linear elastography unreliable. Linear elastography is very sensitive to the experiment conditions. Slight changes in the setup or the way analysis is performed results in significant change in the constructed stiffness values.

In this thesis our main interest is not detecting abnormalities as this can be done by conventional imaging or linear elastography reasonably accurately. The purpose of our research is to characterize the type of abnormality and increase the specificity of elastography. Having higher specificity is very important to avoid sending breast cancer patients for unnecessary biopsies.

One issue with linear elastography is the amount of pre-compression that is being applied to the tissue. Since the tissue linearity assumption is valid for a small range of strain, it is necessary to be in that range to get correct results. This is the main reason for discrepancies in different reported values. Furthermore, to maintain its validity, linear elastography is limited by small deformation for mechanical stimulation. Such small deformations imply small displacement signal-to-noise-ratio (SNR). This small SNR leads to significant errors in the reconstructed values of the elastic modulus.

The first objective of our research is to overcome these deficiencies of elastography by adding non-linearity of the tissue behavior to our system. Soft tissues tend to exhibit nonlinear mechanical behavior and in this investigation we attempt to characterize this behavior.

Nonlinear (hyperelastic) mechanical behavior is valid for wide range of strain. Thus the effect of pre-loading is minimized as, contrary to constructed elastic modulus, the constructed hyperelastic parameters are valid for a wide range of tissue deformation. Any portion of the stress-strain curve can be used for analysis. In addition, applying large deformations is allowed in this case, which implies having large SNR values, thus the effect of noise in the reconstruction is minimized.

The second objective of our research is *in vivo* measurement of hyperelastic properties of soft tissues. This is being done for the first time and has significant applications in image guided surgery and developing virtual reality environments. Knowing the hyperelastic parameters of tissues is required to predict tissue deformation required to direct the surgeon accurately during operation.

Tissue hyperelastic properties measured *in vivo* can also be used in developing virtual reality environments. These environments have several applications such as training surgeon without risking the life of patients. Therefore, it is very important to develop a technique to measure tissue behavior *in vivo*.

We have developed a technique for reconstructing the hyperelastic parameters of soft tissues *in vivo*. This is a novel technique that has been introduced for the first time by our group and the results of applying it to soft tissues have shown its good performance. This problem is formulated in an inverse problem framework in our method, and the parameters are reconstructed in by iteratively updating the parameters values. To overcome the difficulties of solving this inverse problem we introduced a novel constrained hyperelastic parameter reconstruction technique. While constraining our inverse problem helped reduced the ill-conditioning of the problem, it remained highly sensitive to noise with some hyperelastic models. To address this issue, we developed a novel sequential regularization technique.

2. Literature review

2.1. Elastography

Elastography is a non-invasive method in which stiffness or strain images of soft tissues are used to detect or classify tumors [6]. It is known that changes in the stiffness of soft tissues are associated with the presence of pathology. In the case of breast cancer, a tumor or a suspicious cancerous growth is normally stiffer than the background normal soft tissue. This stiffness ranges from 3-6 times the stiffness of fibroglandular tissue for benign tumors to 13 times in the case of high grade invasive ductal carcinoma [7, 8]. This forms the basis for the commonly used breast manual palpation technique initially used for breast cancer detection. Physicians have relied on palpation of hard tissue areas for the purpose of tumor detection. Present cross-sectional imaging methods display tissue parameters not directly associated with the findings on palpation [9].

Manual palpation; however, is not sufficiently sensitive with cases where the tumor is not large enough or is located deep within the breast. In addition, the specificity of palpation is low and the method is incapable of determining the type of abnormality, thus biopsy is required. In such cases, the tumor cannot be detected by palpation in early stages [10]. Therefore more qualitative methods are required to detect the presence of abnormalities.

2.2. Basic principles in elastography

The stress-strain relationship for most soft tissues is nonlinear. Also, a hysteresis loop is encountered in cyclic loading and unloading of the tissue and stress tends to relax over time under constant strain. The hysteresis loop is shown in Figure 2-1.

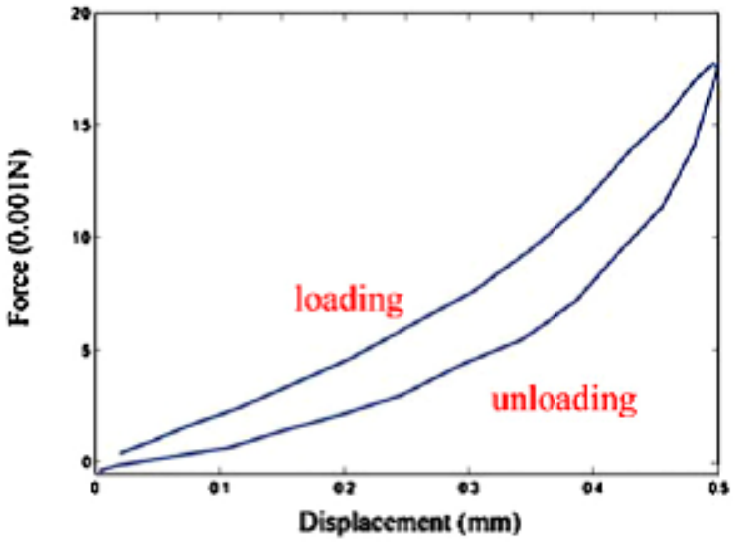

Figure 2-1: Hysteresis loop in biological tissues

Many models have been proposed to characterize the stress-strain relationship in tissues based on the linear theory of viscoelasticity, described by Voigt, Maxwell and Kelvin. Viidik (1996) [11] introduced a nonlinear formulation of tissue mechanical behavior. Fung (1981) [12] formulated a quasi-linear viscoelasticity theory of soft tissues. He stated that the theory of linear viscoelasticity applies for oscillations of small amplitude, while for finite deformation his theory accounts for a nonlinear stress-strain relationship.

The concept of elastography is developed as a technique to map tissue elasticity in a way that adds new, clinically useful information to the interpretation of ultrasound, CT or other scans. In elastography tissue displacement tracking is required. This is usually done by using the images of the tissue taken by other imaging modalities. Cross correlation information of A-line pairs of ultrasound images are used by Ophir's group to provide this information [13]. Other groups such as Miga *et al* [14] have used MR images for

displacement tracking. MR phase imaging is one of the methods that give information about the displacements of the tissue [15].

Various elastography techniques have been developed to extract different properties. Some terms and definitions in elastography as defined in [9] are:

- Elastography: the general field of elasticity imaging
- Sonoelastography: the use of ultrasound for imaging of tissue elastic parameters

Either of the above terms could be modified by the terms describing the method of tissue deformation and the parameters that are imaged:

- Strain images: images displaying tissue strain
- Stress images: images displaying tissue stress
- Compression images : images based on static or nearly static tissue compression
- Quasi-static elastography images: images based on very low frequency (less than 10 Hz) vibration

2.3. Theory of elasticity

Figure 2-2 shows the undeformed configuration of a material continuum at time $t = t_0$ together with the deformed configuration at a later time $t = t$. Suppose that a material point at position X in the undeformed tissue moves to a position x when the tissue is loaded. We may describe the deformation and motion of a tissue by a mapping in the following form:

$$x = \chi(X, t) \qquad 2-1$$

Assuming the coordinates of the two systems are coincident, the material point displacement is:

$$u(t) = x(t) - X \qquad 2-2$$

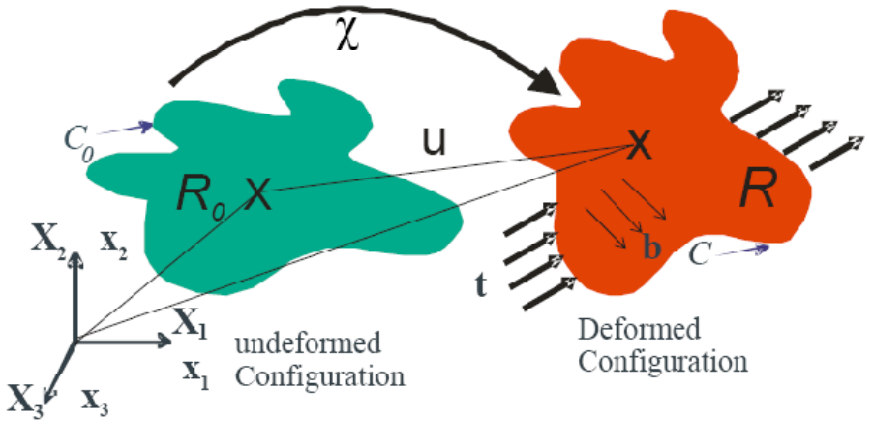

Figure 2-2. Displacements of a point while the object undergoes large deformation

Assuming that dS is the distance between two points in the undeformed configuration and ds is their distance in the deformed configuration, we have the following relationship between ds and dS :

$$dS + u + du = u + ds, \quad \Longrightarrow \quad du = ds - dS \qquad 2-3$$

where u and du are shown in fig 2-3

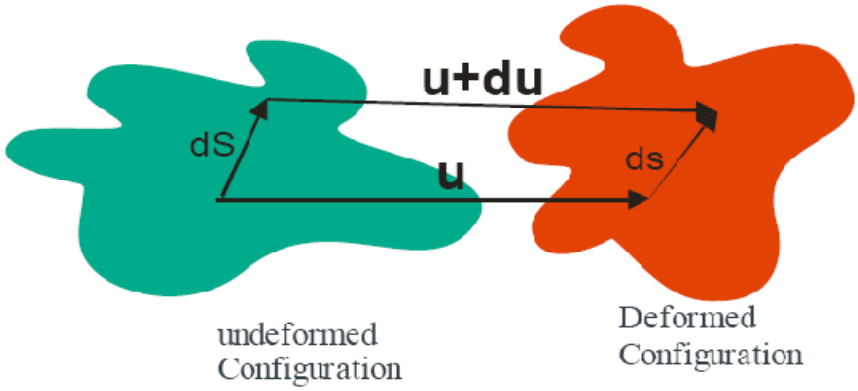

Figure 2-3. Measuring deformations of a point with respect to another point while going from undeformed configuration to deformed configuration

The distance $(ds)^2 - (dS)^2$ is used to define a measure of deformation and occurs in the vicinity of particles in the deformed and undeformed configurations.

We also have

$$(ds)^2 - (dS)^2 = d\bar{x}_\iota d\bar{x}_\iota - d\bar{X}_\iota d\bar{X}_\iota \qquad 2-4$$

and

$$\bar{x}_\iota = \bar{x}_\iota(X_1, X_2, X_3)$$

$$d\bar{x}_\iota = \frac{\partial \bar{x}_\iota}{\partial X_1} d\overline{X_1} + \frac{\partial \bar{x}_\iota}{\partial X_2} d\overline{X_2} + \frac{\partial \bar{x}_\iota}{\partial X_3} d\overline{X_3} \qquad 2-5$$

$$d\bar{x}_\iota = x_{i,j} d\bar{X}_J = F \cdot dX$$

In the above equation F is defined as the deformation gradient. We also define:

$$u = u_1 e_{x_1} + u_2 e_{x_2} + u_3 e_{x_3} = u_i e_{x_i} \qquad 2-6$$

where $e_{x_i}{}'s$ are unit vectors. The measure of deformation can be calculated using the following equation:

$$(ds)^2 - (dS)^2 = \left(u_{i,j} + u_{j,i} + u_{k,i} u_{k,j}\right) d\bar{X}_\iota d\bar{X}_J$$

$$= 2\varepsilon_{ij}^L d\bar{X}_\iota d\bar{X}_J \qquad 2-7$$

where we define strain tensor as follows:

$$\varepsilon_{ij}^L = \frac{1}{2}\left(u_{i,j} + u_{j,i} + u_{k,i} u_{k,j}\right) \qquad 2-8$$

We make some assumptions to simplify the equations for linear elasticity. We assume that the deformation is infinitesimal. Thus we can assume that $u_{k,i} u_{k,j} \approx 0$ and we can rewrite the strain tensor as:

$$\varepsilon_{ij}^L = \varepsilon_{ij}^E = \varepsilon_{ij} = \frac{1}{2}\left(u_{i,j} + u_{j,i}\right) \qquad 2-9$$

The internal traction vector $\boldsymbol{T}_n$ represents the force per unit area acting on a plane with normal vector $\boldsymbol{n}$ inside the deformed solid and can be defined as:

$$T_n = \lim_{dA \to 0} \frac{dP_n}{dA} \qquad 2-10$$

in which dA is an element of area in the interior of the solid, with normal $\boldsymbol{n}$. The components of Cauchy stress in a given basis can be visualized as the tractions acting on planes with normals parallel to each basis vector, as depicted in Figure 2-4.

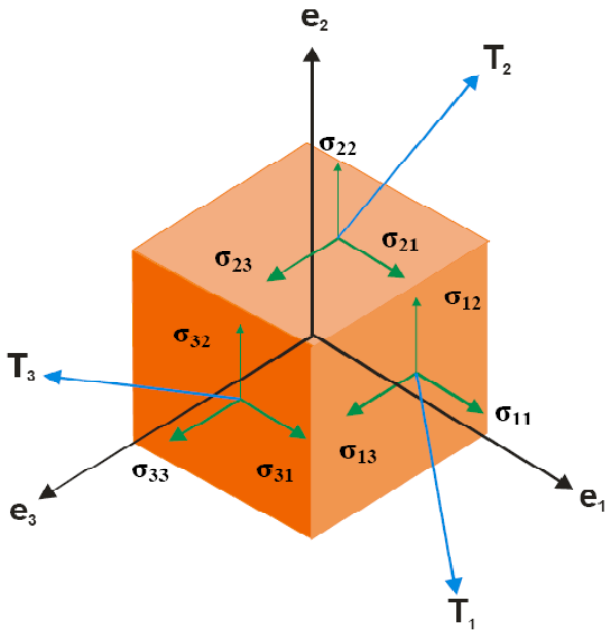

Figure 2-4. The components of Cauchy stress in a given basis visualized as the tractions acting on planes with normal vectors parallel to each basis

Here we can write:

$$T_1 = \sigma_{11}e_1 + \sigma_{12}e_2 + \sigma_{13}e_3$$

$$T_2 = \sigma_{21}e_1 + \sigma_{22}e_2 + \sigma_{23}e_3 \qquad or \qquad T_i = \sigma_{ij}e_j \qquad 2-11$$

$$T_3 = \sigma_{31}e_1 + \sigma_{32}e_2 + \sigma_{33}e_3$$

where $\sigma_{ii}{}'s$ are the components of the Cauchy stress tensor.

The governing equation of the stress tensor distribution for an arbitrary volume is:

$$\sigma_{ji,j} + f_i = \rho\ddot{u}_i \qquad 2-12$$

where ρ is the mass density of the tissue, f_i denotes the body forces and u_i are the displacement vector components.

The static form of the above equations, usually known as the equilibrium equations, is:

$$\sigma_{ji,j} + f_i = 0 \qquad 2-13$$

For an elastic body, which is gradually strained at constant temperature, the components of stress can be derived from the strain energy density ψ, which is a quadratic function of the strain components.

$$\sigma_{ij} = \frac{\partial \psi}{\partial e_{ij}} \qquad 2-14$$

Accordingly, we may write the most general form of Hooke's law as:

$$\sigma_{ij} = E_{ijkl} e_{kl} \qquad 2-15$$

in which E_{ijkl} represents 81 components. For isotropic materials, the stress-strain relationship should not depend on the system of coordinates and its orientation. . In such a case the system of equations will depend on only two parameters (λ and μ). λ and μ are called the Lamé constants. Therefore, for linear elastic isotropic materials, Hook's Law can be written as:

$$\sigma_{ij} = 2\mu\varepsilon_{ij} + \lambda\delta_{ij}\varepsilon_{kk} \qquad 2-16$$

The Lamé constants are quite suitable from mathematical point of view, but they should be related to the Engineering elastic constants (E and ν) obtained in the laboratory. Using these constants, it can be shown that:

$$\varepsilon_{ij} = \frac{1}{E}\left[(1+\nu)\sigma_{ij} - \nu\delta_{ij}\sigma_{kk}\right] \qquad 2-17$$

$$E = \frac{\mu(3\lambda + 2\mu)}{(\lambda + \mu)} \qquad 2-18$$

2.4. Linear Elastography

Imaging elastic properties of the tissue (Elastography) is a method to assess the differences in tissue stiffness in a quantitative way. The goal of elasticity imaging is to map the elastic properties of the tissue (Young's modulus, Poison's ratio) in an anatomically meaningful way to provide clinical information about any abnormality existing in it [10]. The mechanical properties of soft tissues are mainly influenced by the fact that they are biphasic; i.e. they have a solid phase and a fluid phase, with the fluid comprising over 90% of the tissue. This leads to the near incompressibility of soft tissues, which is characterized by Poison's ratio values ranging from 0.490 to 0.499 [16, 17]. In classic elastography the tissue is assumed to exhibit linear behavior. Having the Poison's ratio and using Hooke's law, the only parameter required to characterize the tissue elastic behavior is its Young's modulus. In quasi-static elastography, the tissue is stimulated by applying very low frequency (less than $10Hz$) external compression.

Ophir *et al* [13] proposed a method to calculate the strain field of a linear elastic and isotropic material. They applied static external compression to the specimen. Using cross correlation information of the pre-compression and post-compression A-line pairs, they calculated the strain field inside the tissue. Having the strain field in the tissue and stress field near the transducer they calculated the Young's modulus of the specimen. In this method they only acquired and used the axial component of the displacement field. Konofagou *et al* applied a weighted interpolation method to the neighboring RF A-lines to calculate the lateral displacements of the tissue [18].

2.5. Unconstrained Modulus Reconstruction

Tissue deformation estimation is required to determine and map elastic properties of soft tissues. MRI and Ultrasound are usually used for this purpose. In case of ultrasound, a small quasi-static compression (about 1%) is applied to the tissue. Radio frequency (RF) A-lines are recorded before and after compression and local axial motion is estimated. Assuming that the tissue is linear elastic and isotropic that is subjected to constant stress field, it can be shown that the tissue's elastic modulus distribution relative to a tissue baseline is equal to the inverse strain field relative to the same baseline tissue [19]. In practice the stress field is not constant due to the finite size of the compressor. The stress is high near the compressor interface and reduces at farther points. This decay in stress field is called hardening artifact [5]. This artifact arises from misinterpretation of the strain images as a relative measure of tissue elasticity distribution. To reduce this artifact analytical models that predict the stress field produced by finite size compressor in semi-homogeneous medium can be used. While this method is suitable for a homogeneous medium it is not valid for an inhomogeneous medium, especially near the inclusion where stress concentration occurs. To overcome these limitations the elastography reconstruction problem must be formulated as an inverse problem.

Skorovoda [20] proposed a method for tissue elasticity reconstruction assuming that the tissue is incompressible, isotropic, inhomogeneous and subject to static external compression. Incompressibility assumption is used to eliminate the pressure term from elasticity equations. This method leads to a system of equations, which are functions of spatial derivatives of Young's modulus, the displacement field and the strain tensor [21]. To reconstruct the Young's modulus distribution in this method, the displacement field

components throughout the tissue volume and the Young's modulus values on the boundaries must be known. This method is called unconstrained modulus reconstruction technique. With US imaging, the problem is that only those components of the strain field placed in the acoustical plane can be measured. Thus, it would be necessary to assume plane strain state to reconstruct tissue elasticity [21].

Another method introduced by Sumi *et al* [22] proposed an inverse problem, which assumes a plain stress state. This method leads to a linear system of equations for tissue elasticity reconstruction. In practice all tissue motion components except for its axial components are estimated with large variance. Therefore the signal-to-noise-ratio is acceptable only for the axial component of the motion. To improve the estimation of the displacement lateral component from its axial component, the incompressibility assumption can be used.

Kallel *et al* [19] proposed using a regularized perturbation method to solve the inverse problem in elastography. In this method only the axial component of the displacement field is used for elasticity distribution reconstruction.

2.6. Constrained Modulus Reconstruction

In the case of unconstrained modulus reconstruction some difficulties arise in 3-dimensional (3-D) analysis. The most difficult challenge in 3-D elasticity reconstruction approaches is that they lead to highly ill-conditioned inverse problems. In fact, it is this challenge that led researchers to use 2-D idealization of the displacement field to be able to reduce the problem's ill-conditioning. Other methods use nonlinear least squares algorithms to solve the system of equations [5, 23]. These methods require inversion of a Hessian matrix at each iteration, which is costly, time consuming and prone to error.

To overcome this problem Samani *et al* [24, 25] proposed a method called quasi-static constrained elastography technique. A number of reasonable assumptions are made in this method to simplify the analysis and lead to efficient and reasonably accurate reconstruction in elastography. This method assumes uniform elasticity modulus distribution throughout each tissue volume. Unlike strain imaging methods of elastography, this technique takes into account the non-uniform stress distribution throughout the tissue volumes to reconstruct the elasticity modulus from measured displacements. The novelty of this method is the use of anatomical constrains to impose a discrete elasticity modulus distribution throughout each tissue type in the reconstruction [26]. This method segments the 3-D image of the tissue into a small number of tissue types with uniform elasticity properties [27]. Contrary to unconstrained methods, this method leads to a well-conditioned inverse problem and performs well in 3-D problems. Furthermore, the reconstruction is much faster compared to reconstruction methods formulated based on non-linear least squares inversion.

2.7. Tissue non-linearity

The stress-strain relationship in soft tissues can be assumed to be linear only for a small range of strains. If a large range is being used for the analysis, the stress-strain relationship is non-linear as shown in Figure 2-1. There are two different sources for this non-linear behavior. Intrinsic non-linearity of the tissue which arises from the tissue structure, and geometric non-linearity which arises if large deformations are used for the analysis [28].

2.8. Intrinsic non-linearity of soft tissues

The mechanical behavior of a particular tissue can be attributed to characteristics of the various proteins, such as elastin and collagen, living cells, ground substances such as proteoglycans, and the orientations of fibers within the tissue. The load-bearing components of a tissue are its elastin and collagen fibers. Thus the mechanical behavior of the tissue is determined by the amount and orientation of its elastin and collagen fibers. Elastin exhibits approximately linear behavior over much of its physiological range while collagen is much stiffer with a Young's modulus much higher than elastin. For the case of lung tissue, the Young's modulus of collagen is 10^3 to 10^4 times stiffer than that of elastin. The structure of these fibers together gives rise to the non-linear mechanical behavior of the soft tissue [29]. This non-linearity is called intrinsic non-linearity since it is due to the physiological components of the tissue.

2.9. Geometric non-linearity of soft tissues

Geometric non-linearity of the tissue is defined as the stiffening of the tissue due to the thinness of the tissue [30]. If a loading is applied to the beam as shown in Figure 2-4, the bending moment at the clamped end will be dependent on both the beam's length and its deflection at the free end where the loads are applied. If the deflection is small, its influence of the bending moment is negligible and vice versa. This redistribution of internal forces as a result of large deformation of material leads to the so called geometric nonlinearity. In general large tissue deformation, which is common with most soft tissues is associated with geometric non-linearity.

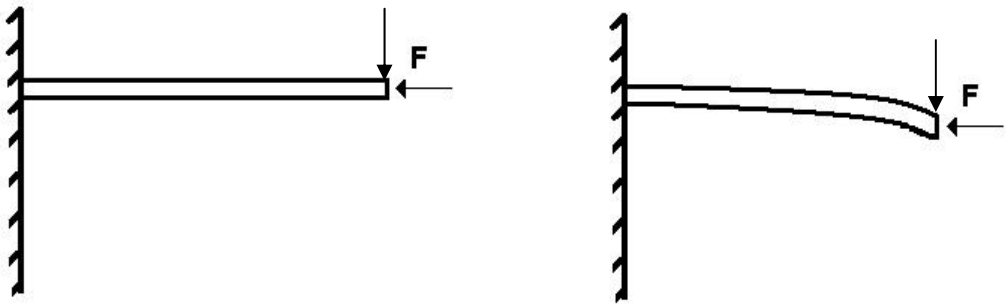

Figure 2-5 Loading a beam while considering geometric non-linearity

The non-linear behavior of soft tissues does not occur only because of the intrinsic nonlinearity of the tissue, but it is due to the change in its geometry under the imposed loading and boundary conditions. This non-linearity appears in the stress-strain relationship of the tissue while it does not change its elastic behavior; i.e. the stresses and deformations disappear when the loading is removed [31].

2.10. Hyperelastic Elastography

Several factors are considered to assess the quality of the strain estimate in elastography. Factors such as Elastography signal-to-noise-ratio (SNRe) or elastography contrast-to-noise-ratio (CNRe) and spatial resolution. Srinivasan *et al* [32] showed that there exists tradeoff between these quality factors in linear elastography. They stated that large improvement in the SNR is possible at the expense of a small reduction in the resolution. Tissues are expected to exhibit linear behavior in the case of small deformations. Bishop *et al* [27] showed diffusion-mediated signal attenuation which limits maximum strain SNR in small displacement cases. With large compressions, the contrast in the elastography changes significantly due to the nonlinear stress-strain relationship in the

tissue. The stiffness of the soft tissue is strain dependent and the Young's modulus of the tissue increases with compression. Varghese *et al* [33] illustrated that the contrast of the elastogram and the contrast to noise ratio in elastography changes significantly due to the changes in tissue modulus as the strain increases.

Most data available in the literature apply small strain (less that 10%) to the soft tissue to use the linearity assumption for the tissue. To represent the mechanical properties of soft tissues accurately, it is required to take into account their nonlinear behavior [34]. Hu *et al* [35] used FEM (Finite Element Method) based analysis of soft tissue indentation to find its hyperelastic parameters.

Although assuming that the tissue exhibits linear behavior (as used in classic elastography) is valid when small external compression is applied, most soft tissues, especially breast tissues deform significantly as a result of small but inevitable body motion; e.g. motion resulting from respiration that causes chest motion [36]. This kind of external and uncontrolled motion yields significant compressions of the tissue compared to the amount of compression allowed for the linearity assumption to be valid. Thus linear elastic behavior of the tissue is maintained at the cost of having small signal to noise ratio of tissue deformation. To avoid this problem, large external compression can be applied to the tissue. This results in large tissue deformation and consequently large signal to noise ratio.

In breast quasi-static elastography, tissue deformation can be very large due to the lack of physical constraints and low stiffness of the breast tissue. In large deformations the tissue's stiffness cannot be assumed to be constant for all strains because of the tissue's intrinsic nonlinear behavior. Most soft tissues exhibit strain hardening in the case of large

deformation [37, 38]. Taking into account these problems, linear elasticity is not sufficient to model the breast tissue deformation and, therefore, nonlinear elasticity must be considered using hyperelastic models. Ignoring hyperelastic effects generally leads to sub-optimal contrast (stiffer tissues at lower strains are contrasted against softer tissues at higher strains) in the elastogram [39].

Signal to noise ratio (SNR) of deformation of the system increases in large deformations [40, 41]. If the tissue nonlinear behavior at large deformations is not taken into account in the reconstruction system, the contrast to noise ratio (CNR) and the image contrast in elastography decreases leading to increased errors. To overcome this limitation, nonlinear modeling must be used [39]. Sinkus *et al* [42] used MR elastography to show that various breast pathologies exhibit different nonlinear behavior. Therefore, nonlinear (hyperelastic) elastography has a potential to be a highly specific breast cancer diagnosis technique.

Finding scalar parameters that describe the nonlinear behavior of the tissue is the ultimate goal of elasticity imaging (elastography). These parameters are intrinsic properties of the tissue and are independent of the boundary conditions [39].

In order to formulate the tissue's nonlinear behavior, a strain energy function, which characterizes the tissue strain energy after loading, is required. A hyperelastic material model relies upon the definition of the strain-energy function, which assumes different forms according to the material or class of material considered. This function is obtained from symmetry, thermodynamics and energy considerations [43]. There are different types of strain energy functions defined for modeling the hyperelastic behavior of tissues such as Neo-Hookean, Ogden, Mooney-Rivlin, Yeoh, Veronda-Westmann, Polynomial

and Reduced Polynomial. Among these strain energy functions Neo-Hokean and Mooney-Rivlin models have one and two parameters, respectively. Thus they have lower level of complexity but their approximation to the stress-strain curve is less accurate than other models. The polynomial form with $N = 2$ (N is the order of the polynomial) is the most commonly used form in the literature. The Veronda-Westman, model introduced in 1970, has an exponential form and provides a very close fit to the typical soft tissue stress-strain curves. This model was first introduced to model skin tissue; it has also been used to model lung tissue. Its application to breast tissues has been done recently, leading to good results [44]. The only difficulty of using this model is that it is non-linear in terms of its three parameters and leads to non-linear optimization that is costly and time consuming. These functions and there forms are described in detail in the next chapter.

3. Theory and Methods

3.1. Large deformation:

Strains greater that 3-5% are considered large deformations and appropriate formulation must be used for modeling. In this case the assumption of having linear relationship between stress and strain is no longer valid since the tissue's stiffness increases as the strain increases. This phenomenon is known as strain hardening of soft tissues as they undergo compression.

For breast tissue modeling it is not applicable to use linear elasticity since the breast tissue deforms extensively due to lack of physical constrains and low stiffness of the tissue itself. These properties of the breast tissues result in significant deformation resulting from respiration or other inevitable body motions. The latter deformation can be viewed as noise, to minimize the effect of which large amount of compression is required to stimulate the tissue.

We define a reference or undeformed configuration as the condition that no load is applied to the tissue. We also define a deformed configuration as the situation in which the load is applied. Assuming x' to be the position vector in 3-D space in the reference configuration and x as the position vector in 3-D space in the deformed configuration we obtain

$$x_i = x_i' + u_i \qquad 3-1$$

where u is the displacement vector. Considering an infinitesimal piece of material in the tissue, we obtain the orientation vectors defined as,

$$dx_i = \partial x_i / \partial x_j' \times dx_j' \qquad 3-2$$

dx' is the gradient vector in the reference configuration and dx is that of the deformed configuration. Deformation gradient is defined as the mapping between the two material vectors

$$F_{ij} = {dx_i}/{dx_j} \qquad 3-3$$

The deformation gradient (F) is a second order asymmetric tensor and for the 3-D space is a 3×3 matrix. Substituting equation 3-1 in equation 3-3 we obtain the following equation

$$F_{ij} = \delta_{ij} + \frac{du_i}{dx_j'} \qquad 3-4$$

where δ_{ij} is the Kronecker delta, which represents the second order identity tensor dx_i'/dx_j'.

Three invariants of F are calculated as follows.

$$I_1(First\ Strain\ Invariant) = trace\ (F) = F_{11} + F_{22} + F_{33} = F_{ij}\delta_{ij}$$

$$I_2(Second\ Strain\ Invariant) = \frac{1}{2}\left(F_{ij}F_{ij} - F_{ii}F_{jj}\right) \qquad 3-5$$

$$I_3(Third\ Strain\ Invariant) = \det(F) = J$$

These parameters are called the strain invariants of deformation. These equations allow us to map the area and volume between the deformed and undeformed configurations.

Deformation gradient tensor is a measure of how a body changes under load but it cannot be used for strain characterization because it contains rigid body motions. To define a strain measure, we measure the change in length squared in a material vector while going from the reference configuration to the deformed configuration. This measure has to be independent of rigid body rotation.

$$(ds')^2 = dx_i'dx_j' \qquad 3-6$$

$$(ds)^2 = dx_i dx_j \qquad 3-7$$

Strain measure tells us how much a length of material has changed. It is the mapping that tells us how much a piece of material is squeezed or stretched while going from initial configuration to the deformed configuration.

The strain tensor can be calculated from the difference between $(ds)^2$ and $(ds')^2$.

$$(ds)^2 E_{ij} = \frac{1}{2}\left(F_{ki}F_{kj} - \delta_{ij}\right) \qquad 3-8$$

We consider an elastic material for which the elastic parameters are characterized in terms of strain energy function (per unit volume). $W = W(F)$ and defined in the space of deformation gradients. This theory is known as hyperelasticity. For an inhomogeneous material, i.e. one whose properties vary from point to point, W depends on X in addition to F, but in this thesis we assume that the materials are homogeneous within each tissue volume. Thus we define hyperelasticity on a homogeneous material.

For an unconstrained hyperelastic material the nominal stress is given by

$$S = H(F) = \frac{dW}{dF} \qquad 3-9$$

For an incompressible material this equation changes to the following:

$$S = \frac{dW}{dF} - pF^{-1} \qquad and \qquad \det(F) = 1$$

where p is the Lagrange multiplier associated with the incompressibility constraint and is referred to as the hydrostatic pressure.

The Cauchy stress tensor corresponding to equation 3-9 is given by:

$$\sigma = G(F) = J^{-1}F\frac{dW}{dF} \qquad 3-10$$

As for H, the form of G depends on the choice of reference configuration. G is a symmetric tensor function. For an incompressible material this equation changes to the following:

$$\sigma = F\frac{dW}{dF} - pI, \qquad 3-11$$

And $\det(F) = 1$.

W depends on the principal stretches and for an isotropic material this dependence is equivalent to W being regarded as a function (symmetric) of the principal invariants I_1, I_2, I_3. In terms of these invariants the Cauchy stress tensor for an unconstrained isotropic elastic material may be written as:

$$\sigma = \alpha_0 I + \alpha_1 B + \alpha_2 B^2 \qquad 3-12$$

where the coefficients α_0, α_1 and α_2, are functions of the strain invariants given by:

$$\alpha_0 = 2I_3^{1/2}\frac{\partial W}{\partial I_3},$$

$$\alpha_1 = 2I_3^{1/2}\left(\frac{\partial W}{\partial I_1} + I_1\frac{\partial W}{\partial I_2}\right),$$

$$\alpha_2 = 2I_3^{1/2}\frac{\partial W}{\partial I_2},$$

for an incompressible material the corresponding equation is [45]:

$$\sigma = -pI + \alpha_1 B + \alpha_2 B^2 \qquad 3-13$$

3.2. Strain Energy Function

The constitutive model of a hyperelastic model is defined on the basis of strain energy functions. The strain energy functions relate the displacements of the tissue to their corresponding stress values. These functions are defined as functions of strain invariants (I_1, I_2, I_3) and a number of parameters called the hyperelastic parameters.

There are several forms of strain energy function for solid rubber. Here some of the most commonly used strain energy functions will be introduced.

3.2.1. Neo-Hookean Model

According to Holzapfel *et al* [46], the Neo-Hookean model was first established by the study of vulcanized rubber, using statistical theory. In this approach the vulcanized rubber is seen as a 3-dimensional network of long chain molecules that are connected at a few points. This model is the simplest strain energy model and was proposed by Treloar in 1943 [47]:

$$U = C_{10}(\bar{I}_1 - 3) \qquad 3-14$$

where C_{10} is the hyperelastic parameter of the model. Typically $C_{10} = \frac{1}{2}\mu_0$, where μ_0 is the initial shear modulus. This model provides good approximation to the behavior of rubber-like materials.

3.2.2. Mooney-Rivlin Model

This model is well known for both historical reasons, as it was one of the first hyperelastic models, and also for its accuracy as it highly accurately predicts the non-linear behavior of isotropic rubber-like materials.

The strain energy function of this form can be expressed as:

$$U = C_{10}(\bar{I}_1 - 3) + C_{01}(\bar{I}_2 - 3) \qquad 3-15$$

Where C_{10} and C_{01} are the hyperelastic parameters and $C_{10} + C_{01} = \frac{1}{2}\mu_0$, where μ_0 is the initial shear modulus.

Mooney-Rivlin model is the most general form allowing linear relation between stress and strain in simple shear. This model provides better fit to experimental data than the Neo-Hookean form.

3.2.3. Ogden Model

This model is based on the Ogden's phenomenological theory of elasticity [48].

$$U = \sum_{i=1}^{N} \frac{2\mu_i}{\alpha_i^2}\left(\lambda_1^{\alpha_i} + \lambda_2^{\alpha_i} + \lambda_3^{\alpha_i} - 3\right) \qquad 3-16$$

This model has $N \times 2$ hyperelastic parameters. Ogden model often provides accurate representation of mechanical behavior of rubber-like materials for large ranges of deformation. It has been shown that excellent convergence between theoretical and experimental results for rubber are achieved when $N = 3$ [46].

3.2.4. Polynomial Model

The Polynomial strain energy function is given in the following equation:

$$U = \sum_{i+j=1}^{N} C_{ij}(\bar{I}_1 - 3)^i(\bar{I}_2 - 3)^j + \sum_{i=1}^{N} \frac{1}{D_i}(J_{el} - 1)^{2i} \qquad 3-17$$

For $N = 1$ Polynomial strain energy function take the form of Mooney-Rivlin strain energy function. Polynomial form with $N = 2$ is the most commonly used form of this strain energy function specially in modeling mechanical behavior of biological tissues. The initial shear modulus and bulk modulus for this model are defined as:

$$\mu_0 = 2(C_{10} + C_{01}), \qquad K_0 = \frac{2}{D_1},$$

For the incompressible materials the second term in the equation (3-17) becomes zero. This is due to the fact that for incompressible materials $J = 1$ (or $I_3 = 1$). Thus only first and second strain invariants are required for incompressibility.

3.2.5. Reduced Polynomial Model

This model is equivalent to the Polynomial form without considering the effect of the second strain invariant. This strain energy function is expressed as:

$$U = \sum_{i=1}^{N} C_{i0}(\bar{I}_1 - 3)^i + \sum_{i=1}^{N} \frac{1}{D_i}(J_{el} - 1)^{2i} \qquad 3-18$$

Since the Moony-Rivlin model has no dependence on $\bar{I}_2$ it is usually preferred over the full polynomial model, especially when there are limited data for calibration.

The Neo-Hooke strain energy function is a special case of the reduced polynomial model with $N = 1$.

3.2.6. Yeoh Model

The Yeoh material model for incompressible (rubber-like) materials was presented for the first time in 1990 [43]. The strain function that characterizes this model depends only on the first strain invariant ($\bar{I}_1$):

$$U = \sum_{i=1}^{3} C_{i0}(\bar{I}_1 - 3)^i \qquad 3-19$$

This strain energy function is a special case of the general reduced polynomial model with *N=3*. For the Yeoh model the initial shear modulus and bulk modulus are given by:

$$\mu_0 = 2C_{10}, \qquad K_0 = \frac{2}{D_1},$$

3.2.7. Veronda-Westmann Model

In 1970, Veronda and Westmann presented a new hyperelastic material model [49]. This model is based on uniaxial tests performed upon skin of cats. This model constitutes the basis for the recent study of the cirrhotic human liver [50].

Veronda-Westmann strain energy function depends on the invariants $\bar{I}_1$, $\bar{I}_2$ and $\bar{I}_3$ in its general form:

$$U = C_1\left[e^{C_3(\bar{I}_1-3)} - 1\right] - C_2(\bar{I}_2 - 3) + g(\bar{I}_3) \qquad 3-20$$

For incompressible materials such as soft tissues, $\bar{I}_3(or\ J_{el}) = 1$, so $g(\bar{I}_3) = 0$. This model has recently become more popular in modeling mechanical behavior of breast tissues and other soft tissues [44].

3.3. Regularization Techniques

In several fields of mathematics, in particular statistics, machine learning and inverse problems, regularization involves introducing additional information in order to solve ill-posed problems or prevent over fitting. This information is usually of the form of a penalty for complexity, such as restrictions for smoothness or bounds on the vector space norm.

A theoretical justification for regularization is that it attempts to impose Occam's razor on the solution. This principle states that the explanation of any phenomenon should make as few assumptions as possible, eliminating those that make no difference in the observable predictions of the explanatory hypothesis or theory. From a Bayesian point of view, many regularization techniques correspond to imposing certain prior distributions on model parameters.

The same idea arose in many fields of science. For example, the least-squares method can be viewed as a simple form of regularization. A simple form of regularization applied to integral equations, generally termed Tikhonov regularization after Andrey Nikolayevich Tychonoff, is essentially a trade-off between fitting the data and reducing a norm of the solution. More recently, non-linear regularization methods, including total variation regularization have become popular.

In this thesis, we are interested in applying regularization techniques to linear least square problems that arise in our application. Regularization is required to reconstruct the hyperelastic parameters of the soft tissue from the highly ill-posed system of equations resulting from the stress deformation relationship of the tissue.

3.3.1. Tikhonov Regularization Technique

Tikhonov regularization is the most commonly used method of regularization of ill-posed problems. In statistics, the method is also known as ridge regression. It is related to the Levenberg-Marquardt algorithm for non-linear least squares problems.

The standard approach to solve an over-determined system of linear equations given as

$$Ax = b, \qquad 3-21$$

is known as linear least squares and seeks to minimize the residual

$$\|Ax - b\|^2 \qquad 3-22$$

Where $\|\cdot\|$ is the Euclidean norm. However, the matrix A may be ill-conditioned or singular yielding a large number of solutions. In order to give preference to a particular solution with desirable properties, the regularization term is included in this minimization:

$$\|Ax - b\|^2 + \|\Gamma x\|^2 \qquad 3-23$$

for some suitably chosen Tikhonov matrix Γ. In many cases, this matrix is chosen as the identity matrix $\Gamma = \mathrm{I}$, giving preference to solutions with smaller norms. In other cases, high-pass operators (e.g. a difference operator or a weighted Fourier operator) may be used to enforce smoothness if the underlying vector is believed to be mostly continuous. This regularization improves the conditioning of the problem, thus enabling a numerical solution. An explicit solution, denoted by $\hat{x}$, is given by:

$$\hat{x} = (A^T A + \Gamma^T \Gamma)^{-1} A^T b \qquad 3-24$$

The effect of regularization may be varied via the scale of matrix Γ (e.g. $\Gamma = \alpha\mathrm{I}$). For $\Gamma = 0$ this reduces to the unregularized least squares solution provided that $(A^T A)^{-1}$ exists.

3.3.2. Truncated Singular Value Decomposition (SVD)

Suppose M is an m-by-n matrix whose entries come from the field K, which is either the field of real numbers or the field of complex numbers. Then there exists a factorization of the form

$$M = U\Sigma V^T, \qquad 3-25$$

where U is an m-by-m unitary matrix over K, the matrix Σ is m-by-n with nonnegative numbers on the diagonal (as defined for a rectangular matrix) and zeros off the diagonal, and V^T denotes the conjugate transpose of V, an n-by-n unitary matrix over K. Such a factorization is called a singular-value decomposition of M.

- The matrix V thus contains a set of orthonormal basis vector directions for M. Columns of V are called the right eigen-vectors of M.

- The matrix U contains a set of orthonormal basis vector directions for M. Rows of U are called the left eigen-values of M.
- The matrix Σ contains the singular values.

A common convention is to order the values $\Sigma_{i,i}$ in non-increasing fashion. In this case, the diagonal matrix Σ is uniquely determined by M (though the matrices U and V are not).

If the system equations given by $Ax = b$ is ill-conditioned, the ratio of the first eigen-value (the term $\Sigma_{1,1}$ in the singular value decomposition of A) to the last eigen-value (the term $\Sigma_{n,n}$ in the singular value decomposition of A), is a large number. This number is called the condition number of matrix A.

One way to solve the ill-conditioning of matrix A is to make this number smaller. To do this the smallest eigen-values of matrix A are eliminated. This results in having a larger value as the smallest eigen-value of A and consequently having smaller condition number for A. This new decomposition of matrix A is called the truncated SVD of A.

3.3.3. Wiener Filtering

Wiener filtering is similar to Tikhonov regularization and truncated SVD. In the truncated SVD, the smaller eigen-values are eliminated, this causes very significant alteration in the original coefficient matrix A. In the Tikhonov regularization, using Tikhonov matrices of the form $\Gamma = \alpha I$ alters all the eigen-values of A. This also causes considerable difference between the original and the regularized coefficient matrices. A Wiener filter is capable of altering one or more of the eigen-values of matrix A without changing the rest of them. This method uses the singular value decomposition of matrix

$A(A = VDU^T)$ and makes slight changes to selected eigen-values. The resultant approximate solution to the system $\hat{x}$ is calculated using equation the following equation:

$$\hat{x} = \sum_{i=1}^{q} f_i \frac{u_i^T b}{\sigma_i} v_i \qquad 3-26$$

where the Wiener weights are $f_i = \frac{\sigma_i^2}{\sigma_i^2+\alpha^2}$, in which α is the regularization factor and q is the rank of matrix A.

3.4. Non-linear Optimization Technique

A nonlinear system of equations is defined as a set of equations that are nonlinear in terms of the unknown parameters, or as two linear and nonlinear sets in terms of the parameters. For example, Gaussians, ratios of polynomials, and power functions are all nonlinear. In matrix form, nonlinear models are given by the formula

$$y = f(X, \beta) + \varepsilon \qquad 3-27$$

where

- y is an n-by-1 vector of responses or experimental measurements.
- f is a function of β and X. β is a m-by-1 vector of coefficients.
- X is the n-by-m parameters matrix for the system. The goal of solving the system is to find X.
- ε is an n-by-1 vector of errors.

Nonlinear systems are more difficult to solve than linear systems because the parameters cannot be estimated using simple matrix techniques. Instead, an iterative approach is required. In this thesis we used Trust region method to minimize the non-linear least square cost function. This trust region method uses a combination of steepest descent

method and Newton's method to find the Preconditioned Conjugate Gradient (PCG) method to find the Newton's direction to minimize the cost function.

3.4.1. Trust Region

In the standard trust-region method, the quadratic approximation to the cost function f is defined by the first two terms of the Taylor approximation to f at x; the neighborhood is usually spherical or ellipsoidal in shape. Mathematically, the trust-region sub-problem is typically stated as:

$$\min\left\{\frac{1}{2}s^{T}Hs+s^{T}g \ \text{ such that } \|Ds\|\leq\Delta\right\} \qquad 3-28$$

where g is the gradient of f at the current point x, H is the Hessian matrix (the symmetric matrix of second derivatives), D is a diagonal scaling matrix, Δ is a positive scalar, and $\|.\|$ is the 2-norm.

Several approximation and heuristic strategies, based on Equation 3-28, have been proposed in the literature [51, 52]. The approximation approach used here is to restrict the trust-region sub-problem to a two-dimensional subspace [51, 53]. Once the subspace has been computed, the work to solve Equation 3-28 is trivial even if full eigenvalue/eigenvector information is needed (since in the subspace, the problem is only two-dimensional).

The two-dimensional subspace S is determined with the aid of a preconditioned conjugate gradient process described below. The method assigns $S = \langle s_1, s_2 \rangle$, where s_1 is in the direction of the gradient g, and s_2 is either an approximate Newton direction, i.e., a solution to

$$H \cdot s_2 = -g \qquad 3-29$$

or a direction of negative curvature,

$$s_2^T \cdot H \cdot s_2 < 0 \qquad 3-30$$

The philosophy behind this choice of S is to force global convergence (via the steepest descent direction or negative curvature direction) to achieve fast local convergence (via the Newton step, when it exists).

3.4.2. Preconditioned Conjugate Gradient Method

We want to solve the following system:

$$Ax = b, \qquad 3-31$$

where A is a n × n symmetric definite and positive matrix ($A^T = A$ and $x^T Ax > 0$, for all non zero $x \in \mathbb{R}^n$). Let x_* be the exact solution of this system.

It happens sometimes that the condition number of A ($\kappa(A)$) is too high (eigen-values are not well distributed). Preconditioning consists of introducing regular matrix $C \in M_n(R)$ and solving the system:

$$C^{-1}(Ax) = C^{-1}b \Leftrightarrow Ax = b \qquad 3-31$$

such that the new condition number is smaller for a judicious choice of the matrix C.

Let $x_0 \in \mathbb{R}^n$ be an initial vector, Preconditioned Gradient Method algorithm is the following:

$$r_0 = b - Ax_0$$

$$z_0 = C^{-1}r_0$$

$$d_0 = z_0$$

For $k = 0,1,2, \ldots$

$$\alpha_k = \frac{z_k^T \tau_k}{d_k^T A d_k}$$

$$x_{k+1} = x_k + \alpha_k d_k$$

$$r_{k+1} = r_k - \alpha_k A d_k$$

$$z_{k+1} = C^{-1} r_{k+1}$$

$$\beta_{k+1} = \frac{z_{k+1}^T r_{k+1}}{z_k^T r_k}$$

$$d_{k+1} = z_{k+1} + \beta_{k+1} d_k \qquad 3-32$$

There exist different pre-conditioner matrices some of them are as follows.

3.4.2.1. Jacobi Pre-conditioner

Jacobi Pre-conditioner consists of taking the diagonal of A for the matrix C, i.e.

$$C_{ij} = \begin{cases} A_{ii} & \text{if } i = j \\ 0 & \text{elsewhere} \end{cases} \qquad 3-33$$

Advantages of such pre-conditioner are the ease of its implementation and the low memory it requires. However, we can find other pre-conditioners such that resolution of the linear system is fastest; it is the case of the SSOR Pre-conditioner which is used in this thesis for solving the optimization problem.

3.4.2.2. SSOR Pre-conditioner (Symmetric Successive Over Relaxation)

We decompose the symmetric matrix *A* as follows:

$$A = L + D + L^T \qquad 3-34$$

where L is the strictly lower part of A and D is the diagonal of A. SSOR Pre-conditioner consists of taking

$$C = \left(\frac{D}{\omega} + L\right)\frac{\omega}{2-\omega}D^{-1}\left(\frac{D}{\omega} + L^{T}\right) \qquad 3-35$$

where ω is a relaxation parameter. A necessary and sufficient condition of the pre-conditioned gradient method algorithm is to fix the parameter ω in the interval $]0,2[$.

3.5. Structure of the remainder of the thesis

The next chapter talks about the methodology used to perform reconstruction. It involves information about the different phantoms that are constructed in this research and the way the theoretical part that are presented up to know are used to formulate the reconstruction algorithm. The Methods chapter is followed by the Result chapter that gives the results of applying the reconstruction technique to the numerical model and the experimental phantoms.

The final chapter is summary, conclusions and discussions in which we talk about the different models used in the study and the advantages and disadvantages of each model. It also talks about the difficulties and issues that we faced in our research and provides some future works for extension of my current study.

4. Methods

4.1. Phantom Study

4.1.1. Building gelatin phantom

In order to verify the results of the reconstruction method, that will be described later, first a phantom was built using gelatin. Gelatin exhibits linear mechanical behavior and is suitable for testing the method on linear behavior. To build tissue mimicking phantom using gelatin, the gelatin is dissolved in water. The stiffness of the tissue depends on the amount of gelatin added to the water. In this experiment we used Gelatin from bovine skin, type B, 225 bloom.

The phantom is a cubic phantom with dimensions: 16mm height, 64mm width and 64mm length. The phantom consists of three different tissue types to represent the three existing tissue types in a cancerous breast tissue (the tumor tissue, the fibloglandular tissue and the adipose tissue).

The inner part that represents the tumor tissue has a cylindrical shape. This tissue has the highest stiffness. The middle part is cubic and represents the fibroglandular tissue. The stiffness of this tissue is lower than the tumor tissue but it is stiffer than the outer part of the phantom. The outer part of the phantom that has cubic shape represents the adipose tissue. This tissue is the softest tissue in the phantom. The gelatin based phantom is depicted in Figure 4-1.

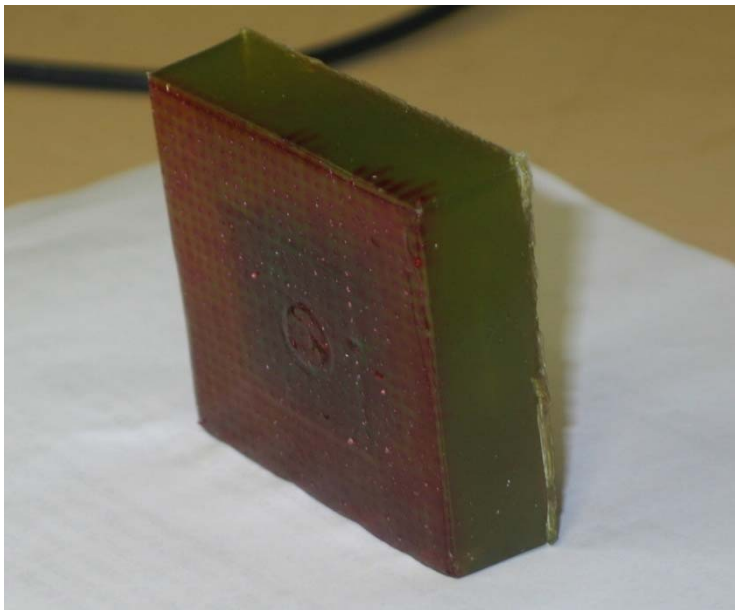

Figure 4-1 Phantom made by gelatin, which consists of three different tissue types. The two outer and middle cubic portions represent the adipose and fibroglandular tissue in the breast while the inner cylindrical part represents a breast tumor

The Young's modulus of the gelatin based phantom (the tumor tissue, the fibroglandular tissue and the adipose tissue) were measured independently from uniaxial load test data on cylindrical gelatin samples using an electromechanical system developed by Samani *et al* [54]. Figure 4-2 shows the cylindrical samples that were made for use in uniaxial compression process.

Figure 4-2. Cylindrical samples of each tissue type made for use in uniaxial compression process. Uniaxial compression is performed to independently measure the mechanical behavior of the tissues in the phantom.

The Young's Moduli of the three tissues are as follows: $E_1 = 110\ kPa$, $E_2 = 120\ kPa$, $E_3 = 230\ kPa$. The E_1 stiffness value is acquired by dissolving $12g$ gelatin powder in $50ml$ water. The E_2 and E_3 are acquired by adding $15g$ and $25g$ gelatin powder to $50ml$ water respectively.

In this study we are just performing a proof of concept type of analysis, thus the value of mechanical properties of the tissues are different from the values for real breast tissue. The ratio of the stiffness of tumor to the stiffness of other parts in the phantom is too low to represent the real situation.

4.1.2. Building a phantom from Polyvinyl Alcohol (PVA)

The gelatin based phantom that was made and described in the previous part has linear mechanical behavior. In order to verify that the method works for reconstructing hyperelastic parameters of soft tissues, a phantom with hyperelastic behavior is required. Therefore, the fabrication of this type of phantom will be described.

Polyvinyl Alcohol (PVA) is a material that is widely used for constructing tissue mimicking phantoms. Although this material is has been used for tissue mimicking purposes, it has not been used as a model for characterizing hyperelastic behavior of tissues. This is the first time that this material is being used for modeling the mechanical behavior of tissues and we are the first group to take advantage of this unique property of PVA.

To make the phantom, PVA is first resolved in deionized water. The stiffness of the material is determined according to the concentration of PVA in water and the type described as the percentage of the PVA to the mass of the whole gel. For example

$30\%\ PVA$ (if the whole gel is $300ml$) is made up of 90 grams PVA powder added to $210\ ml$ deionized water.

In order for the mixture of PVA powder and water to make the gel, it is cooked for about 45 minutes to one hour. The temperature of the system must not exceed 90 degrees (centigrade) or the PVA burns and sticks to the container. This also adds bubbles to the gel which is not desirable. Bubbles ruin the uniformity of the PVA sample when it is made; it also changes the mechanical properties of the sample. Thus one must prevent having bubble in the sample.

To be able to keep the phantom in room temperature 0.02% biocide is added to the PVA. The stiffness of the PVA depends on two factors, one is the PVA concentration or the amount of PVA powder added to water. The second factor is the number of Freeze-Thaw Cycles (FTC) that the PVA goes through. Freeze-Thaw Cycle is a process in which the PVA gel is frozen and then thawed systematically so that the PVA crystals form. An environmental chamber is used to perform this process. The chamber's temperature decreases gradually starting from the room temperature and goes down to -20^{o} (C). This decrease in the temperature takes place gradually and with constant speed. The profile of temperature changes as shown in Figure 4-3. One FTC takes about 14 hours in which the temperature decreases from +20 (C) to -20^{o} (C), stays in -20^{o} for a specified duration and then increases from -20^{o} (C) to +20^{o} (C).

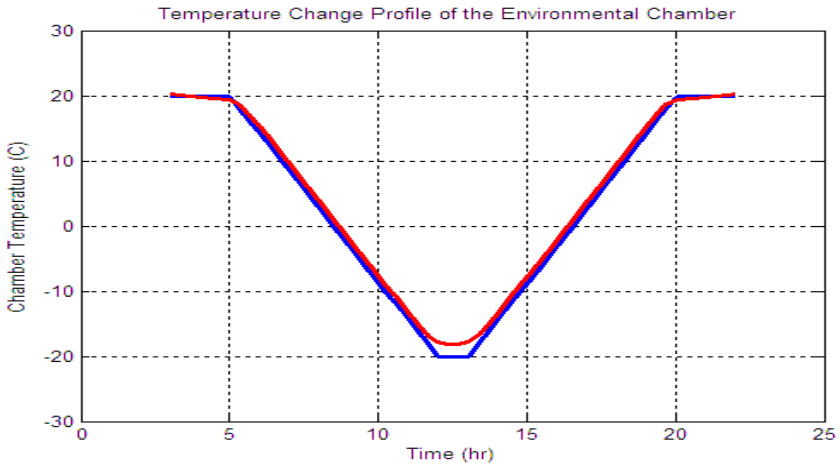

Figure 4-3. Temperature change profile of the environmental chamber for one Freeze-Thaw cycle which takes approximately 14 hours

FTC's are required for the gel to form. Typically more than one FTC is required for a gel to solidify and make the phantom since the crystals in PVA form during the second FTC and in the first cycle only a number of these crystals are formed.

The more the number of FTC's the stiffer the samples. The phantom that we made for the experiment has the following characteristics. The inclusion, which is the stiffest part, is 10% PVA and 5 FTC's. The middle block of the phantom is made up of 5% PVA and 3FTCs' and the outer block is constructed using 5% PVA and 2 FTC's. This phantom is shown in Figure 4-4.

Figure 4-4. The PVA phantom, which consists of three different tissue types. Two outer and middle cubic portions represent the adipose and fibroglandular tissue of the breast while the inner cylindrical part represents a breast tumor.

The phantom was constructed in 3 steps. The first step was making a cylindrical tissue made up of 10% PVA and 0.02% biocide with 2 FTC's. the cylindrical phantom has the dimensions of 1 cm diameter and 7.7 cm height. This tissue is then placed in the mould of middle tissue. The cylinder is placed in the middle and the 5% PVA solution is poured in the mould to cover the inner tissue. The liquid temperature must be 55 degrees (Centigrade) or less in order not to melt the cylindrical tissue. This combination was placed in the environmental chamber for 1 FTC. The third step was placing this tissue in the large mould (in the middle of the mould) and pouring 5% PVA solution around it. This combination underwent 2 FTC's.

Using this procedure the phantom with the specified specification was made. This process was required to make the phantom and also having bounding between the three tissue types of the phantom. The moulds that were used to make this phantom are shown in Figure 4-5.

Once the phantom is made, since its height is too much for the plane stress state, is was cut to have height of 2 cm. The final phantom was shown in Figure 4-4.

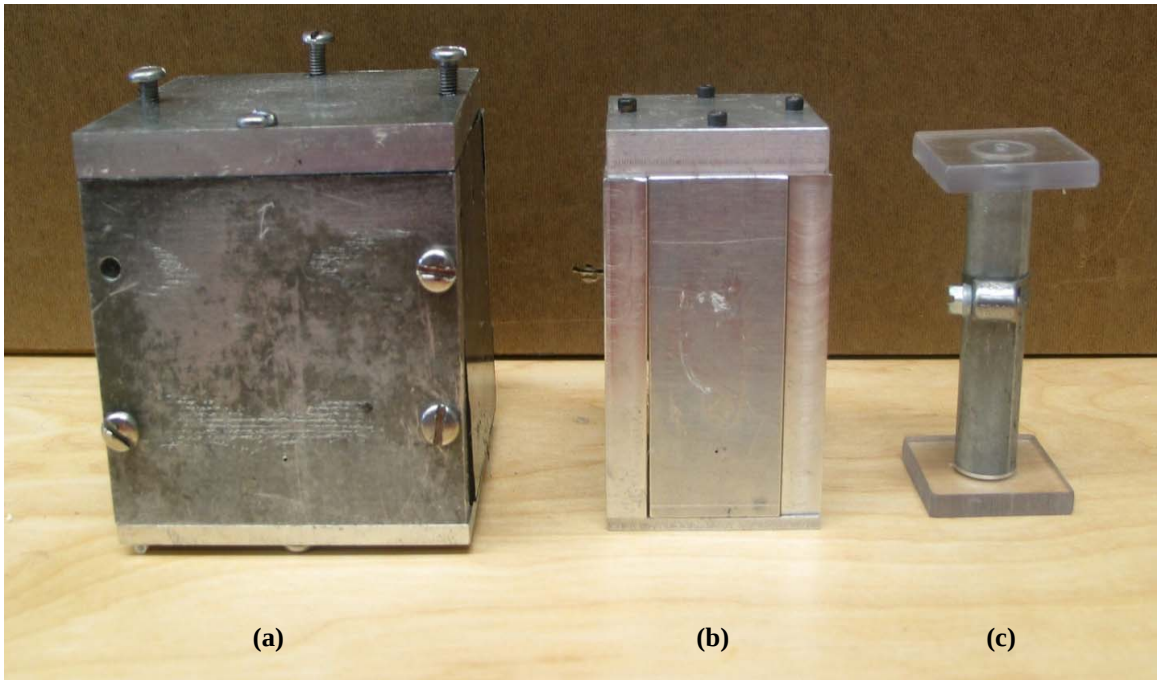

Figure 4-5 the moulds that were used to construct the experimental phantom, a) the mould used for constructing the large block of the phantom, b) the mould used for constructing the middle block of the phantom and c) the cylindrical mould that was used for constructing the inner part of the phantom.

One difficulty in the phantom construction process, apart from finding appropriate PVA concentrations was the moulds themselves. Due to the variations in the volume of the PVA solution when it undergoes the freezing and thawing cycles. The volume of the solution increases as while the volume of the Aluminum mould does not change

significantly. Thus the bolts of the mould would break during this process. The solution for this problem was using strong bolts of large diameter and using stainless steel. Although we used strong bolts, still there were some deformations in the shape of the mould which may affect the freezing and thawing process.

4.1.3. Uniaxial testing for gelatin and PVA materials

In order to validate the results of the reconstruction, it is required to find the mechanical properties of the tissues independently. Therefore, cylindrical samples of each tissue type were made to be used in uniaxial loading tests.

The general form of a finite deformation is defined by a second order tensor, commonly known as deformation gradient.

$$\mathrm{F_{aA}} = \frac{\partial \mathrm{x_a}}{\partial \mathrm{x_A}}\,, \qquad \mathrm{a, A} = 1,2,3. \qquad\qquad 4-1$$

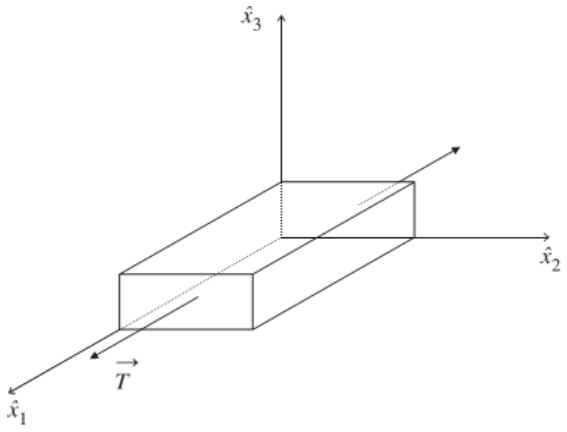

Figure 4-6. Uniaxial stretching of a tissue sample

The particular form of F in the case of hyperelastic materials subjected to a uniaxial tension is:

$$\mathrm{F} = \begin{bmatrix} \lambda & 0 & 0 \\ 0 & \frac{1}{\sqrt{\lambda}} & 0 \\ 0 & 0 & \frac{1}{\sqrt{\lambda}} \end{bmatrix} \qquad 4-2$$

Assuming that the stress is applied along the $\hat{\mathrm{x}}_1$ direction (Figure 4-6), taking $\lambda_1 = \lambda$ and taking into account the incompressibility condition:

$$J = \prod_{i=1}^{3} \lambda_i = \det(F) = 1 \qquad 4-3$$

Requires that $\lambda_2 = \lambda_3 = \frac{1}{\sqrt{\lambda}}$.

$$I_1 = \lambda_1^2 + \lambda_2^2 + \lambda_3^2 = \lambda^2 + \frac{2}{\lambda}, \qquad 4-4$$

According to Holzapfel [46], in the case of uniaxial tension, the Cauchy stress $\sigma = \sigma_1$ as a function of strain invariants, if the directions of the principal stretches are oriented with the coordinate basis vectors, is:

$$\sigma_{11} = -p + 2\lambda^2 \left(\frac{\partial U}{\partial I_1} + \frac{1}{\lambda}\frac{\partial U}{\partial I_2}\right), \qquad 4-5$$

$$\sigma_{22} = -p + \frac{2}{\lambda}\left(\frac{\partial U}{\partial I_1} + \frac{1}{\lambda}\frac{\partial U}{\partial I_2}\right) = \sigma_{33} \qquad 4-6$$

since $\sigma_{22} = \sigma_{33} = 0$, we have:

$$p = \frac{2}{\lambda}\left(\frac{\partial U}{\partial I_1} + \frac{1}{\lambda}\frac{\partial U}{\partial I_2}\right), \qquad 4-7$$

$$\Rightarrow \sigma_{11} = 2\left(\lambda^2 - \frac{1}{\lambda}\right)\left(\frac{\partial U}{\partial I_1} + \frac{1}{\lambda}\frac{\partial U}{\partial I_2}\right), \qquad 4-8$$

The uniaxial nominal stress is:

$$T_{11} = {}^{\sigma_{11}}/_{\lambda} = 2\left(\lambda - \frac{1}{\lambda^2}\right)\left(\frac{\partial U}{\partial I_1} + \frac{1}{\lambda}\frac{\partial U}{\partial I_2}\right) \qquad 4-9$$

The uniaxial nominal stress for the Polynomial model can be calculated by the following equation

$$T_{11} = 2(1-\lambda^{-3})\Big(\lambda C_{10} + C_{01} + C_{11}\big(\lambda(\bar{I}_2 - 3) + (\bar{I}_1 - 3)\big) + 2\lambda C_{20}(\bar{I}_1 - 3) + 2C_{02}(\bar{I}_2 - 3)\Big)$$

The uniaxial nominal stress for the Yeoh model can be calculated by the following equation

$$T_{11} = 2(1-\lambda^{-3})(\lambda C_{10} + 2\lambda C_{20}(\bar{I}_1 - 3) + 3\lambda C_{30}(\bar{I}_1 - 3)^2)$$

The uniaxial nominal stress for the Veronda-Westmann model can be calculated by the following equation

$$T_{11} = 2(1-\lambda^{-3})\big(C_1 C_3 exp\big(C_3(\bar{I}_1 - 3)\big) + C_2\big)$$

4.1.4. Plane Stress Assumption

The phantom shape is made in a way that it is close to plane stress situation. The dimensions of the phantom are $2cm \times 6.1cm \times 6.3cm$. The thickness is small compared to its other dimensions, thus we can assume that the system performs like plane stress condition.

Plane stress assumption is used here to convert the 3-D analysis to a simple 2-D plane stress analysis. 3-D analysis is time consuming since our reconstruction algorithm involves employing a FE software (ABAQUS-commercial FE software) to solve the finite element problem using hyperelastic formulation on a 3-D tissue at each iteration while performing 2-D finite element analysis is much faster. Another advantage of using the plane-stress assumption is simplification of the image processing step required to estimate tissue displacements. Here we assume that the deformations of the nodes along

the direction of thickness are the same. Using this assumption, only the displacements of the nodes on the surface are needed and the analysis can be performed on the surface of the phantom.

To validate the accuracy of the plane stress assumption, a numerical study was performed using ABAQUS software. The geometry of the phantom as shown in the Figure 4-7b is the same as our experimental phantom. It is comprised of three different tissue types, the inner tissue is cylindrical with diameter of 1 cm and depth of 2 cm. The middle tissue type is cubic with depth of 2 cm and height and width of 3.1 cm. The outer part is also cubic with depth if 2 cm amd height and width of 6.3 cm and 6.1 cm respectively. The properties of the tissues are also the one that are calculated for the three experimental tissue types derived from uniaxial compression tests. The displacements of the surface nodes of a 3-D phantom were compared to the displacements of the nodes in plane stress state. Figure 4-7 shows the displacement field of the plane stress state (Figure 4-7a) and the displacement field for the 3-D model of the phantom (Figure 4-7b).

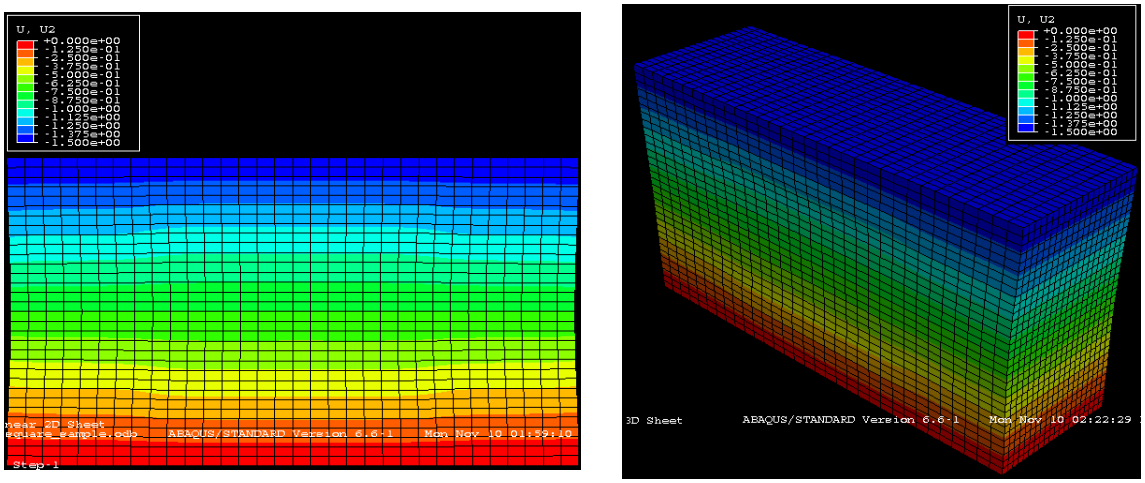

(a) **(b)**

Figure 4-7 a) the displacement field of the plane stress state and b) the displacement field for the 3-D model of the phantom

The error in the displacements are given in Table 4-1.

Table 4-1. The mean and maximum error in displacement calculations in 2-D model versus 3-D model for both X-axis and Y-axis.

	Mean value of displacement (X-axis)	**Max value of displacement (X-axis)**	**Mean value of displacement (Y-axis)**	**Max value of displacement (Y-axis)**
2-Dimensional model	0.2357 (cm)	0.4805 (cm)	0.75 (cm)	1.5(cm)
3-Dimensional model	0.2276 (cm)	0.4690 (cm)	0.75 (cm)	1.5(cm)
Error percent b/w two models	0.3615%	2.6861 %	3.5735%	5.3018%

As shown in the table above, the error in the displacement for the surface of the phantom compared to that of the plane stress state is less than 5% which means that this assumption is valid. Thus we use this assumption for designing our experiment.

4.1.5. Loading the Phantom

In order to reconstruct the hyperelastic parameters of the tissue, the phantom undergoes finite deformation (30% compression in this case). Once the phantom was deformed the displacement field of deformation was acquired. Hence, this field was fed to the iterative optimization routine to find the parameters characterizing the non-linear behavior of the tissue.

The phantom used in this research has a cubic shape (shown in Figure 4-8), the dimensions of which are as follows:

$$h(Hieght) = 6.3\ (cm)$$

$$w(Width) = 6.1\ (cm)$$

$$d(depth) = 2\ (cm)$$

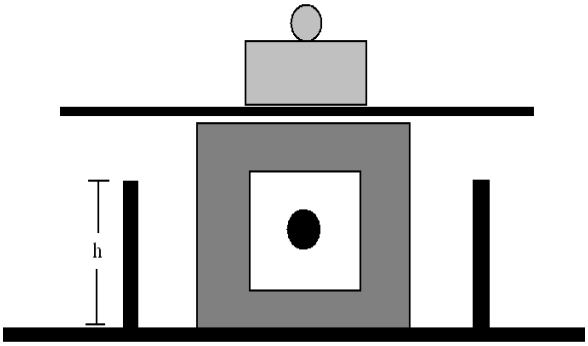

Figure 4-8. The schematic of the set up for applying the load. The horizontal plane is used to apply compression and the two vertical planes are placed to constrain the amount of compression

The 30% compresive load is applied to the phantom along the height direction, the schematic of the set up for applying the load is given in Figure 4-8. In this figure the horizontal plane is used to apply compression and the two vertical planes are placed to constrain the amount of compression being applied to the phantom. A photo of the setup used in the experiment is depicted in Figure 4-9.

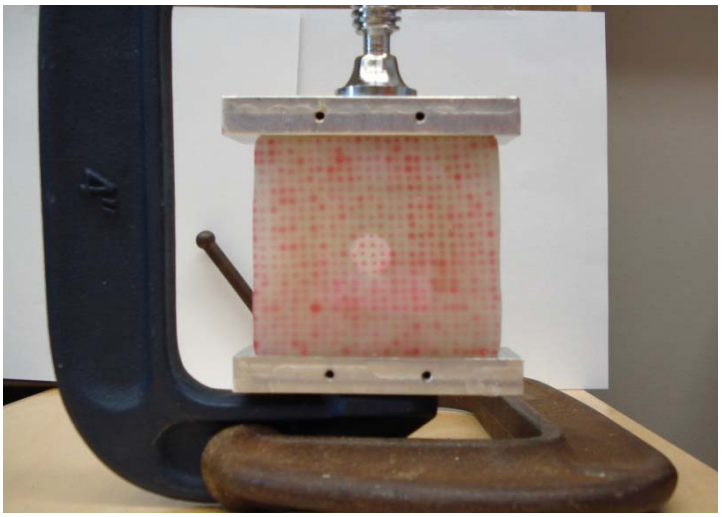

Figure 4-9. A photo of the setup used in the experiment

4.1.6. Meshing and displacement tracking

The iterative reconstruction process requires measuring the displacement of each point in the phantom as it undergoes deformation. These deformations are required to be compared with the results of the FE (Finite Element) solver. To model the phantom in the FE solver, in general, a 3-D mesh is required. However, using the plane stress assumption, we just need to track the displacements of the nodes lying on the surface of the phantom. For the phantom's displacements data acquisition, one possibility is using imaging such as US or MRI. With US, it is possible to use RF signal correlation methods while with MRI phase imaging maybe used to acquire tissue displacements. In this research, we used a simple inexpensive displacement tracking method, which involves placing a 2-D mesh on the phantom's surface and tracking the nodal displacements by manually processing photos of the undeformed and deformed phantom.

We placed a 25×24 grid on the phantom manually in a way that its nodes form 4-noded rectangular elements on the phantom. Then a photo of the phantom was taken

using a digital camera. The phantom was compressed using the set up described in the previous section and a new image was taken using the same digital camera and from the same distance. In this experiment we applied 30% compression to the phantom with zero displacement boundary condition at the bottom. The photos of the phantom before and after compression are depicted in Figure 4-10.

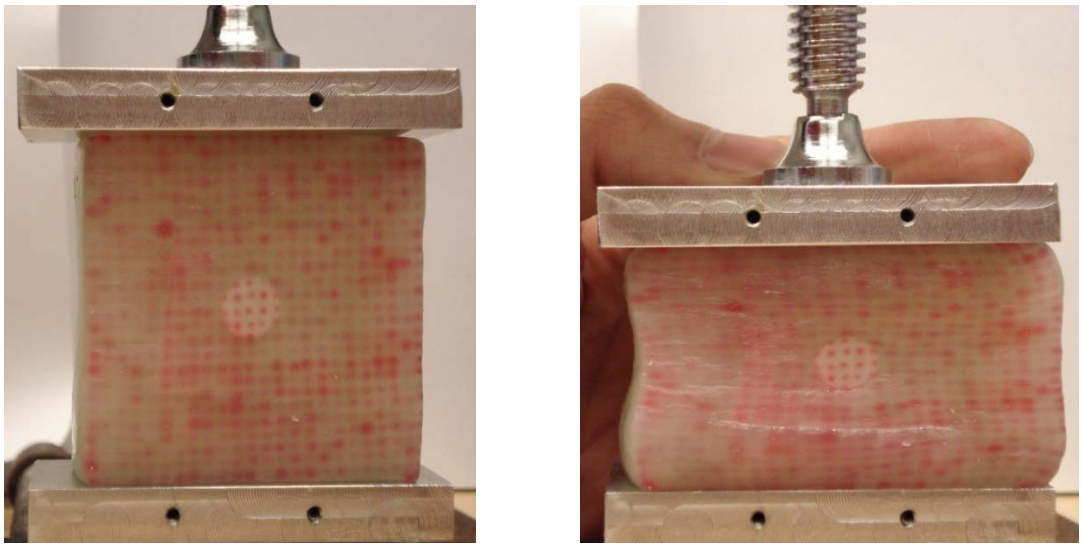

(a) **(b)**

Figure 4-10. a) Image of the phantom before compression and b) image of the phantom after compression

Once we had the images of pre- and post-compression stages, we extracted the location of each point in the pre-compression image and the location of its corresponding point in the post compression image manually, and measured its displacement using subtraction.

In order to extract the displacements, we took digital photos of both pre-compressed and post-compressed tissues. Then we imported these images to MATLAB. Using this software we extracted the pixel location of each point of our mesh and using the

dimensions of the phantom, we translated these pixel locations into the location of the point on the phantom.

A section of the pre-compressed image is shown in Figure 4-11. In this figure the points that are placed on the phantom can be clearly seen. We performed the manual point location extraction 10 times to minimize the human error in locating the nodes.

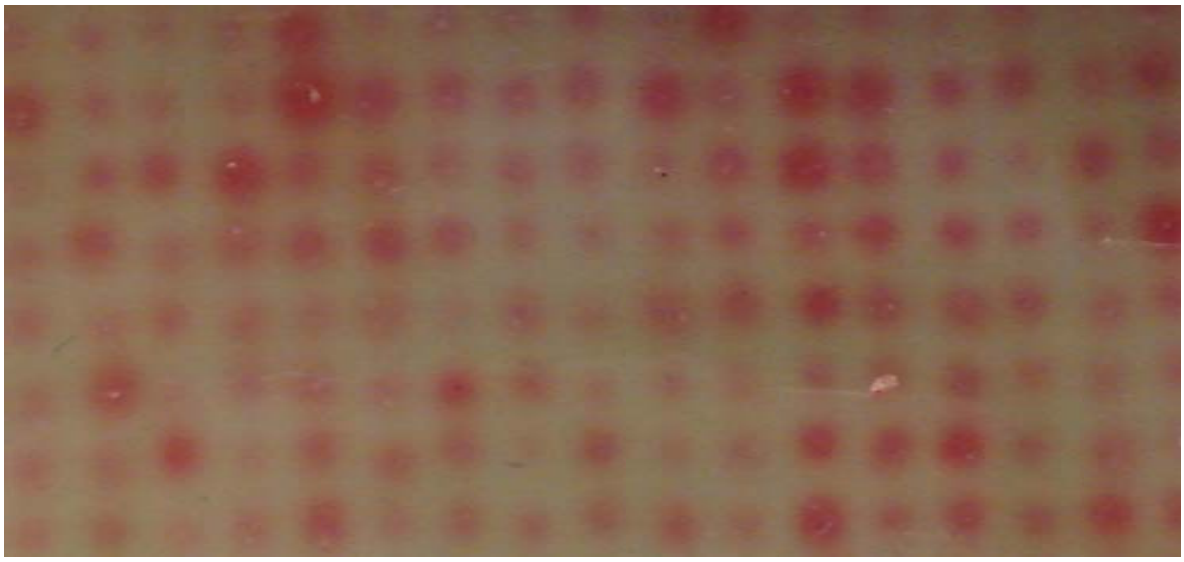

Figure 4-11. A section of the pre-compressed image. In this figure the points that are placed on the phantom can be clearly seen.

Figure 4-12 shows the mesh extracted for the pre- and post- compression images. These meshes were used to model the phantom in the ABAQUS finite element solver. They were also used in the iterative process to reconstruct the hyperelastic parameters of the tissue.

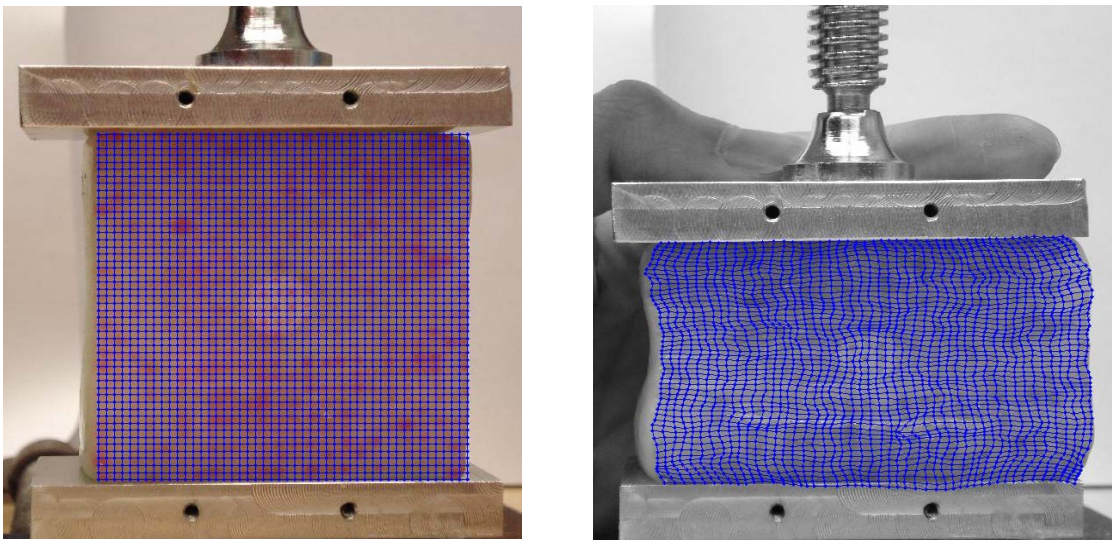

(a) **(b)**

Figure 4-12. a) The mesh extracted for the pre-compression image, and b) the mesh extracted for the post-compression image

4.1.7. Iterative Hyperelastic Parameters Reconstruction

To reconstruct the tissues' hyperelastic parameters, two images are required. The pre-compression and the post-compression images of the phantom. The deformations of the tissue while undergoing compression are extracted using these two images. The data acquisition process is done manually as described in the earlier sections.

For validating our reconstruction technique, we used numerical and experimental breast phantoms. For the numerical phantom, displacement data were generated using ABAQUS finite element solver. After applying simulated compression to the phantom, we calculated the displacements at each point using finite element analysis with the known geometry and boundary conditions. The type of compression used in this study is displacement boundary condition. For this numerical study, we used a 3-D phantom with

zero displacement boundary condition at the bottom and known displacement boundary condition at the moving nodes. In the experimental case, since we are interested in the displacements of the surface nodes, we employed a 2-D model of the surface of the phantom using plane stress state. In this case, we used 4-noded rectangular elements for modeling.

The hyperelastic parameter reconstruction algorithm is iterative and involves parameter updating followed by finite element analysis for stress calculation in each iteration. The algorithm assumes initial guesses for the hyperelastic parameters of the tissues, and using the known geometry and boundary conditions; it simulates the compression by ABAQUS and calculates the stress distribution. Hence, using the displacement data extracted from comparing the two pre- and post-compression images, and using the stress-deformation relationship for hyperelastic materials, the hyperelastic parameters were updated iteratively until convergence was reached. The iterative parameter reconstruction process is summarized in the flowchart in Figure 4-13.

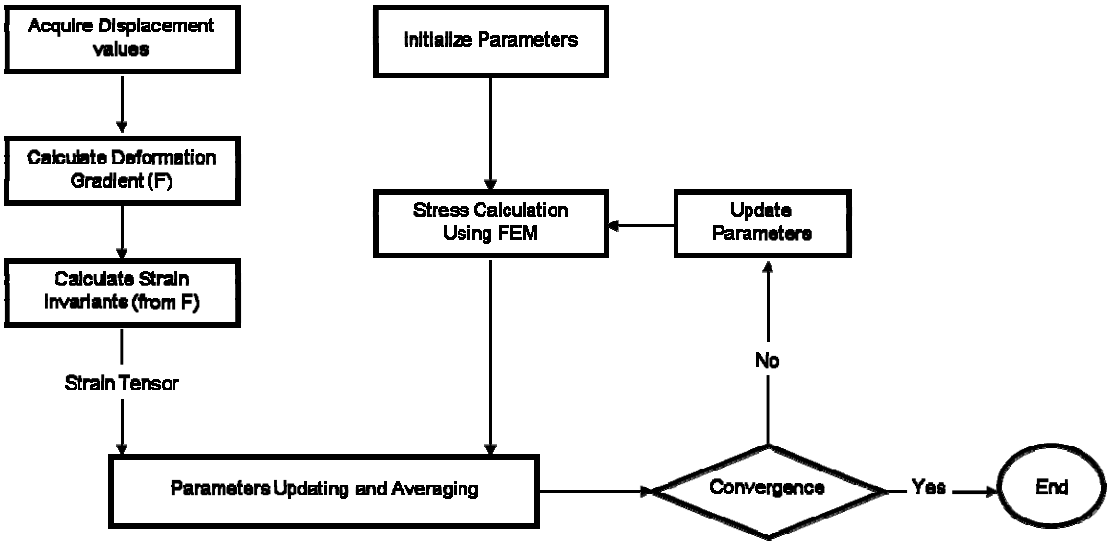

Figure 4-13. Flow chart illustrating the procedure of iterative reconstruction of hyperelastic parameters

The iterative process begins with an initial guess for the five (for Polynomial model) or three (for Yeoh and Veronda-Westmann models) unknown hyperelastic parameters of the tumor. ABAQUS is then employed for stress calculation using the known boundary conditions, the initial guess and the FE mesh generated from the segmented tissues. This is followed by updating the parameters using strain energy function defined in equations 3-17, 3-19 or 3-20 and the stress-deformation relationship given in equation (4-10).[46]

$$\sigma = \frac{2}{J} DEV\left[\left(\frac{\partial U}{\partial \bar{I}_1} + \bar{I}_1 \frac{\partial U}{\partial \bar{I}_2}\right)\bar{B} - \frac{\partial U}{\partial \bar{I}_2}\bar{B}\cdot\bar{B}\right] - pI \qquad 4-10$$

where DEV represents the deviatoric part of the stress tensor, p is hydrostatic pressure, I is the identity matrix and B is defined as

$$\bar{B} = \bar{F}\cdot\bar{F}^T \qquad 4-11$$

where F is the deformation gradient tensor that describes the displacement of each point after compression. In this equation, F is defined as follows for separating the volumetric and deviatoric effects

$$\bar{F} = J^{-1/3}F \qquad 4-12$$

$$J = \det(F)$$

This follows the definition of alternate forms of the strain invariants I_1 and I_2 as follows:

$$\bar{I}_1 = tr(\bar{B}) \qquad 4-13$$

$$\bar{I}_2 = \frac{1}{2}\left(\bar{I}_2^{\,2} - tr(\bar{B}\cdot\bar{B})\right) \qquad 4-14$$

For each element, equation (4-10) was rearranged in the following form:

$$\{\sigma\} = [A]\{C\} \qquad 4-15$$

where $\{\sigma\}$ is the element stress tensor, $[A]$ is the coefficients matrix formed using nodal displacements and F tensor, and $\{C\}$ is the unknown hyperelastic parameters vector.

Using equation (4-15), the values of C_{ij} were calculated using a least squares method. This yields a set of parameters for each element in the mesh. Averaging these values over the entire volume of the tumor tissue results in the updated parameters of the tissue.

The expanded form of equation (4-15) for the Yeoh model is given in the following

$$\text{equation} \begin{bmatrix}\sigma_{11}\\ \sigma_{12}\\ \sigma_{13}\\ \sigma_{21}\\ \sigma_{22}\\ \sigma_{23}\\ \sigma_{31}\\ \sigma_{32}\\ \sigma_{33}\end{bmatrix} = \frac{2}{J}\left[\begin{bmatrix}1, & 2(\bar{I}_1-3), & 3(\bar{I}_1-3)^2\end{bmatrix}\begin{bmatrix}C_{10}\\ C_{01}\\ C_{20}\\ C_{11}\\ C_{02}\end{bmatrix}\begin{bmatrix}b_{11}\\ b_{12}\\ b_{13}\\ b_{21}\\ b_{22}\\ b_{23}\\ b_{31}\\ b_{32}\\ b_{33}\end{bmatrix}\right] - p\begin{bmatrix}1\\0\\0\\0\\1\\0\\0\\0\\1\end{bmatrix}$$

The expanded form of equation (4-15) for the Polynomial model is given in the following equation

$$\begin{bmatrix}\sigma_{11}\\ \sigma_{12}\\ \sigma_{13}\\ \sigma_{21}\\ \sigma_{22}\\ \sigma_{23}\\ \sigma_{31}\\ \sigma_{32}\\ \sigma_{33}\end{bmatrix} = \frac{2}{J}\left[\begin{bmatrix}1, & \bar{I}_1, & 2(\bar{I}_1-3), & (\bar{I}_2-3)+\bar{I}_1(\bar{I}_1-3), & 2\bar{I}_1(\bar{I}_2-3)\end{bmatrix}\begin{bmatrix}C_{10}\\ C_{01}\\ C_{20}\\ C_{11}\\ C_{02}\end{bmatrix}\begin{bmatrix}b_{11}\\ b_{12}\\ b_{13}\\ b_{21}\\ b_{22}\\ b_{23}\\ b_{31}\\ b_{32}\\ b_{33}\end{bmatrix}\right.$$

$$\left. - \begin{bmatrix}0, & 1, & 0, & (\bar{I}_1-3), & 2(\bar{I}_2-3)\end{bmatrix}\begin{bmatrix}C_{10}\\ C_{01}\\ C_{20}\\ C_{11}\\ C_{02}\end{bmatrix}\begin{bmatrix}B_{11}\\ B_{12}\\ B_{13}\\ B_{21}\\ B_{22}\\ B_{23}\\ B_{31}\\ B_{32}\\ B_{33}\end{bmatrix}\right] - p\begin{bmatrix}1\\0\\0\\0\\1\\0\\0\\0\\1\end{bmatrix}$$

The expanded form of equation (4-15) for the Veronda-Westmann model is given in the following equation

$$\begin{bmatrix}\sigma_{11}\\ \sigma_{12}\\ \sigma_{13}\\ \sigma_{21}\\ \sigma_{22}\\ \sigma_{23}\\ \sigma_{31}\\ \sigma_{32}\\ \sigma_{33}\end{bmatrix} = \frac{2}{J}\left[\left[C_1C_3\ exp\left(C_3(\bar{I}_1-3)\right)+C_2\bar{I}_1\right]\begin{bmatrix}b_{11}\\ b_{12}\\ b_{13}\\ b_{21}\\ b_{22}\\ b_{23}\\ b_{31}\\ b_{32}\\ b_{33}\end{bmatrix} - [C_2]\begin{bmatrix}B_{11}\\ B_{12}\\ B_{13}\\ B_{21}\\ B_{22}\\ B_{23}\\ B_{31}\\ B_{32}\\ B_{33}\end{bmatrix}\right] - p\begin{bmatrix}1\\ 0\\ 0\\ 0\\ 1\\ 0\\ 0\\ 0\\ 1\end{bmatrix}$$

4.1.8. Inverse problem

An inverse problem consists of using the actual result of some measurements to infer the values of the parameters that characterize the system. Unlike forward problem, an inverse problem does not necessarily have a unique solution. In the problem of interest we have characterized the system via some constants ($C_{ij}\,'s$ in equation (4-15)) and the purpose is to find these system parameters using the displacement data acquired from the pre and post compression stages.

Using a least squares method to solve the inverse problem, we encounter equation (4-16) to calculate the parameters at each iteration.

$$C = (A^TA)^{-1}A^T\sigma \qquad 4-16$$

Equation (4-16) requires calculating the inverse of matrix (A^TA), which is not always possible. $(A^TA)^{-1}$ is a 3×3 matrix for the Yeoh model, and taking its inverse is relatively easier than other models, while for the Polynomial form with 5 parameters this inversion is not feasible and other considerations are required. This is the main difficulty

of our inverse problem and is referred to as ill-conditioning of the system. For the Veronda-Westmann model this inversion is converted to requirement for solving the nonlinear system of equation that result from this model. Tackling the ill-conditioning and nonlinear optimization was the major challenge of solving the inverse problem.

4.1.9. Regularization Technique Used In the Study

In many applications of linear algebra, the need arises to find a good approximation $\hat{x}$ to a vector $x \in \mathbb{R}^n$ satisfying an approximate equation $Ax \approx y$ with ill-conditioned or singular $A \in \mathbb{R}^{m \times n}$ given y$\in \mathbb{R}^m$. The solution to this system is $\hat{x} = A^{-1}y$ (or in the full rank over determined case $A^{+}y$, where A^{+} is the pseudo inverse of A). If this solution exists at all, it is usually a meaningless bad approximation to x due to the ill-conditioning of the matrix A. The reason for this difficulty is the ill-conditioning of the matrix $(A^T A)$. There are three conditions in which a matrix becomes ill-conditioned:

- If the determinant of the coefficient matrix is too small
- If a row/column of the coefficient matrix is close to a linear combination of other rows/columns of the matrix
- If the ratio of the largest eigen-value of the coefficient matrix to the smallest one is too large.

All of these cases have similar effects on the system response, and make it unstable. Round off errors in the computations can potentially result in very inaccurate solutions in ill-conditioned systems. We have observed that the system of equations for the polynomial form is ill-conditioned. Solutions to this ill-conditioned problem may be found using regularization techniques.

Three different regularization techniques were used here to solve the ill-conditioning problem of the system. There three methods are:

- Truncated SVD
- Tikhonov Regularization
- Wiener Filtering

Each regularization technique leads to a certain amount of error in the reconstructed parameters. The methods that have large errors in final result are more stable for large errors in initial iterations while the methods with high accuracy in finding the parameters are usually unstable for large errors in initial iterations. Truncated SVD, Tikhonov regularization and Wiener filtering technique are given in equations (4-17), (4-18) and (4-19) respectively.

$$Ax = b, \qquad A^T A = U\Sigma V^T,$$
$$\hat{x} = \sum_{i=1}^{q} \frac{u_i^T b}{\sigma_i} v_i, \qquad q < rank(A^T A), \tag{4-17}$$

$$\hat{x} = \left(A^T A + \Gamma^T \Gamma\right)^{-1} + A^T b \tag{4-18}$$

$$\hat{x} = \sum_{i=1}^{q} f_i \frac{u_i^T b}{\sigma_i} v_i, \qquad q = rank(A^T A),\ f_i = \frac{\sigma_i^2}{\sigma_i^2 + \alpha^2} \tag{4-19}$$

4.1.10. Applying the sequential regularization technique to the algorithm

This section reports the method of applying the reconstruction algorithm in conjunction with the Polynomial strain energy function to reconstruct the corresponding tissues' hyperelastic parameters. This technique is being introduced here for the first time. The algorithm is developed in our lab and takes advantage of the iterative nature of our

system. Iterative techniques are unstable at the early stages and become more stable as the process reaches its final iterations. This technique is designed in a way that it takes profit out of this behavior of the iterative processes and provided promising results for ill-conditioned systems that are being solved iteratively.

A sequence of the three different regularization techniques described above is used here to solve the ill-conditioning problem of the system. Each regularization technique leads to a certain amount of error in the reconstructed parameters. Methods known to lead to large errors are more stable during the initial iterations of the algorithm where errors are expected to be large while methods known to be highly accurate in finding the parameters are usually unstable during the initial iterations. Therefore, the Truncated SVD (singular value decomposition) was used for the first set of iterations where the error is large. This method is very stable and leads the iterations to the vicinity of the exact value of parameters but is not capable of finding the exact solution. Following this first set of iterations, we switched to Tikhonov regularization technique with $\Gamma = \alpha I$ after the Truncated SVD converged. Tikhonov regularization is known to provide better solutions than the Truncated SVD. Although the output of Tikhonov regularization is close to the exact values, its accuracy is not sufficient for our problem. Therefore, a third regularization technique was used to achieve more accurate results. Wiener Filtering was used for this purpose. Wiener Filter is similar to Tikhonov Regularization but instead of modifying all the eigenvalues of the system, it only changes the smallest one. Thus the main system of equations does not change significantly as a result of this regularization. This sequential regularization technique led reasonably accurate hyperelastic parameter reconstruction.

4.1.11. Using Optimization for Veronda-Westmann model

In the case of Veronda-Westmann model, unlike other models; the inverse problem boils down to a non-linear system of equations. Thus in order to update the parameters, it is required to solve the non-linear system given in equation (4-20):

$$\{\sigma\} = f(\{C\}) \qquad 4\text{-}20$$

Where $\{\sigma\}$ is the element stress tensor, $f(\cdot)$ is a function of nodal displacements, and $\{C\}$ is the unknown hyperelastic parameters. This non-linear system of equations is solved using a non-linear least squares method that involves iteratively using a combination of preconditioned conjugate gradient optimization method, steepest descent method and the Newton's optimization method that are described in the Theory chapter of this thesis.

5. Results

In this chapter we will discuss the results of applying the reconstruction algorithm introduced in the methods chapter to our phantoms in order to validate the proposed method. To test the feasibility and accuracy of the method in terms of reconstructing the hyperelastic parameters of tumor tissue, we performed numerical and experimental studies that involved numerical and breast tissue mimicking phantoms. In the first study, a numerical phantom with simplified breast geometry was developed. This model comprised of a cylinder connected to a hemisphere. We applied the algorithm to this model in conjunction with various strain energy functions and reported the corresponding reconstruction results in this chapter.

For the tissue mimicking phantom, we constructed a phantom with cubic shape using PVA (Polyvinyl Alcohol). Again, we applied the algorithm in conjunction with various strain energy functions to this phantom and reported the corresponding results. In this study, we simplified the actual 3-D problem to a 2-D model to speed up the analysis. As discussed in the Methods, the 2-D model used here was developed using plane stress idealization. The phantom was made such that it satisfied this assumption with relatively high accuracy.

5.1. Numerical Validation

In the first stage, a numerical phantom study was performed on a simplified breast tissue geometry comprised of a hemisphere connected to a cylinder. The phantom is comprised of three different tissue types to represent the two different tissue types in a normal breast (fat and fibroglandular tissues) in addition to a tumor tissue as shown in Figure 5-1. The

phantom's FE mesh was constructed using a transfinite interpolation meshing technique. This mesh with element sets corresponding to three tissue types is shown in Figure 5-1.

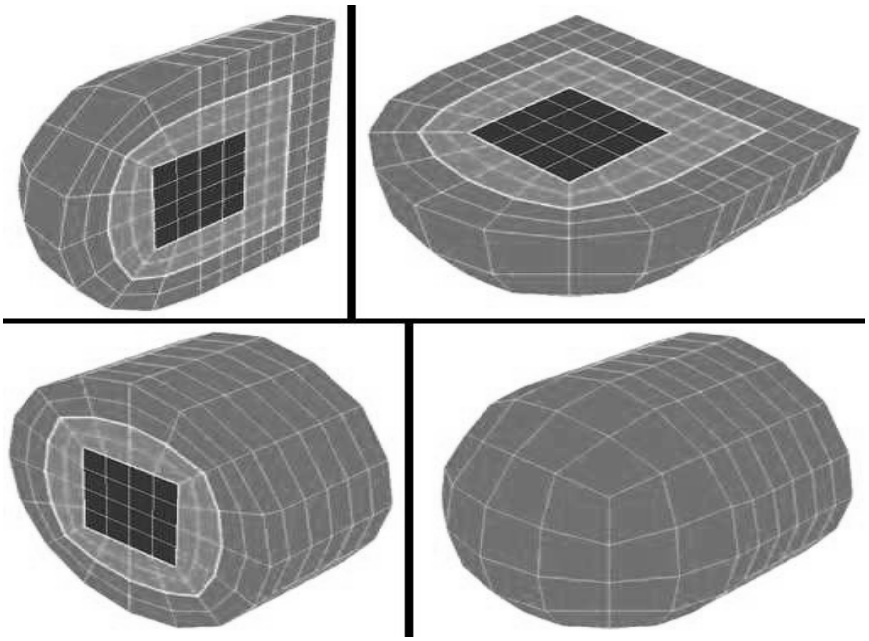

Figure 5-1. FE mesh of the computational breast phantom and three corresponding orthogonal cross sections. Different tissue types are shown in different grayscale colors, where the interior, middle and exterior layers represent tumor, fibroglandular and adipose tissues, respectively.

As described earlier, the phantom's tissue deformation was simulated using ABAQUS based on prescribed displacement boundary conditions. The hyperelastic parameters reconstruction was conducted using the iterative technique summarized in the flowchart shown in Figure 4-11.

5.1.1. Geometry

Using prescribed boundary conditions, simulated tissue displacements were obtained using a nonlinear FE model developed in ABAQUS. The phantom's FE mesh was constructed using transfinite interpolation (TFI) meshing technique [55]. To compensate for the weakness of the transfinite interpolation in meshing circular geometries we used the method given in [56]. This method constructs a circular mesh by applying the TFI method described in Appendix A to five rectangular meshes that are connected to each other as shown in Figure 5-2.

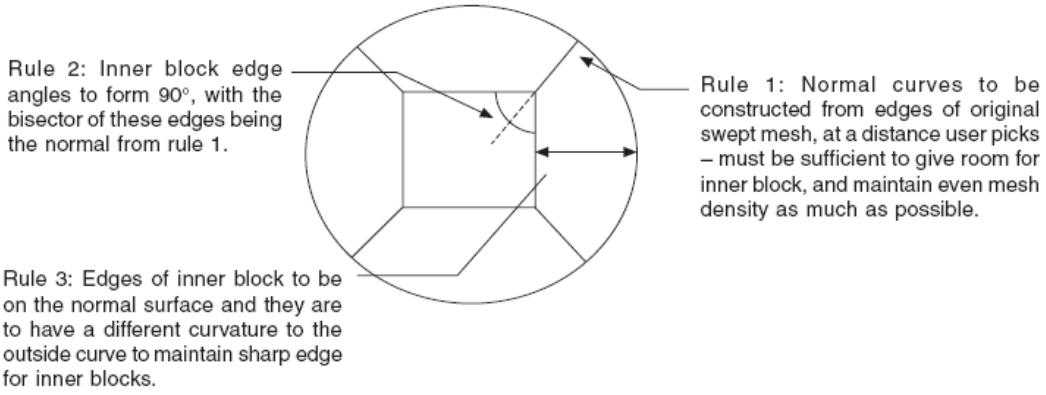

Figure 5-2. The meshing technique used to eliminate distorted elements that occur while using transfinite interpolation method of mesh generation.

Figure 5-3 compares the mesh generated using transfinite interpolation with the mesh generated by Horgan *et al* [56]. As can be seen in this figure, the meshing technique used by Horgan led to significantly better quality FE mesh compared to the TFI mesh.

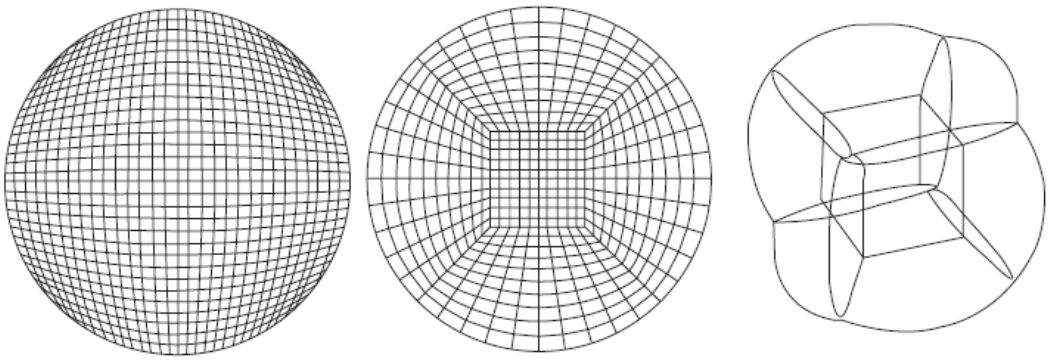

(a) (b) (c)

Figure 5-3. Transfinite interpolation meshing method a) simple implementation, which leads to low quality FE mesh causing numerical issues, b) FE mesh generated using the new? method, which high quality with no extensively distorted elements, and c) extension of the new meshing technique to 3-D.

The advantage of using this method over using the conventional transfinite interpolation is that the latter results in extremely distorted elements close to the circle perimeter, while the former avoids having such elements leading to a very smooth and uniform FE mesh. The mesh generated for this model and its three different cross-sections are shown in Figure 5-1.

5.1.2. Numerical analysis

30% compression was applied to the numerical phantom using the nonlinear ABAQUS model. Once the phantom model is deformed numerically, the displacement data provided by the software was obtained. The analysis was performed for three different commonly used strain energy functions, the Yeoh, the Polynomial and the Veronda-Westmann strain energy functions. Given the tissue incompressibility assumption, these strain energy functions are independent of the third strain invariant. Amongst the three

strain energy functions used at this stage, the Polynomial and Veronda-Westmann models are dependent on both first and second strain invariants (I_1 and I_2) while the Yeoh model is only dependent on the first strain invariant (I_1). As discussed before, there are several advantages in choosing strain energy function that are independent of the second strain invariant.

Once the model is developed in ABAQUS, the resulting displacement field is fed to the reconstruction algorithm to obtain the tissues' hyperelastic properties.

5.1.3. Inverse problem

In this parameter reconstruction problem, we use the displacement data acquired from the pre- and post-compression to determine the tissues' hyperelastic parameters ($C_{ij}{}'s$ in equation 4-15). As mentioned in the Methods chapter solving the resultant inverse problem is not always straight forward, since it requires calculation of matrix inverse which is not always possible. Thus, regularization techniques are required in most applications. In this problem regularization was required to construct the hyperelastic parameters corresponding to the Polynomial strain energy function.

5.1.4. Simulation results

The displacement data for each node was used to form the coefficients matrix and the system of equations was solved for Yeoh, Polynomial and Veronda-Westmann models. The inverse problem was solved using the iterative algorithm depicted in Figure 4-11. For the Polynomial form regularization techniques were required to achieve convergence while the Yeoh and Veronda-Westman models converged without any regularization.

5.1.5. Reconstruction results for Polynomial Model using sequential regularization

This section reports the results of applying the reconstruction algorithm in conjunction with the Polynomial strain energy function to reconstruct the corresponding tissues' hyperelastic parameters. In this section we assume that the hyperelastic parameters of the normal breast tissues (the adipose and the fibroglandular tissues) are known, and we seek to determine the tumor's hyperelastic parameters. The regularization technique is applied to the system as described in the Theory chapter. This technique is developed for this research for the first time and showed promising results in tackling the ill-conditioning problem of our iterative process.

The least squares error of the system in each iteration is shown in Figure 5-4. In this regularization technique, we divided the iterations range into three regions as shown in the Figure The dashed lines correspond to the first region where the Truncated SVD method was used. The dotted portion of the graph corresponds to the second region where the Tikhonov Regularization technique was used while the last portion of the graph corresponds to the Wiener Filtering regularization technique used for the third iteration region

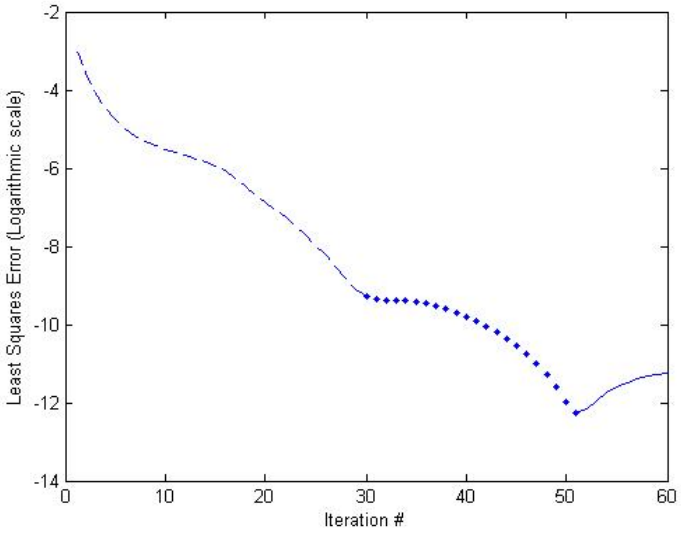

Figure 5-4. Least squares error of the system at each iteration. The dashed line corresponds to the Truncated SVD method. The dotted and solid lines correspond to the Tikhonov Regularization technique and the Wiener Filtering regularization technique, respectively.

Figure 5-5 shows the actual value for each parameter versus its reconstructed value at every iteration for Polynomial model.

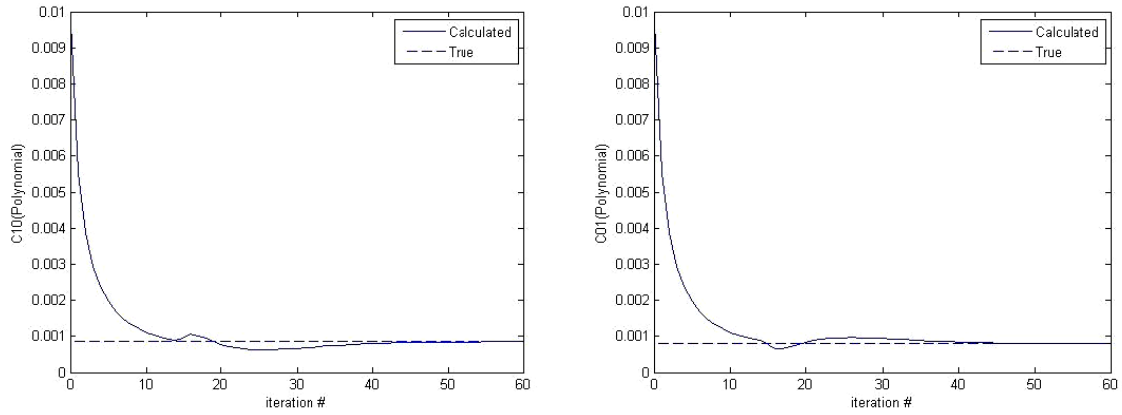

(a) (b)

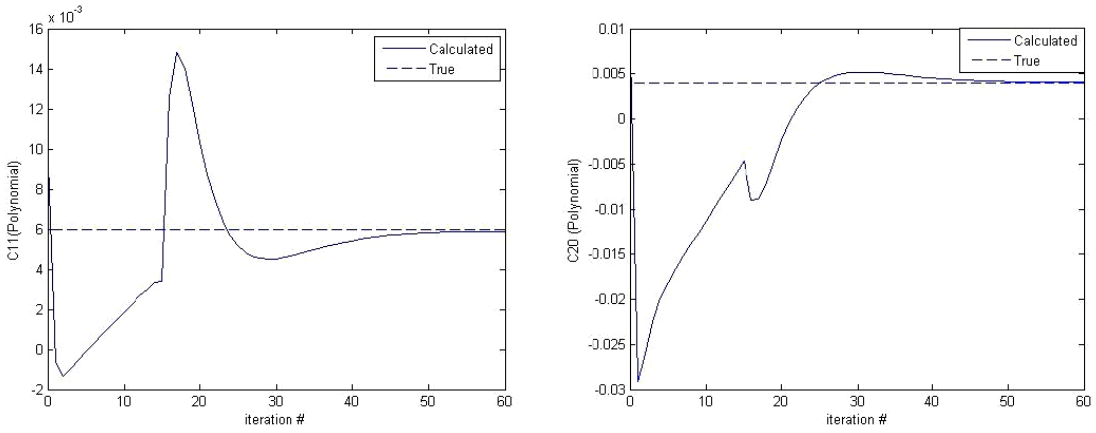

(c)

(d)

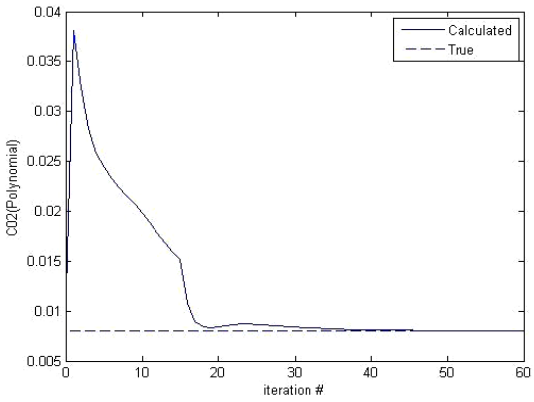

(e)

Figure 5-5 a, b, c, d, e) the convergence of C10, C01, C11, C20, and C02 in the Polynomial form, respectively.

The stress-strain relationship corresponding to the actual parameters versus the reconstructed parameters for Polynomial model is shown in Figure 5-6.

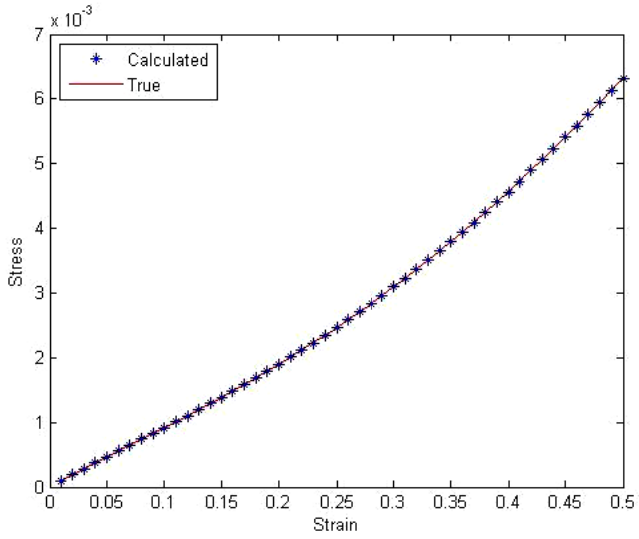

Figure 5-6. True and reconstructed stress-strain curves of the tumor tissue of the Polynomial form

Figure 5-7 shows the stress-strain relationship for fat, fibroglandular and tumor tissues used in the analysis for the Polynomial model.

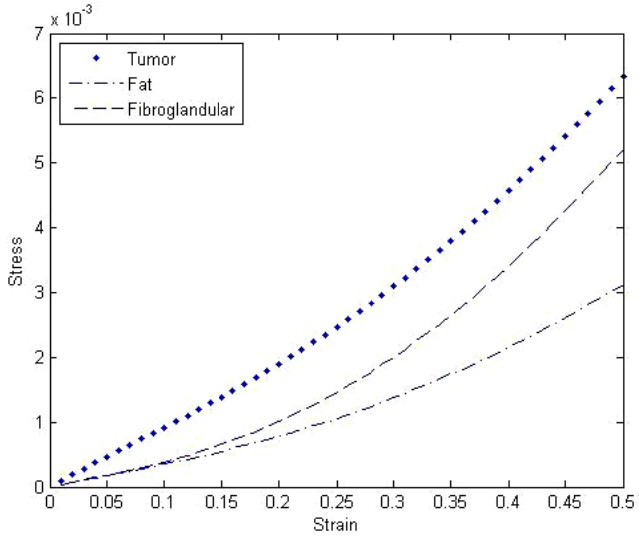

Figure 5-7. True stress-strain relationship of the fat, fibroglandular and tumor tissues of the Polynomial form

Table 5-1 illustrates the initial guess, true parameter values, calculated parameter values, number of iterations required for convergence, the tolerance used in the convergence criteria, and the percentage error of the calculated values.

Table 5-1. The initial guess, true values of the hyperelastic parameters, calculated values of the parameters, number of iteration required to reach these values, the tolerances used as convergence criteria and the error percentage of the calculated values for Polynomial model.

	Initial Guess(kpa)	True Value(kpa)	Calculated Value (kpa)	Iteration Number	Tolerance (tol %)	Error (%)
C10 (Polynomial)	0.01	0.00085	0.000849	60	0.04	0.038
C01 (Polynomial)	0.01	0.0008	0.000799	60	0.04	0.016
C20 (Polynomial)	0.01	0.004	0.004065	60	0.04	1.630
C11 (Polynomial)	0.01	0.006	0.005883	60	0.04	1.950
C02(Polynomial)	0.01	0.008	0.008051	60	0.04	0.648

5.1.6. Reconstruction results for Yeoh Model

This section reports the results of applying the reconstruction algorithm to the numerical model using the Yeoh strain energy function for modeling the hyperelastic behavior of the tissues. Similar to the Polynomial model, in this section we assume that the hyperelastic parameters for the normal breast tissues (the adipose and the fibroglandular tissues) are known, and we seek to determine the parameters for the tumor. Figure 5-8 shows the actual value for each parameter versus its reconstructed value at every iteration for the Yeoh model.

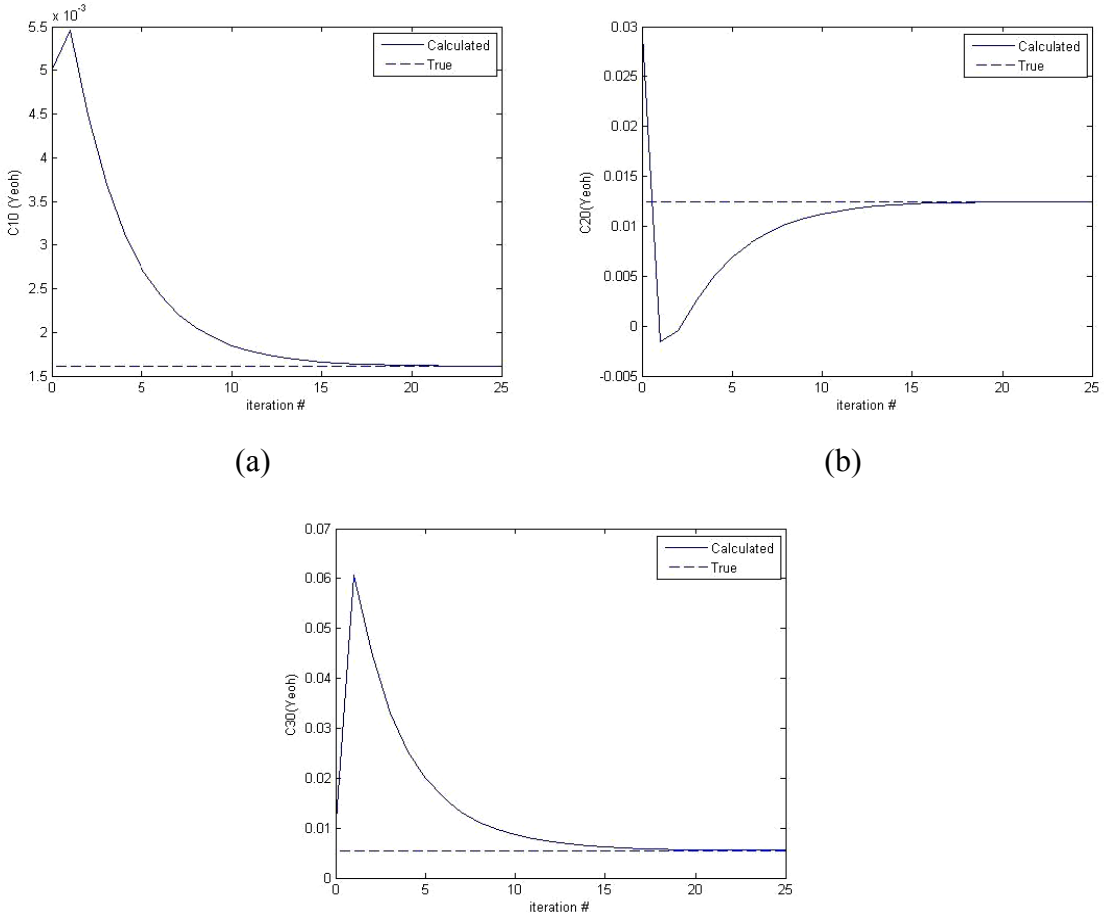

Figure 5-8 a, b, c) the convergence of C10, C20, and C30 in the Yeoh form, respectively.

The stress-strain relationship corresponding to the actual parameters versus the reconstructed parameters for Yeoh model is shown in Figure 5-9.

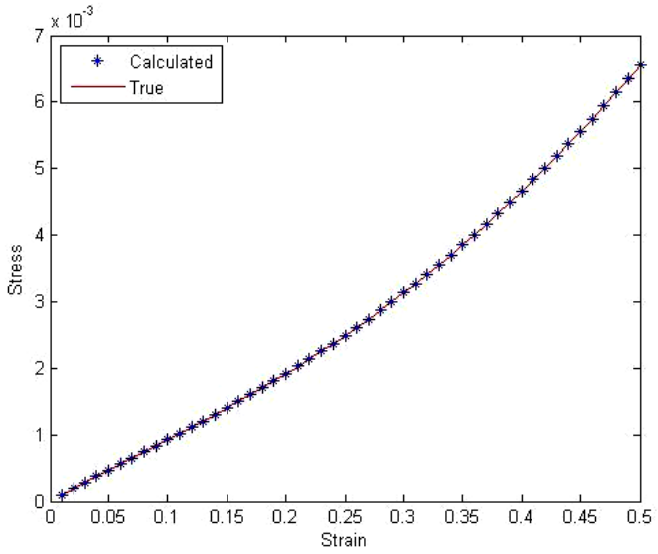

Figure 5-9. True and reconstructed stress-strain curves of the tumor tissue of the Yeoh form.

Figure 5-10 shows the stress-strain relationship for the fat, fibroglandular and tumor tissues used in the analysis for the Yeoh model.

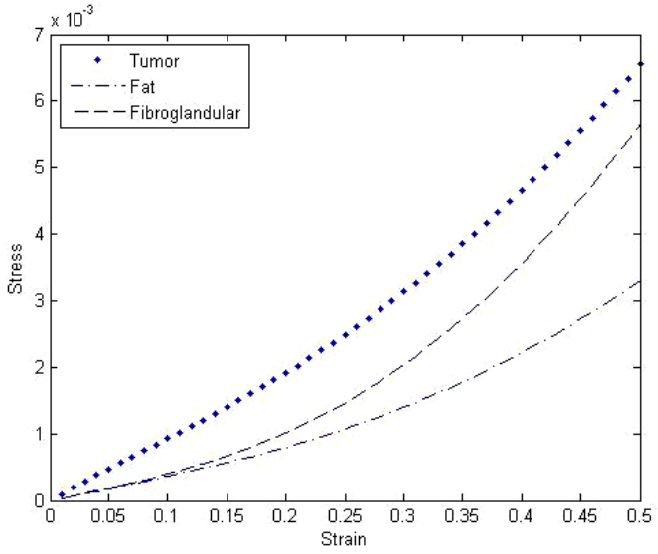

Figure 5-10. True stress-strain relationships of the fat, fibroglandular and tumor tissues of the Yeoh form.

Table 5-2 illustrates the initial guess, true parameter values, calculated parameter values, number of iterations required for convergence, the tolerance used in the convergence criteria, and the percentage error of the calculated values for Yeoh model.

Table 5-2. The initial guess, true values of the hyperelastic parameters, calculated values of the parameters, number of iteration required to reach these values, the tolerances used as convergence criteria and the error percentage of the calculated values for Yeoh model.

	Initial Guess(kpa)	True Value(kpa)	Calculated Value (kpa)	Iteration Number	Tolerance (tol %)	Error (%)
C10 (Yeoh)	0.005	0.00161	0.001612	25	0.2	0.143
C20 (Yeoh)	0.03	0.0125	0.012487	25	0.2	0.1
C30 (Yeoh)	0.01	0.00551	0.005541	25	0.2	0.563

5.1.7. Reconstruction results for Veronda-Westmann Model

This section reports the results of applying the reconstruction algorithm in conjunction with the Veronda-Westmann strain energy function for modeling the hyperelastic behavior of the tissues. Similar to the previously reported models, in this section we again assumed that the hyperelastic parameters of the normal breast tissues (the adipose and the fibroglandular tissues) are known, and we sought to determine the parameters for the tumor.

The reconstruction results corresponding to the 30% phantom compression were encouraging. The hyperelastic parameters for Veronda-Westmann model were reconstructed with high accuracy. Figure 5-11 shows the actual value for each parameter versus its reconstructed value at each iteration for the Veronda-Westmann model.

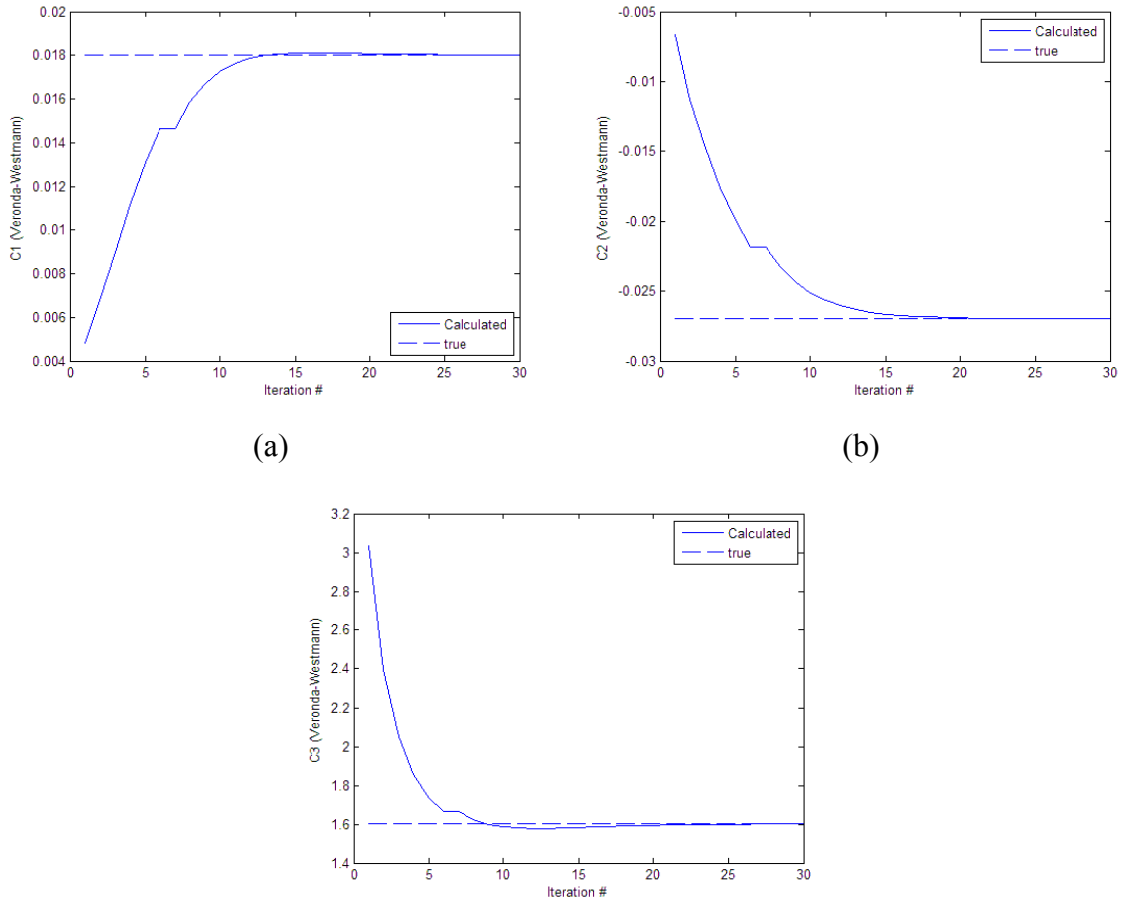

Figure 5-11 a, b, c) The convergence of C1, C2, and C3 in the Veronda-Westmann form, respectively.

The stress-strain relationship corresponding to the actual parameters versus the reconstructed parameters for the Veronda-Westmann model is shown in Figure 5-12.

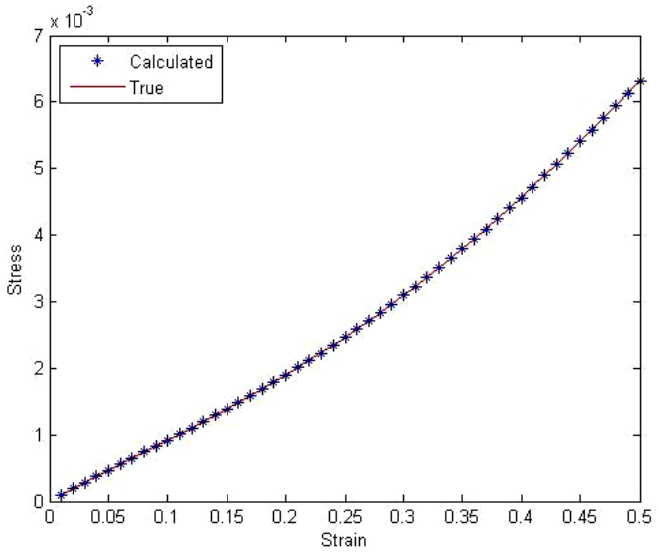

Figure 5-12. True and reconstructed stress-strain curves of the tumor tissue of the Veronda-Westmann hyperelastic model.

Figure 5-13 shows the stress-strain relationship for fat, fibroglandular and tumor tissues used in the analysis for the Veronda-Westmann model.

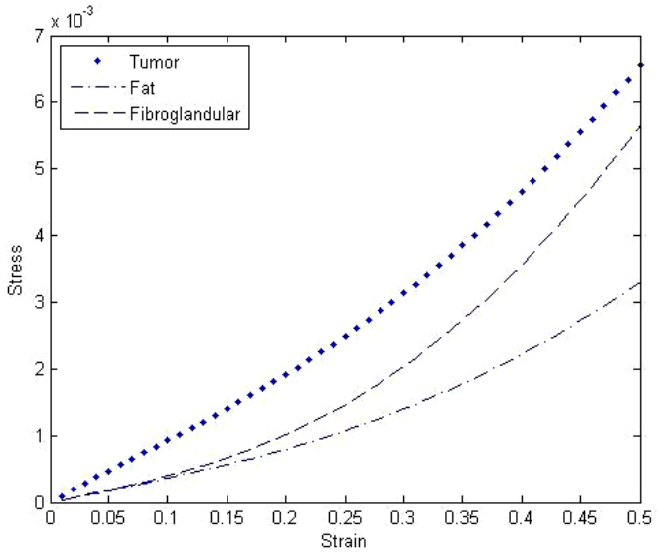

Figure 5-13. True stress-strain relationship of the fat, fibroglandular and tumor tissues of the Veronda-Westmann hyperelastic form.

Table 5-3 illustrates the initial guess, true parameter values, calculated parameter values, number of iterations required for convergence, the tolerance used in the convergence criteria, and the percentage error of the calculated values for the Veronda-Westmann model.

Table 5-3. The initial guess, true values of the hyperelastic parameters, calculated values of the parameters, number of iteration required to reach these values, the tolerances used as convergence criteria and the error percentage of the calculated values for Veronda-Westmann model.

	Initial Guess(kpa)	True Value(kpa)	Calculated Value (kpa)	Iteration Number	Tolerance (tol %)	Error (%)
C1 (VW)	0.01	0.0014	0.00139	15	0.1	0.71
C2 (VW)	0.01	-0.0048	-0.00479	15	0.1	0.21
C3 (VW)	20	5.0194	5.02	15	0.1	0.012

5.2. Experimental Phantom study

In this section the experimental phantom study that was performed to validate the reconstruction algorithm is presented. The phantom used here is a cubic phantom comprised of three different tissue types. The phantom is depicted in Figure 4-4. As shown in this figure, the phantom has three different sections representing the three different tissue types usually present in a cancerous breast. The phantom is constructed using PVA that is used extensively as tissue mimicking material since it exhibits mechanical behavior close to that of soft tissues. The specifications of the tissue material were given in the Methods Chapter. We also made the plane stress assumption to idealize the 3-D phantom into a 2-D model. This assumption and the amount of error it adds to the system was justified based on simulation assessments. The results of this analysis were presented in Methods Chapter. In addition to the PVA phantom that exhibits non-linear

mechanical behavior, we also performed investigation on a phantom made by Gelatin that exhibits linear mechanical behavior. The properties of this phantom was introduced in the methods chapter. Here, we first present the results of applying the reconstruction algorithm to the linear phantom, then we report the results of applying the reconstruction technique to obtain the hyperelastic parameters of the PVA phantom. We also report the results of uniaxial compression test performed on the cylindrical samples of each tissue type obtaining independent hyperelastic parameters measurement.

5.2.1. Linear phantom study

In order to experimentally validate the feasibility of the reconstruction algorithm in terms of calculating the mechanical properties of soft tissues, we first performed the reconstruction on a phantom made from Gelatin. Gelatin exhibits linear mechanical behavior. Hence, Hooke's law was used to measure the Young's Modulus of the tumor according to the following:

where is the stress tensor and is the strain tensor. Using this equation as the stress deformation relationship in the iterative reconstruction algorithm [57], we have the following iterative equation to update the Young's modulus of the tumor tissue.

Starting from an initial guess for E, we iteratively perform FE analysis to calculate the stress field followed by updating the E value according to the above equation until convergence is reached.

5.2.2. Uniaxial compression test for gelatin phantom

The mechanical properties (Young's modulus) of each tissue type are measured independently using the cylindrical sample of the same material. These measurements are required to assess the amount of error in the reconstruction results. The uniaxial test is performed using the electromechanical system developed by Samani *et al* [54]. Figure 5-14 shows the setup made for uniaxial compression test. This setup is made such that it applies uniform force to the top of the sample and records this applied force using a load cell. The displacement accuracy of this system is $2\mu m$. Thus, it is capable of recording the force and the amount of compression applied to the cylinder with high accuracy.

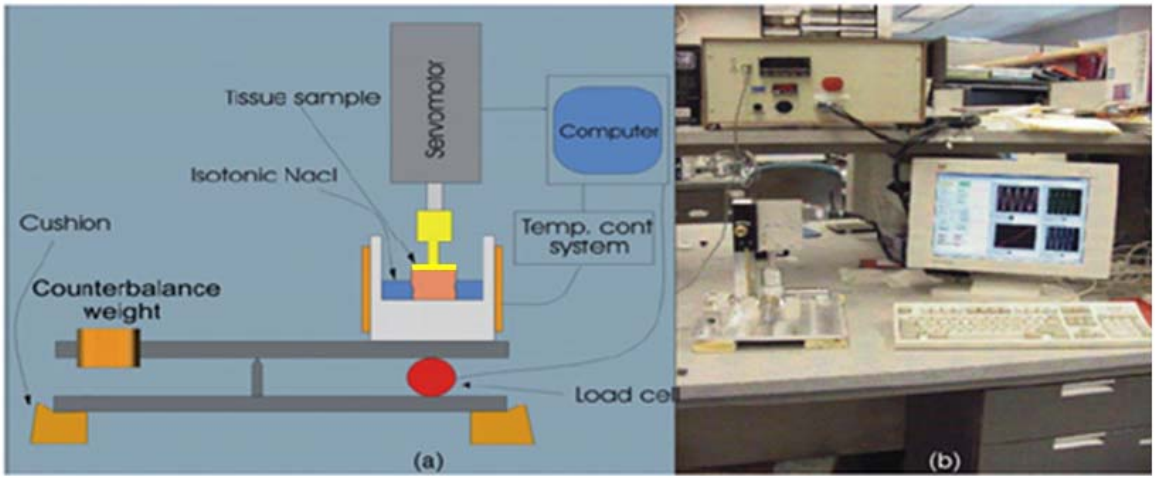

Figure 5-14 a) Schematic of uniaxial compression test setup, b) photograph of the uniaxial compression setup

The gelatin samples are shown in Figure 5-15 and have a height and diameter of approximately 2 $cm$and 1.25 cm, respectively.

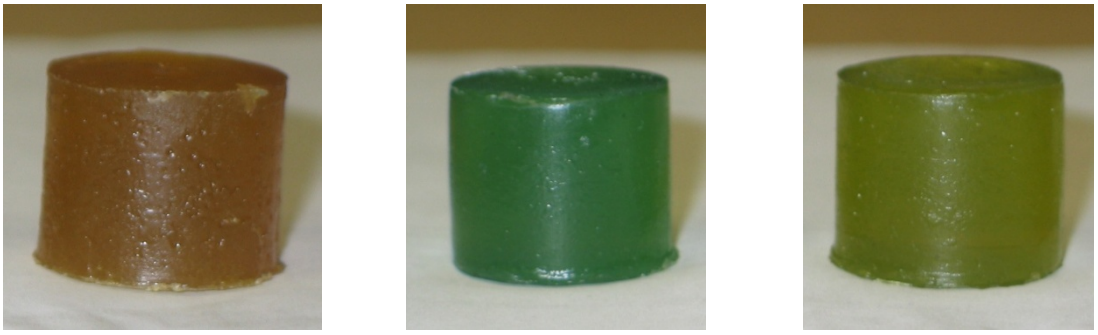

(a) (b) (c)

Figure 5-15 a, b and c) cylindrical samples of the tumor (inner brown cylindrical part of the phantom), fibloglandular tissue (middle dark green cubic part of the phantom) and the adipose (outer light green cubic part of the phantom), respectively. These sample were were made for uniaxial compression test of the gelatin phantom

The force deformation plots of the system for the three tissue samples are given in Figures 5-16, 5-17 and 5-18 for the brown, dark green and light green samples, respectively.

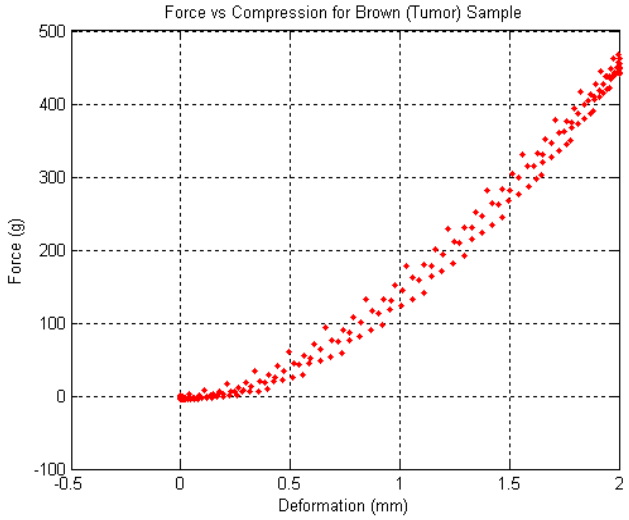

Figure 5-16. The force deformation plots of the brown (inner cylindrical portion of the phantom) sample.

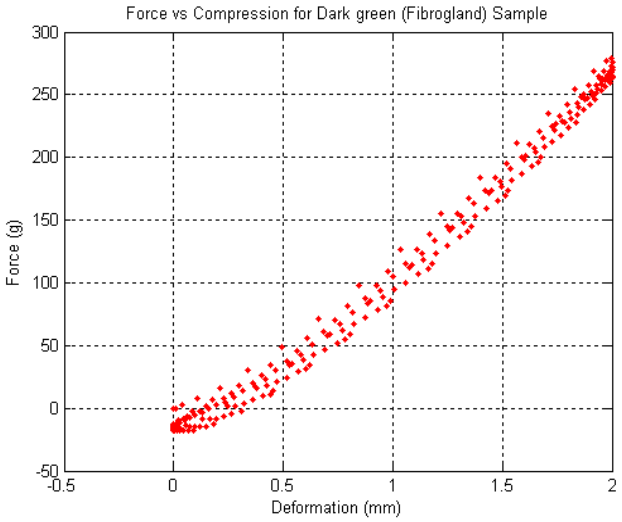

Figure 5-17. The force deformation plots of the dark green (middle cubic portion of the phantom) sample

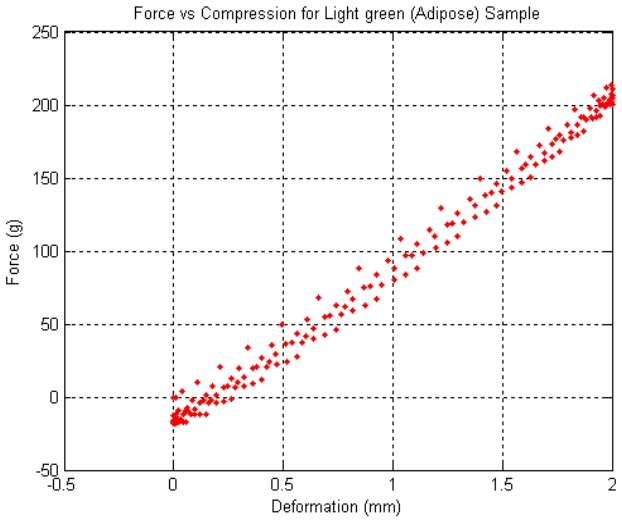

Figure 5-18. The force deformation plots of the light green (outer cubic portion of the phantom) sample

The Young's modulus of each tissue type calculated using the force deformation graphs are given in table 5-4.

Table 5-4. The Young's modulus of the brown (tumor), dark green (fibrogland) and light green (adipose) cylindrical samples calculated by uniaxial compression tests.

Tissue Type	Brown (tumor)	Dark green (fibrogland)	Light green (adipose)
Young's Modulus	**0.23 (MPa)**	**0.12 (MPa)**	**0.11 (MPa)**

5.2.3. Reconstruction results

In this section we report the reconstruction results for the gelatin phantom. Similar to the numerical analysis, we assume that the Young's moduli of the middle and outer tissues are known (in principle knowing E of one of the layers only is necessary) and the goal is to calculate that of the tumor. The displacement field was acquired manually (similar to the PVA phantom) by locating each node in the pre-compressed image and its corresponding node in the post-compressed image. The images are shown in Figure 5-19.

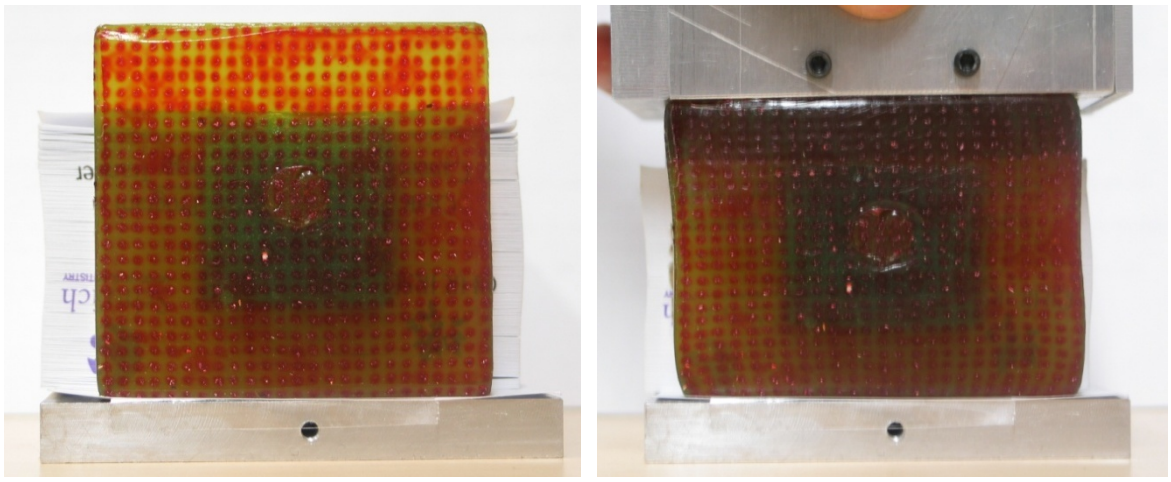

(a) (b)

Figure 5-19. Photo of the phantom a) before compression and b) phantom after compression.

compression was applied to the phantom. The convergence of the Young's modulus for tumor tissue is shown in Figure 5-20. As can be seen in this figure, the Young's modulus value converges in a few iterations. This shows the high speed of this method compared to optimization based methods.

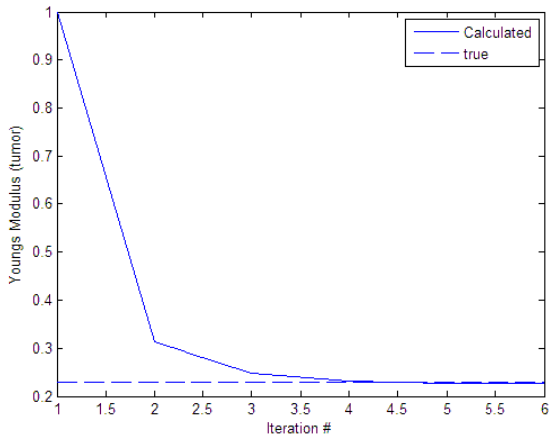

Figure 5-20. Convergence of the Young's modulus of the tumor tissue in the gelatin phantom

Table 5-5 illustrates the initial guess, true Young's modulus value, calculated Young's modulus value, number of iterations required for convergence, the tolerance used in the convergence criteria, and the percentage error of the calculated values.

Table 5-5. The initial guess, true value of the Young's modulus, calculated Young's modulus value, number of iteration required to reach this value, the tolerances used as convergence criteria and the error percentage of the calculated Young's modulus value.

Parameter	Initial Guess(MPa)	True Value(MPa)	Calculated Value (MPa)	Iteration Number	Tolerance (tol %)	Error (%)
Young's Modulus (tumor)	1	0.23	0.2261	6	0.69	1.72

As can be noticed in the Table 5-5, the reconstruction result for Young's modulus is highly accurate. These results demonstrate the sufficient accuracy of manual displacement tracking technique to be used for reconstruction. Thus this tracking technique can be used for the PVA phantom for which we will be reconstructing hyperelastic parameters of the tissues.

5.2.4. Hyperelastic phantom study

In this section the results of applying the reconstruction technique to the PVA phantom described before are presented. As mention before, the phantom has cubic shape and is comprised of three different tissue types with different mechanical properties. The two outer cubic parts represent breast normal tissues while the cylindrical portion in the center represents a breast tumor.

Similar to the linear case we use the plane stress assumption to simplify the 3-D reconstruction problem with a 2-D model. The phantom underwent 31.7% compression in this case; this high amount of compression is required here since we are seeking to determine the hyperelastic properties of the tissues, especially the tumor tissue, since it is stiffer and does not deform sufficiently with low compression. The phantom's baseline photo and a photo corresponding to its deformed state are depicted in Figure 4-9. To validate the results of the reconstruction, we first performed uniaxial compression tests on the cylindrical samples of each tissue type and measured their hyperelastic properties independently. Here, we first report the results of the uniaxial compression tests followed by presentation of the reconstruction process output.

5.2.5. Uniaxial compression test for PVA samples

To measure the hyperelastic properties of each tissue type independently, we constructed cylindrical samples from each PVA material. These samples have an equal height and diameter of approximately 1 cm as shown in Figure 5-21.

(a) (b) (c)

Figure 5-21. a, b and c) Cylindrical samples of the tumor(inner white cylindrical part of the phantom), fibloglandular tissue(middle blue cubic part of the phantom) and the adipose (outer yellow cubic part of the phantom), respectively. These samples were made for uniaxial compression tests of the PVA phantom layers.

Using the electromechanical setup described earlier, we acquired the force-deformation data for each sample. We applied $1g$ preload for the measurements and used the maximum compression range of the system which is $2.5mm$. The force-deformation plots of the three tissue samples are given in Figures 5-22, 5-23 and 5-24.

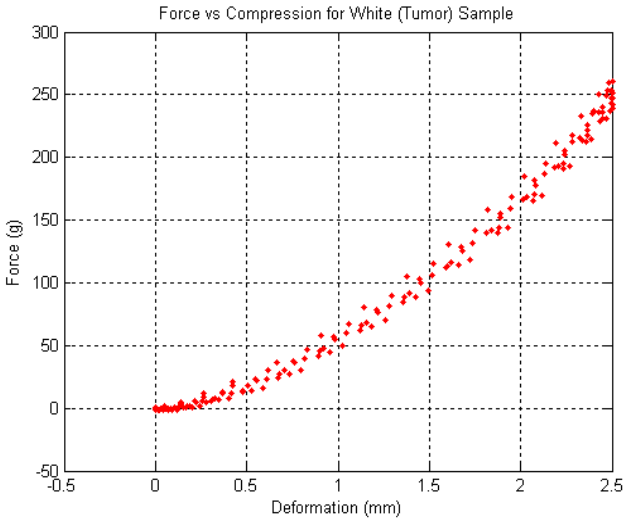

Figure 5-22. The force-deformation plots of the white (inner cylindrical portion of the phantom) sample.

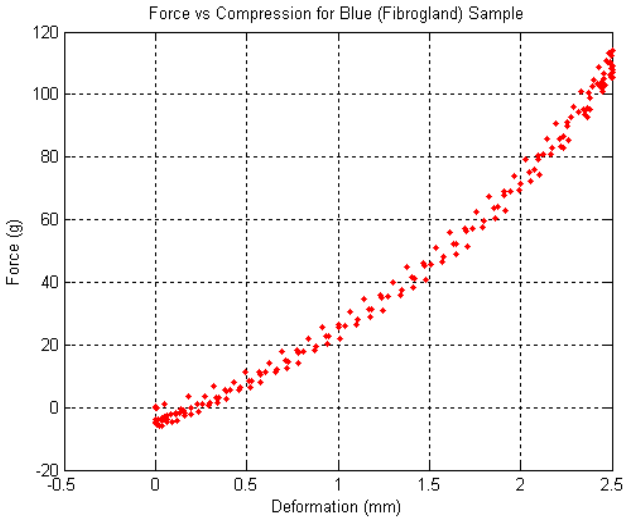

Figure 5-23. The force-deformation plots of the blue (middle cubic portion of the phantom) sample.

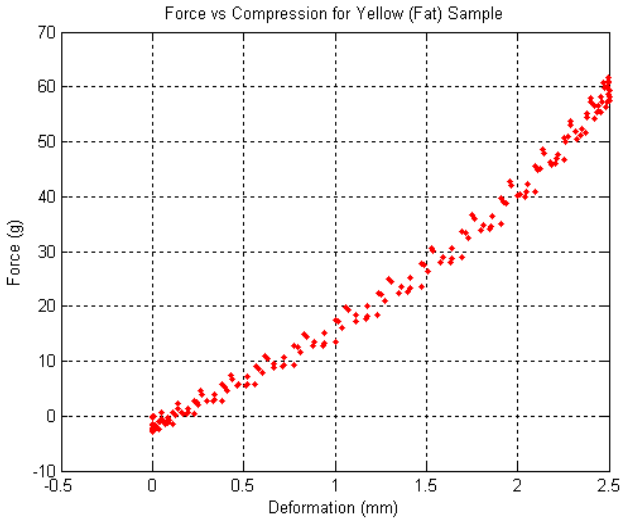

Figure 5-24. The force-deformation plots the yellow (outer cubic portion of the phantom) sample.

The hyperelastic parameters of each tissue type calculated using the force-deformation graphs for the Polynomial, Yeoh and Veronda-Westmann models are given in Tables 5-6, 5-7 and 5-8, respectively.

Table 5-6. The hyperelastic parameters of the white (tumor), blue (fibrogland) and yellow (adipose) cylindrical sample for Polynomial strain energy functions.

Coefficients	C10	C01	C20	C11	C02
White(Tumor)	0.0349	0.0123	0.1301	-0.1806	0.0969
Blue(Fibrogland)	0.0117	0.006	0.044	-0.0649	0.033
Yellow(Adipose)	0.0098	0.0032	0.0118	-0.0168	0.0087

Table 5-7. The hyperelastic parameters of the white (tumor), blue (fibrogland) and yellow (adipose) cylindrical sample for Yeoh strain energy functions.

Coefficients	C10	C20	C30
White(Tumor)	0.0206	0.0062	0.0448
Blue(Fibrogland)	0.0079	0.0029	0.023
Yellow(Adipose)	0.0046	0.0013	0.0054

Table 5-8. The hyperelastic parameters of the white (tumor), blue (fibrogland) and yellow (adipose) cylindrical sample for Veronda-Westmann strain energy functions

Coefficients	C1	C2	C3
White(Tumor)	0.0091	-0.0017	2.5875
Blue(Fibrogland)	0.0066	-0.003	2.0039
Yellow(Adipose)	0.0043	-0.0006	1.5564

The stress-strain curves corresponding to these sets of parameters for the three tissue types are given in Figure 5-25.

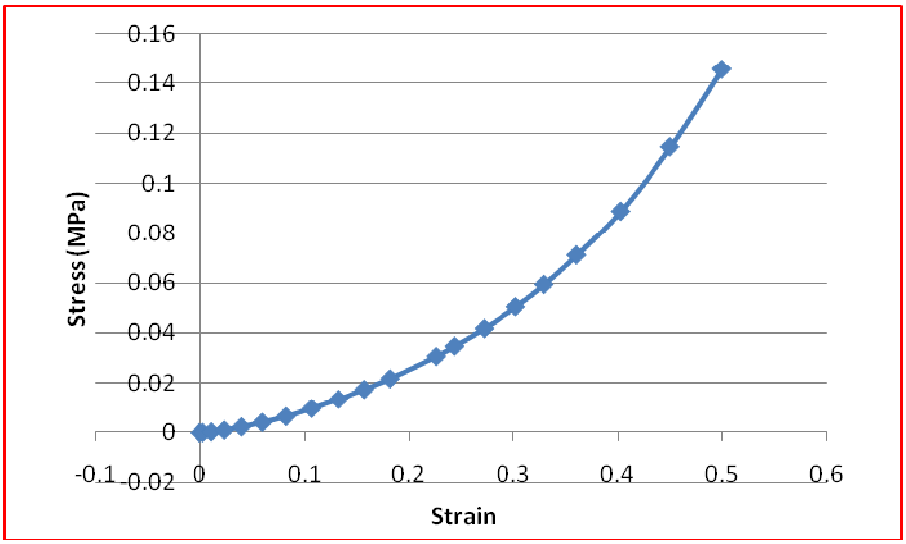

(a)

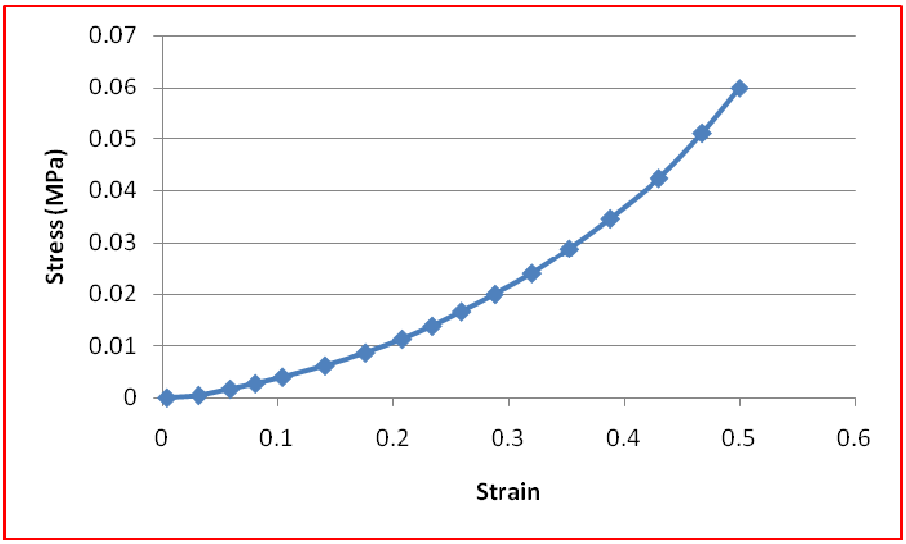

(b)

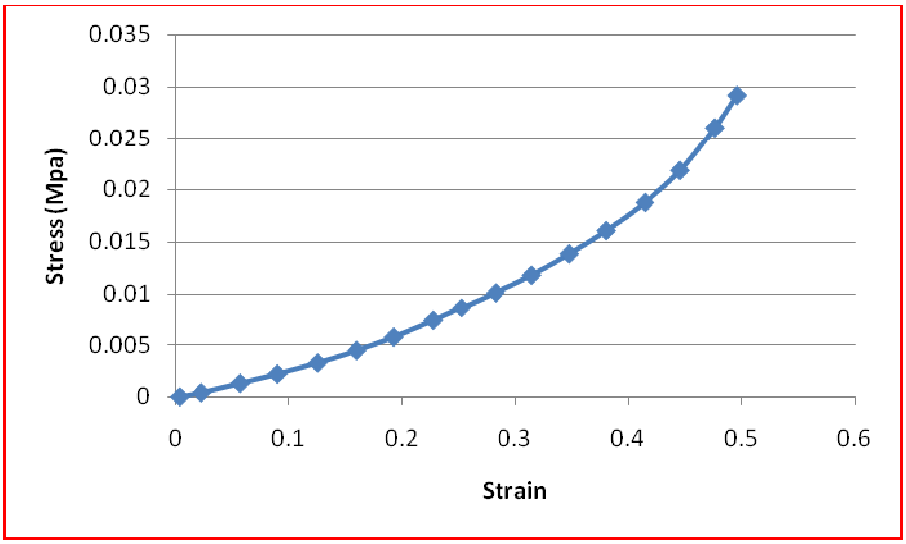

(c)

Figure 5-25. Stress-strain curves corresponding to calculated sets of hyperelastic parameters for a) white(tumor) tissue sample, b) blue (fibrogland) tissue sample, and c) yellow (adipose) tissue samples.

5.2.6. Absolute reconstruction results for the Polynomial model

In this section we report the results of applying the reconstruction algorithm to the pre- and post- compression images of the phantom while using the polynomial strain energy function to model the hyperelastic behavior of the soft tissues. The convergence of the

hyperelastic parameters to their final value are shown for all 5 parameters of the Polynomial form in Figure 5-26.

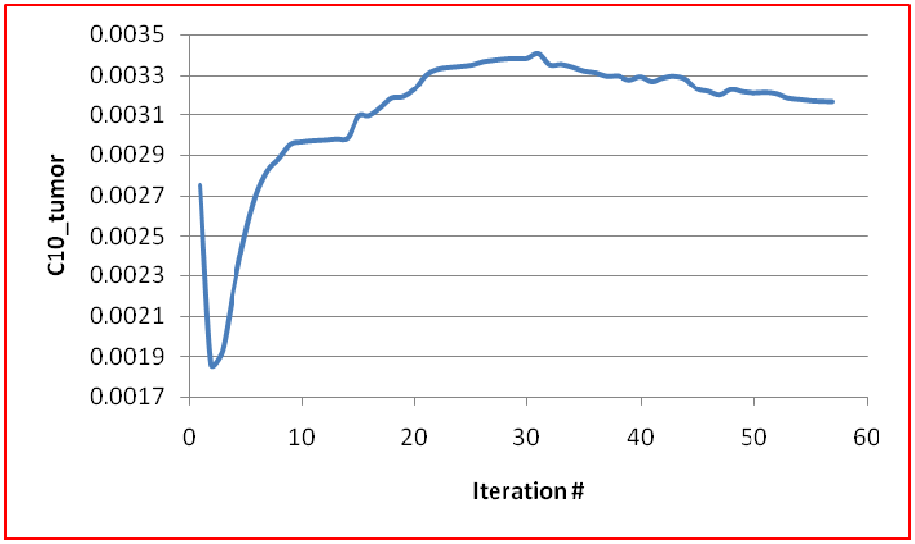

(a)

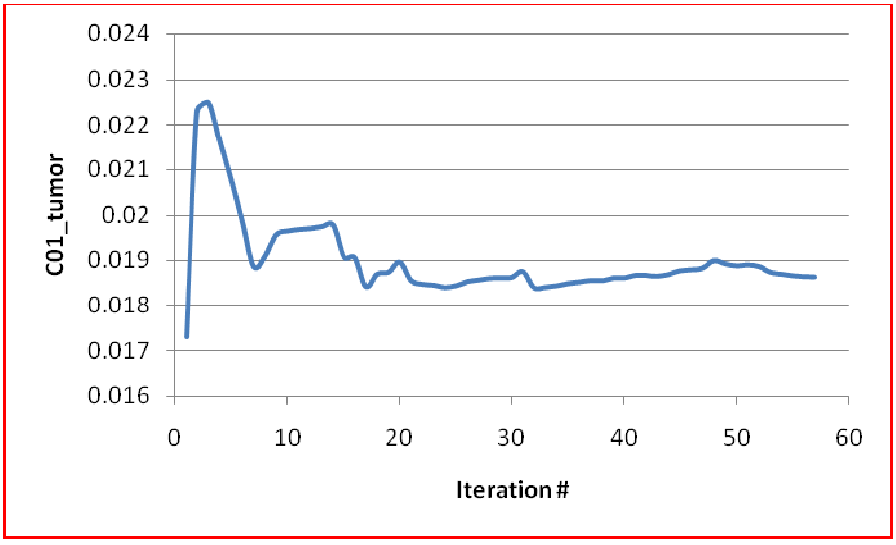

(b)

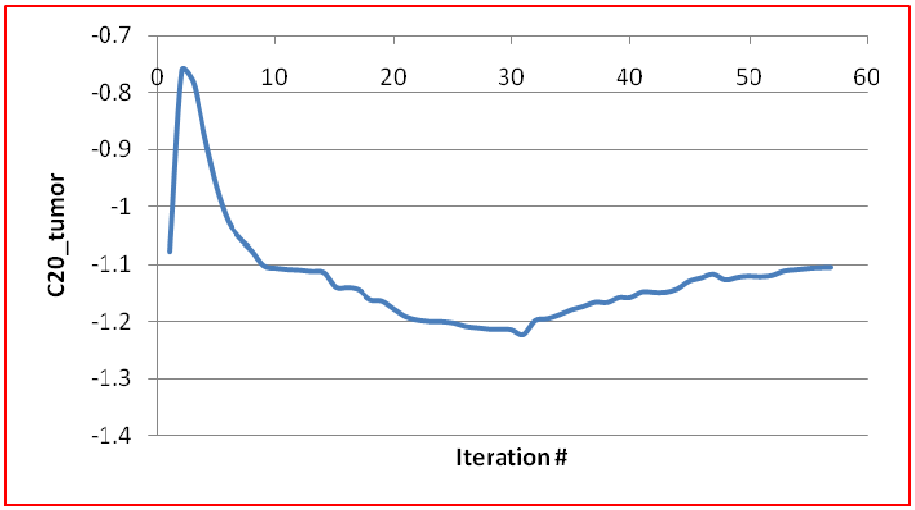

(c)

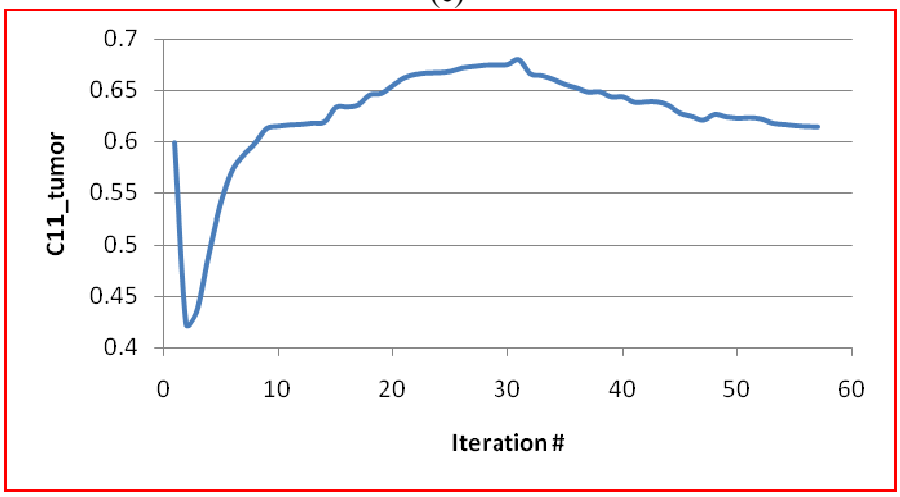

(d)

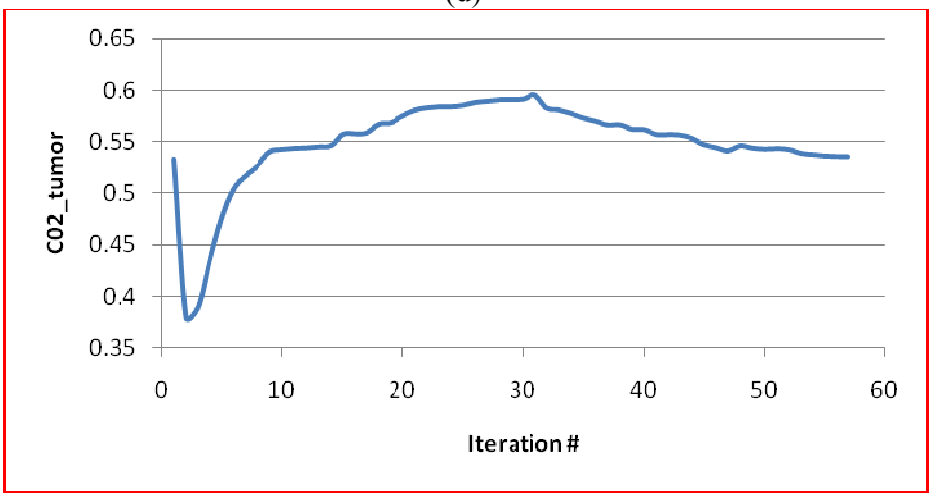

(e)

Figure 5-26. a, b, c, d, e) Convergence of C10, C01, C11, C20, and C02 in the Polynomial form, respectively.

In this case, similar to the numerical analysis, we used the proposed regularization technique to achieve convergence to avoiding the effects of ill-conditioning. The regularization technique involves applying the truncated SVD method to the first 15 iterations and then switches to the Tikhonov regularization for the next 20 iterations. The final 22 iterations are performed using the Wiener filtering technique to achieve better convergence. As can be derived from the convergence graphs after 15 iterations the truncated SVD method has converged, after achieving this convergence we switched to Tikhonov regularization. The stress-strain relationship corresponding to the actual parameters versus the reconstructed parameters for Polynomial model is shown in Figure 5-27.

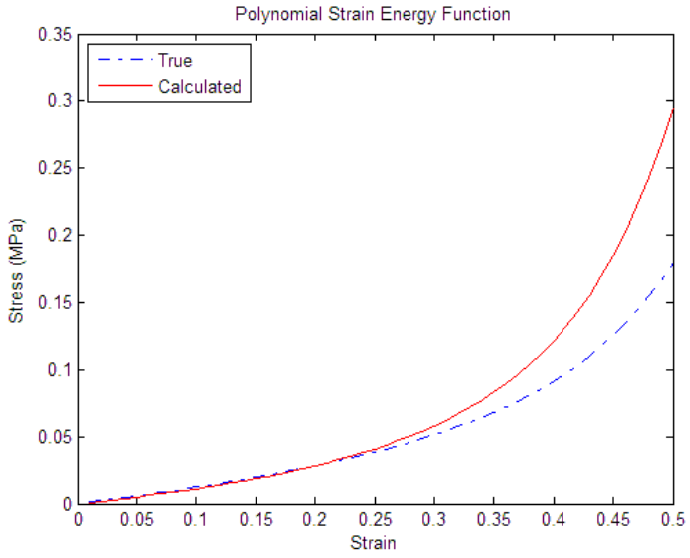

Figure 5-27. True and reconstructed stress-strain curves of the tumor tissue of the Polynomial hyperelastic model

Figure 5-27 shows, although the parameters are reconstructed with large errors, the stress-strain curves of the actual parameters versus the reconstructed parameters are very

close to each other. This is due to the fact that the cost function of our inverse problem is formulated in a way that it minimizes the difference between the experimental and calculated stress versus strain relationship in a least squares manner. Therefore, the agreement between the experimental and calculated stress-strain curves was better than the parameters agreement in this model. This agreement is even higher in the beginning of the curves where the tissue is still in the linear portion of is mechanical behavior.

Figure 5-28 shows the stress-strain relationship corresponding to the inner cylindrical part, middle cubic part and outer cubic portion of the phantom used in the analysis for the Polynomial model.

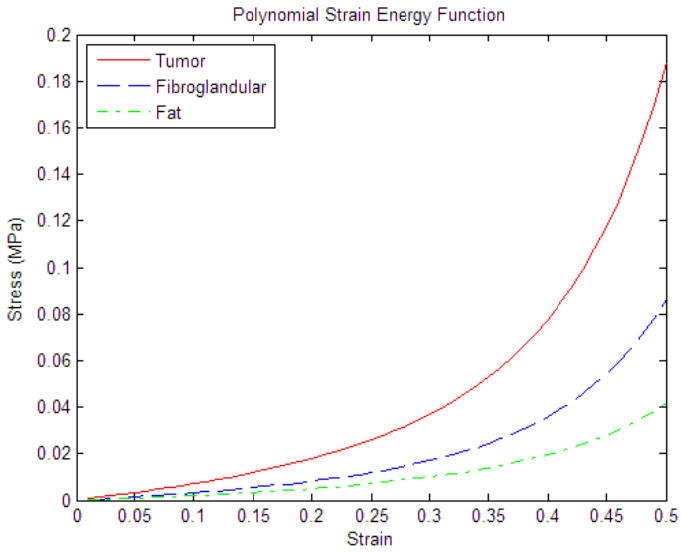

Figure 5-28. True stress-strain relationship of the fat, fibroglandular and tumor tissues of the Polynomial hyperelastic form.

Table 5-9 illustrates the initial guess, true parameter values, calculated parameter values, number of iterations required for convergence, the tolerance used in the convergence criteria, and the percentage error of the calculated values for the Polynomial model.

Table 5-9 The initial guess, true values of the hyperelastic parameters, calculated values of the parameters, number of iteration required to reach these values, the tolerances used as convergence criteria and the error percentage of the calculated values for Polynomial model.

	Initial Guess(kpa)	True Value(kpa)	Calculated Value (kpa)	Iteration Number	Tolerance (tol %)	Error (%)
C10 (Polynomial)	0.005	0.0239	0.003165	57	0.05	86.757
C01 (Polynomial)	0.005	0.0023	0.01863	57	0.05	710
C20 (Polynomial)	0.4	0.2041	0.614	57	0.05	200.83
C11 (Polynomial)	-1.5	-0.3396	-1.1057	57	0.05	225.58
C02(Polynomial)	0.4	0.1669	0.5357	57	0.05	220.97

5.2.7. Absolute reconstruction results for the Yeoh model

In this section we report the results of applying the reconstruction algorithm to the pre- and post- compression images of the phantom while using the Yeoh strain energy function to model the hyperelastic behavior of the soft tissues. The convergence of the hyperelastic parameters to their final value are shown for all 3 parameters of the Yeoh form in Figure 5-29.

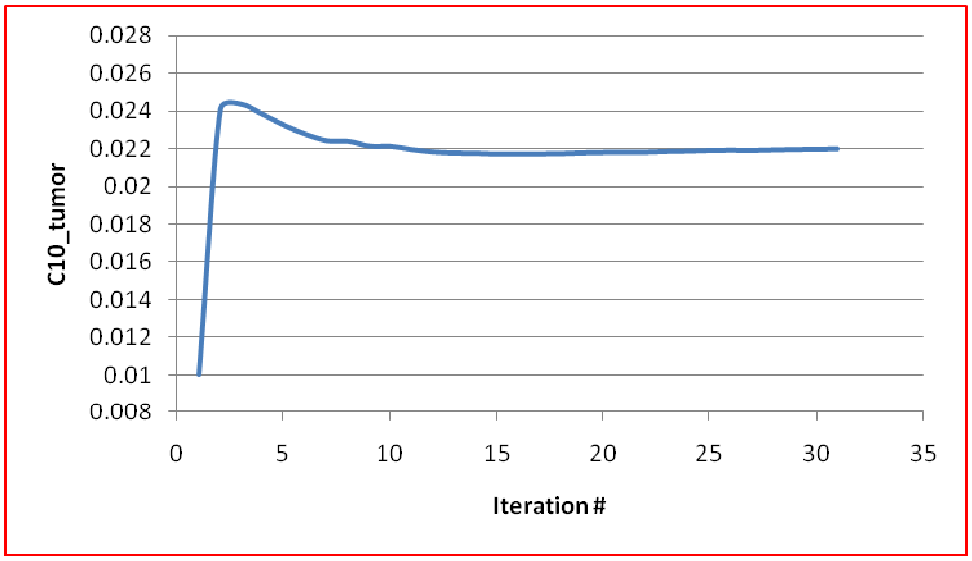
0.028
0.026
0.024
0.022
0.02
0.018
0.016
0.014
0.012
0.01
0.008
C10_tumor
0
5
10
15
20
25
30
35
Iteration #

(a)

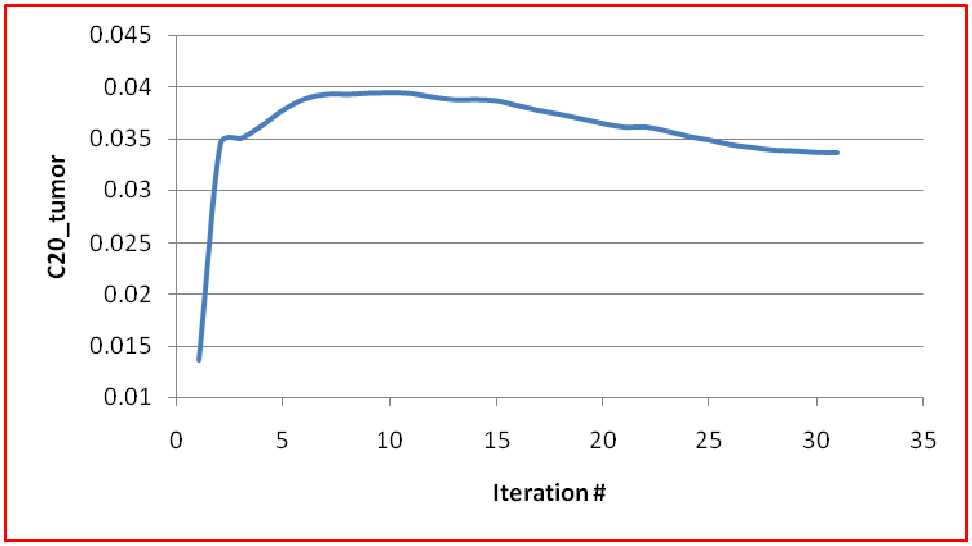
0.045
0.04
0.035
0.03
0.025
0.02
0.015
0.01
C20_tumor
0
5
10
15
20
25
30
35
Iteration #

(b)

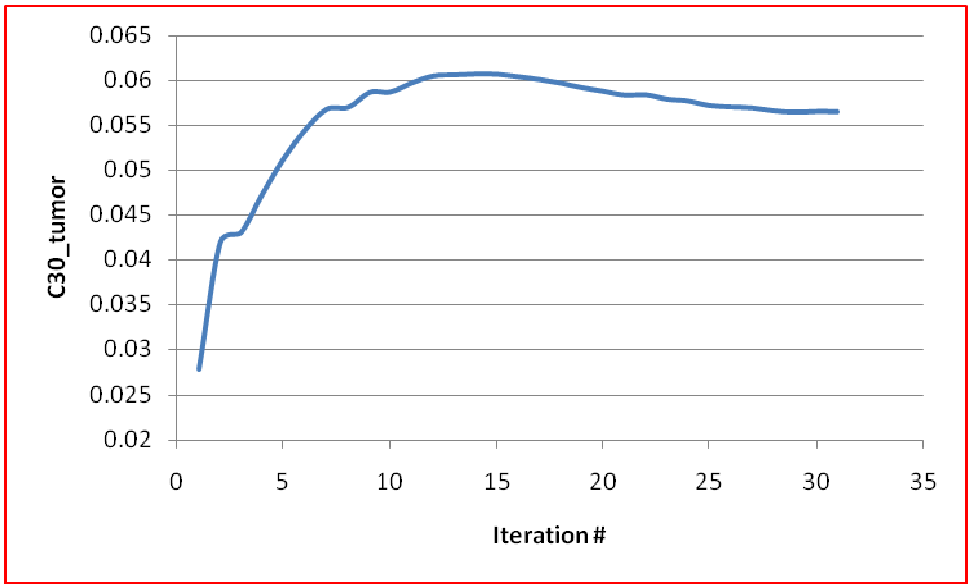

(c)

Figure 5-29. a, b, c) Convergence of C10, C20, and C30 in the Yeoh form, respectively.

The stress-strain relationship corresponding to the actual parameters versus the reconstructed parameters for Polynomial model is shown in Figure 5-30.

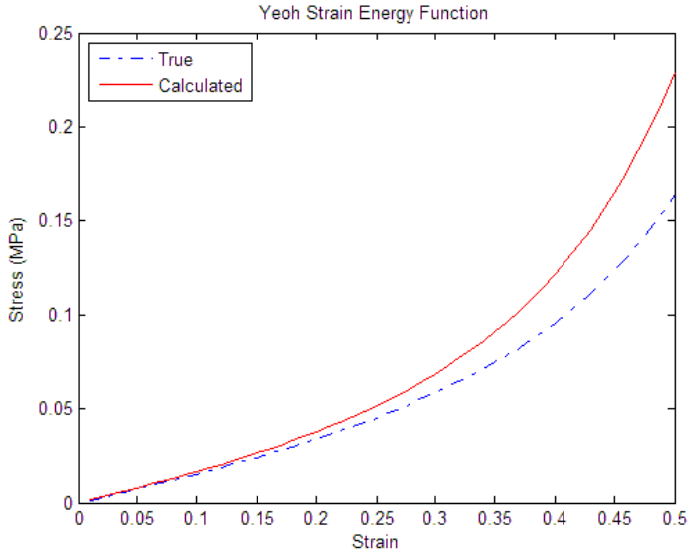

Figure 5-30. True and reconstructed stress-strain curves of the tumor tissue of the Yeoh hyperelastic model.

This figure again justifies the match between the reconstructed and true stress-strain curves for the Yeoh model as discussed for the Polynomial model previously.

Figure 5-31 shows the stress-strain relationship corresponding to the inner cylindrical part, middle cubic part and outer cubic portion of the phantom used in the analysis for the Yeoh model.

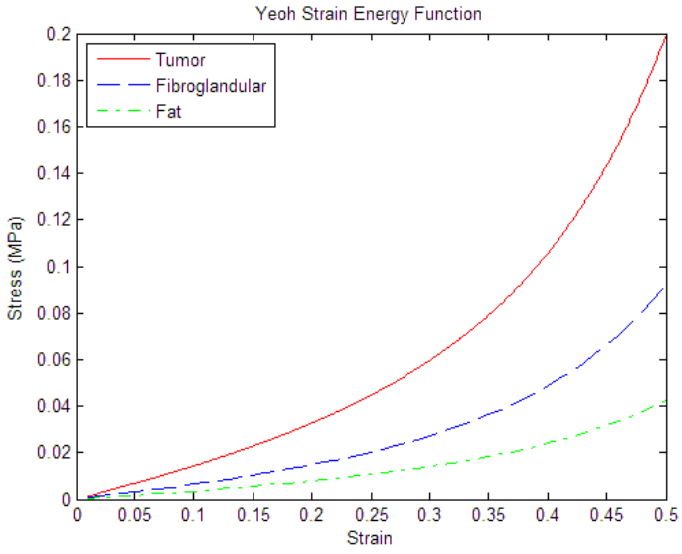

Figure 5-31. True stress-strain relationship of the fat, fibroglandular and tumor tissues of the Yeoh hyperelastic form.

Table 5-10 illustrates the initial guess, true parameter values, calculated parameter values, number of iterations required for convergence, the tolerance used in the convergence criteria, and the percentage error of the calculated values for Yeoh model.

Table 5-10. The initial guess, true values of the hyperelastic parameters, calculated values of the parameters, number of iteration required to reach these values, the tolerances used as convergence criteria and the error percentage of the calculated values for Yeoh model.

	Initial Guess(kpa)	True Value(kpa)	Calculated Value (kpa)	Iteration Number	Tolerance (tol %)	Error (%)
C10 (Yeoh)	0.01	0.0206	0.0220	31	0.07	6.79
C20 (Yeoh)	0.01	0.0068	0.0336	31	0.07	394.11
C30 (Yeoh)	0.02	0.0448	0.0565	31	0.07	26.11

5.2.8. Absolute Reconstruction results for the Veronda-Westmann model

In this section we report the results of applying the reconstruction algorithm to the pre- and post- compression images of the phantom while using the Veronda-Westmann strain energy function to model the hyperelastic behavior of the soft tissues. The convergence of the hyperelastic parameters to their final value are shown for all 3 parameters of the Veronda-Westmann form in Figure 5-32.

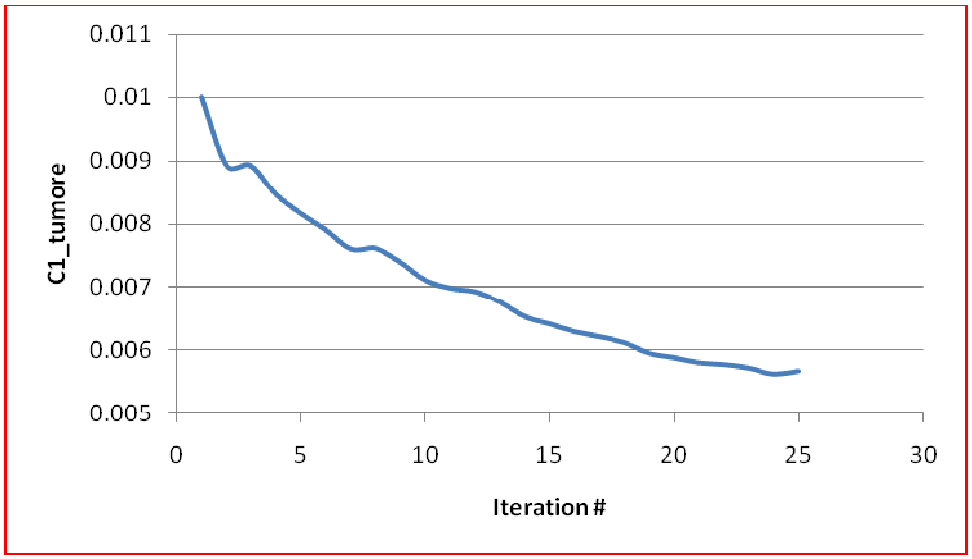

(a)

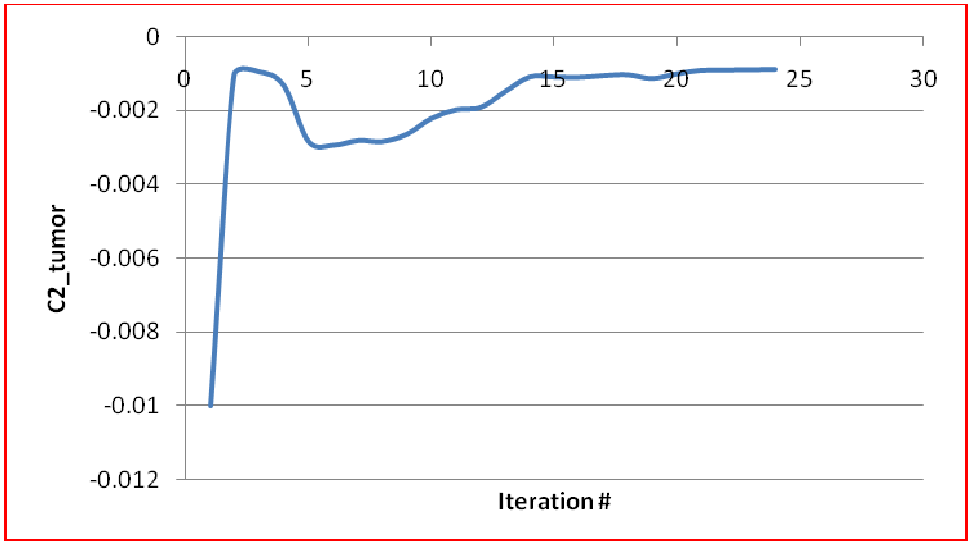

(b)

(c)

Figure 5-32. a, b, c) Convergence of C1, C2 and C3 in the Veronda-Westmann form, respectively.

The stress-strain relationship corresponding to the actual parameters versus the reconstructed parameters for Veronda-Westmann model is shown in Figure 5-33.

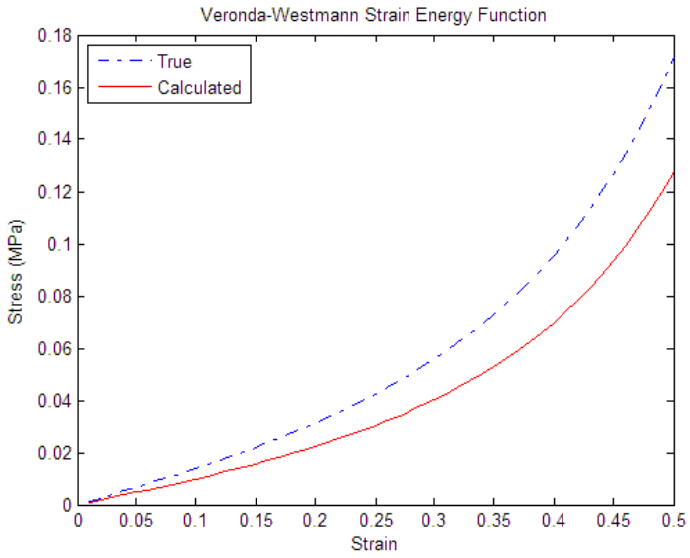

Figure 5-33. True and reconstructed stress-strain curves of the tumor tissue of the Veronda-Westmann hyperelastic model.

In this figure again we witness the same agreement between the reconstructed and true stress-strain curves as discussed for the Polynomial and Yeoh models.

Figure 5-34 shows the stress-strain relationship corresponding to the inner cylindrical part, middle cubic part and outer cubic portion of the phantom used in the analysis for the Veronda-Westmann model.

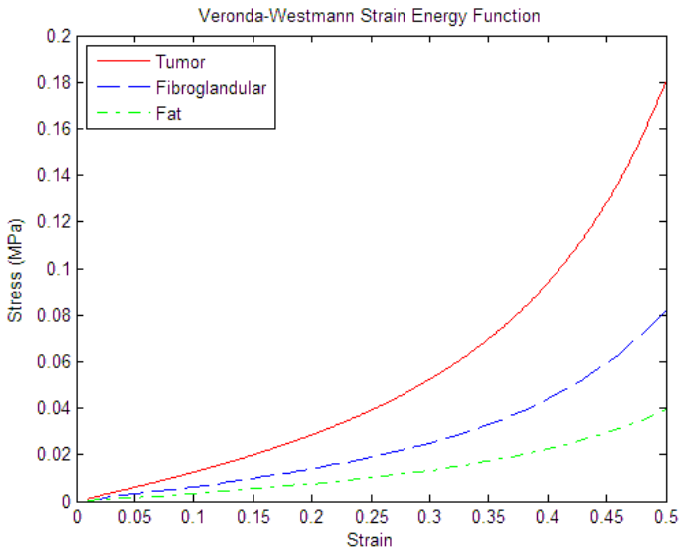

Figure 5-34. True stress-strain relationship of the fat, fibroglandular and tumor tissues of the Veronda-Westmann hyperelastic form.

Table 5-11 illustrates the initial guess, true parameter values, calculated parameter values, number of iterations required for convergence, the tolerance used in the convergence criteria, and the percentage error of the calculated values for Veronda-Westmann model.

Table 5-11. The initial guess, true values of the hyperelastic parameters, calculated values of the parameters, number of iteration required to reach these values, the tolerances used as convergence criteria and the error percentage of the calculated values for Veronda-Westmann model.

	Initial Guess(kpa)	True Value(kpa)	Calculated Value (kpa)	Iteration Number	Tolerance (tol %)	Error (%)
C1 (VW)	0.01	0.0091	0.00566	25	0.09	37.8
C2 (VW)	-0.01	-0.0019	-0.000870	25	0.09	54.21
C3 (VW)	3	2.5875	3.5489	25	0.09	37.15

5.2.9. Relative reconstruction

The results of reconstructing the absolute values of the parameters (Tables 5-9, 5-10 and 5-11) show that there are large errors in the reconstructed values versus the actual values obtained from the uniaxial compression tests. These differences are due to the fact that in our reconstruction algorithm we do not have enough information to measure the absolute values of the parameters for all tissues because of lack of tissue force data.

In order to be able to calculate the absolute values of the parameters, we need the force information of the tissue in addition to the displacement information. To justify this we use the following simple system shown in Figure 5-35.

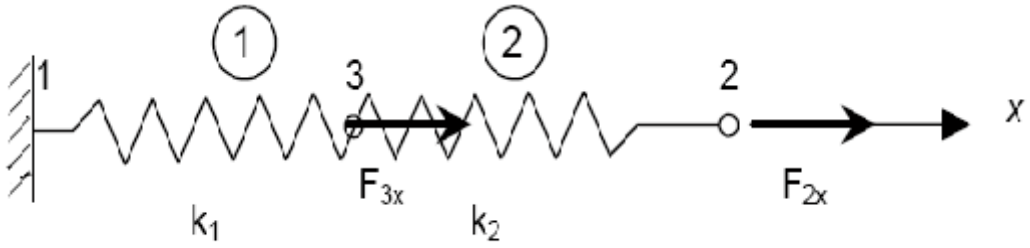

Figure 5-35. The system of two springs connected in series to each other. A known displacement is applied to the system at node 2.

This system is comprised of two springs (k_1 and k_2) connected in series and fixed in one end while a known compression is being applied to their other end. Assuming that we only have information about the amount of compression applied to the system, we can measure the compression of each spring after loading (x_1 and x_2). The force-deformation relationship of the system is:

$$F_{s1} = k_1 x_1 = F$$

$$F_{s2} = k_2 x_2 = F$$

Thus, without having the force information we can only calculate the ratio of the stiffness not their absolute values. The same conclusion applies to our case in which we only have displacement data. Therefore, it is not possible to reconstruct the absolute hyperelastic values without tissue force information.

The relative reconstructed parameters for the phantom are depicted in the following figures.

Figure 5-36 shows the ratio of the parameters reconstructed for the inner cylindrical part to the middle cubic part of the phantom for the Polynomial strain energy function.

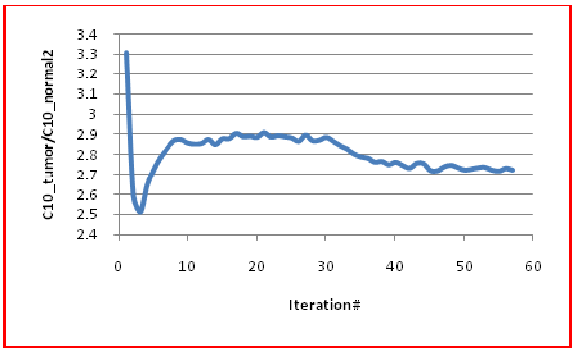

(a)

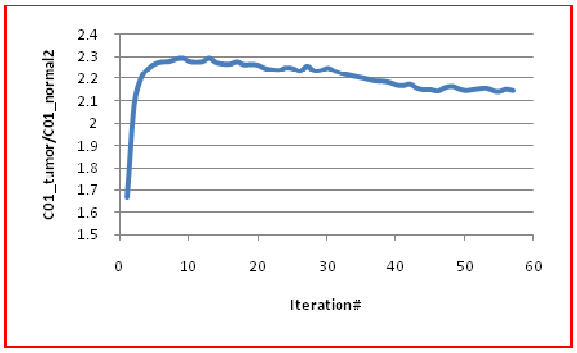

(b)

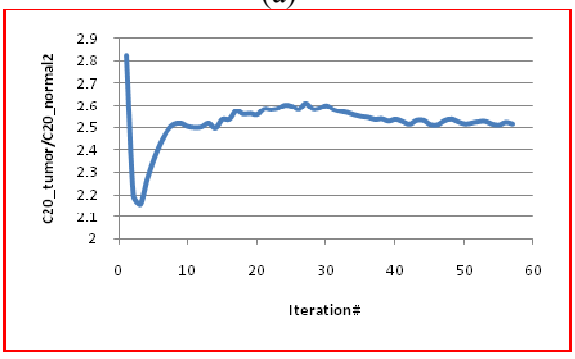

(c)

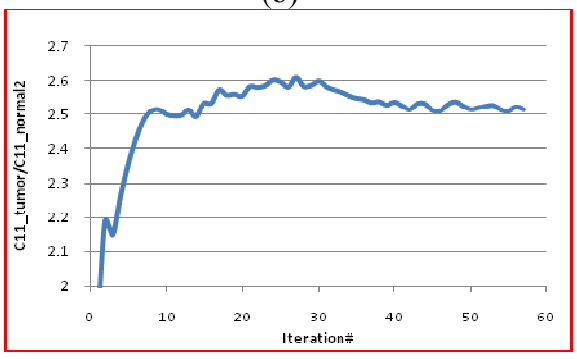

(d)

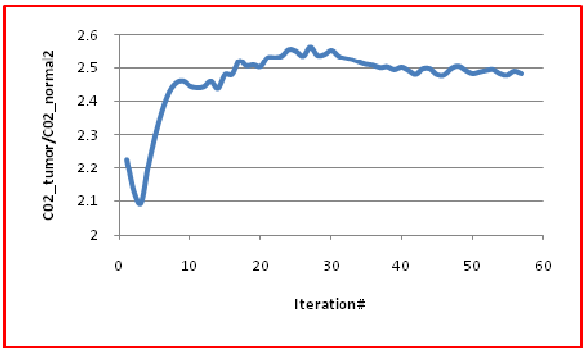

(e)

Figure 5-36. a, b, c, d, e) Convergence of the ratio of C10's, C01's, C20's, C11's and C02's of the tumor tissue to the fibroglandular tissue in the Polynomial form, respectively.

Figure 5-37 shows the ratio of the parameters reconstructed for the inner cylindrical part to the outer cubic part of the phantom for the Polynomial strain energy function.

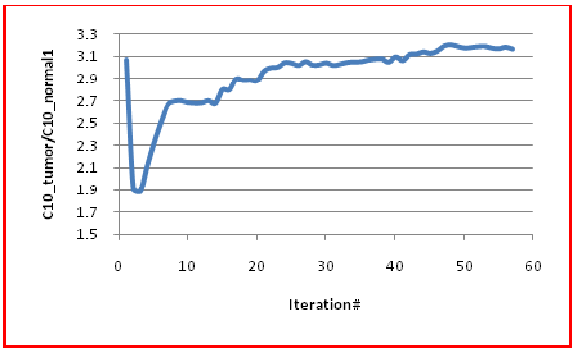

(a)

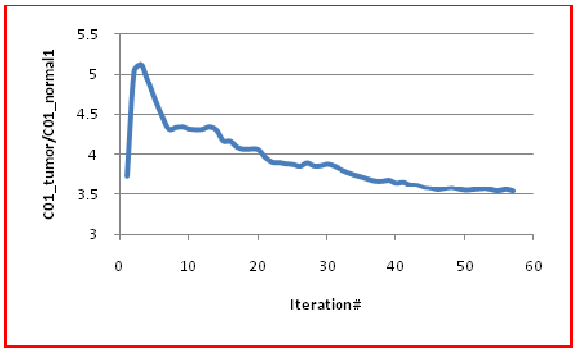

(b)

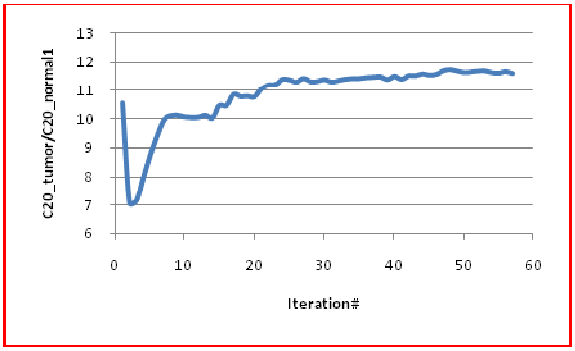

(c)

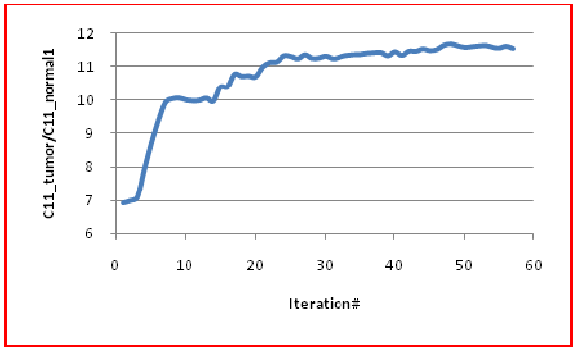

(d)

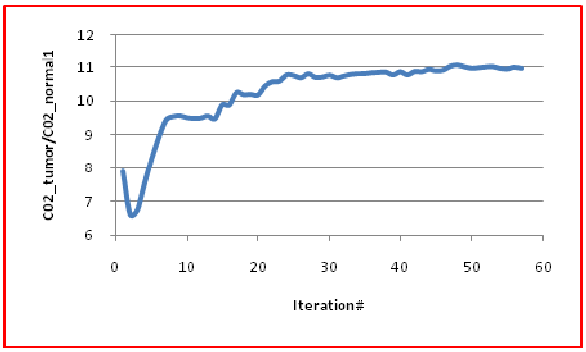

(e)

Figure 5-37. a, b, c, d, e) Convergence of the ratio of C10's, C01's, C20's, C11's and C02's of the tumor tissue to the adipose tissue in the Polynomial form, respectively.

Figure 5-38 shows the ratio of the parameters reconstructed for the middle cubic part to the outer cubic part of the phantom for the Polynomial strain energy function.

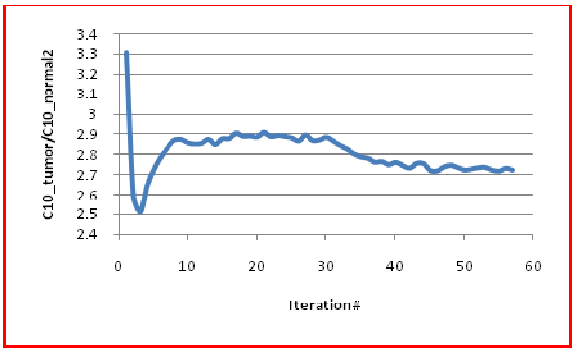

(a)

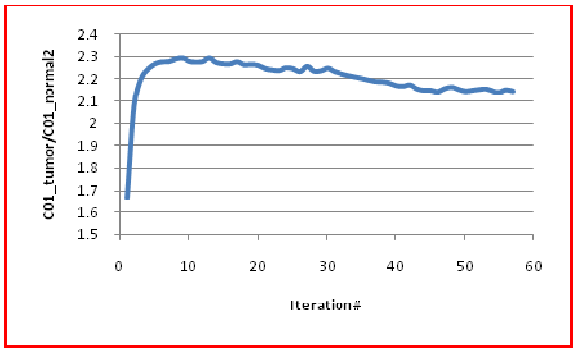

(b)

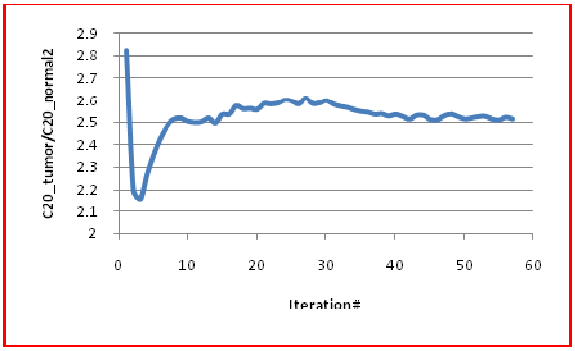

(c)

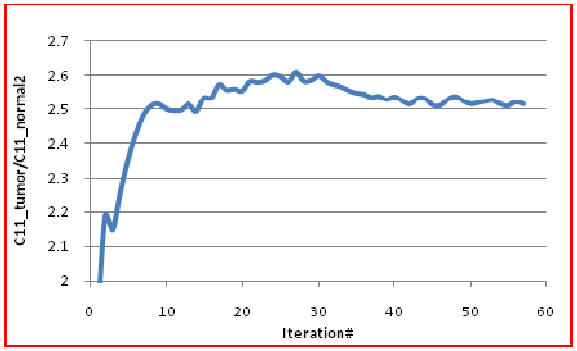

(d)

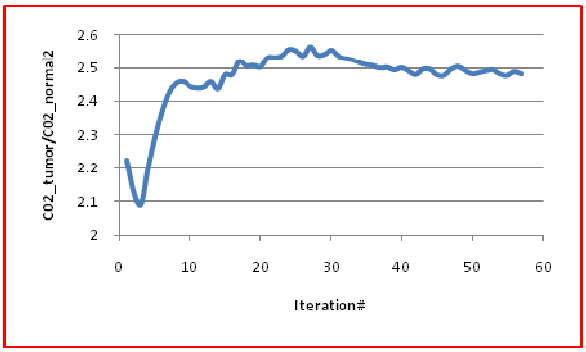

(e)

Figure 5-38. a, b, c, d, e) Convergence of the ratio of C10's, C01's, C20's, C11's and C02's of the tumor tissue to the fibroglandular tissue in the Polynomial form, respectively.

Figure 5-39 shows the ratio of the parameters reconstructed for the inner cylindrical part to the middle cubic part of the phantom for the Yeoh strain energy function.

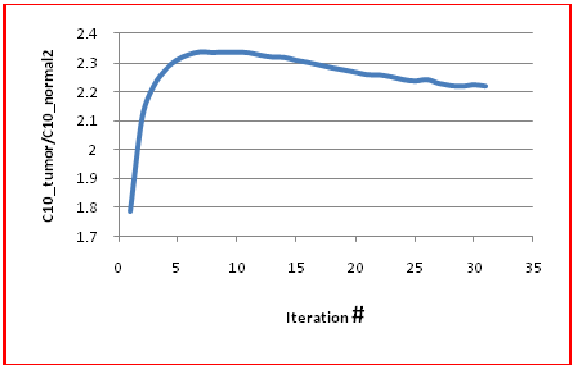

(a)

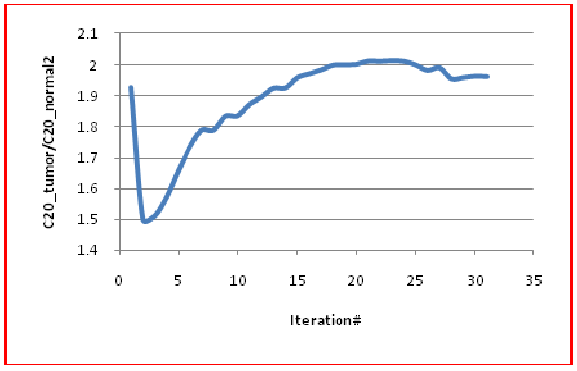

(b)

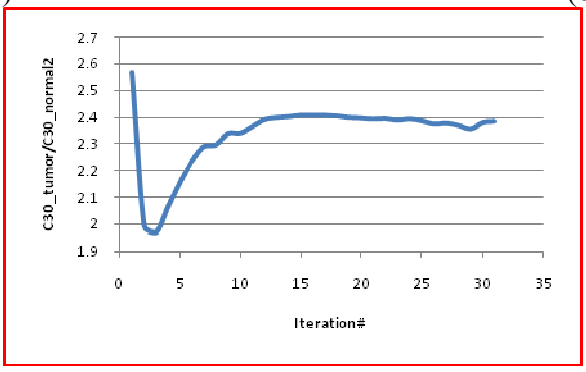

(c)

Figure 5-39. a, b, c) Convergence of the ratio of C10's, C20's and C30's of the tumor tissue to the fibroglandular tissue in the Yeoh form, respectively.

Figure 5-40 shows the ratio of the parameters reconstructed for the inner cylindrical part to the outer cubic part of the phantom for the Yeoh strain energy function.

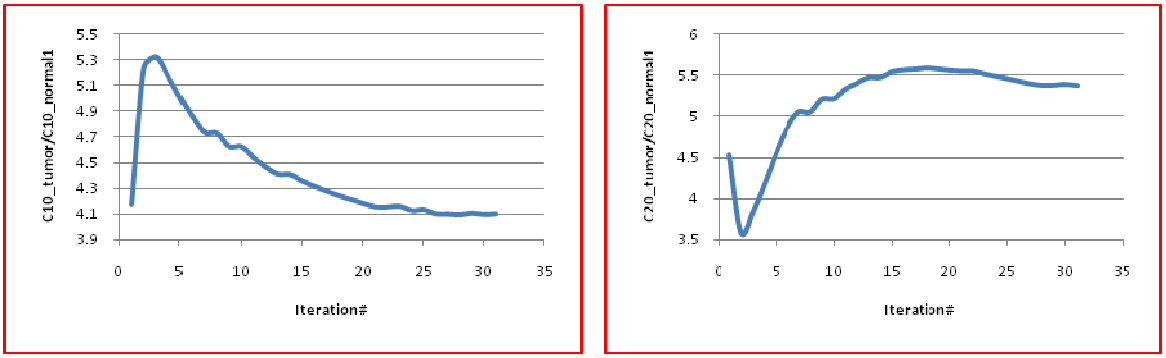

(a) (b)

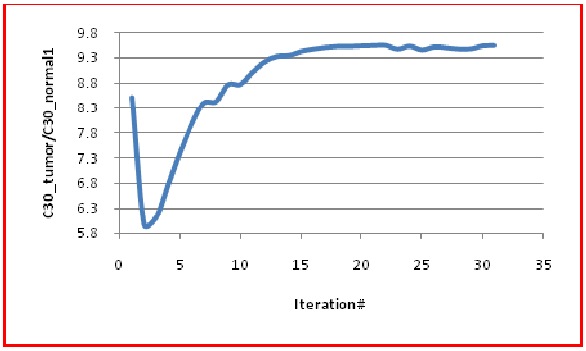

(c)

Figure 5-40. a, b, c) Convergence of the ratio of C10's, C20's and C30's of the tumor tissue to the adipose tissue in the Yeoh form, respectively.

Figure 5-41 shows the ratio of the parameters reconstructed for the middle cubic part to the outer cubic part of the phantom for the Yeoh strain energy function.

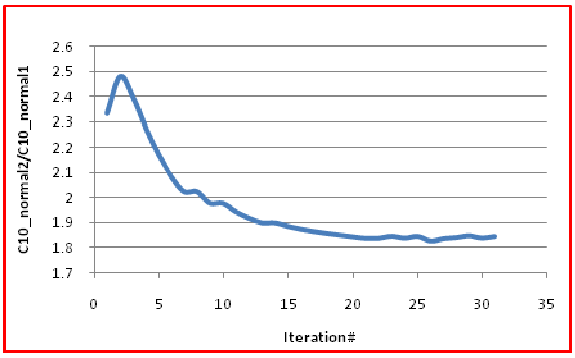

(a)

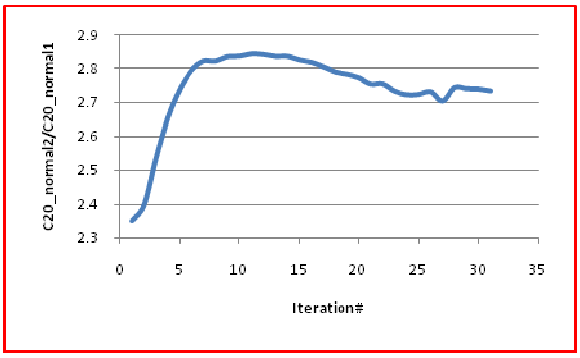

(b)

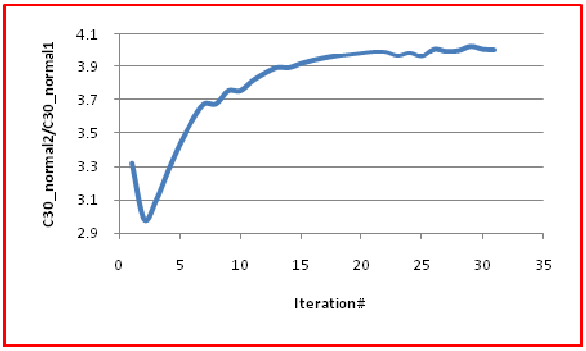

(c)

Figure 5-41. a, b, c) Convergence of the ratio of C10's, C20's and C30's of the fibroglandular tissue to the adipose tissue in the Yeoh form, respectively.

Figure 5-42 shows the ratio of the parameters reconstructed for the inner cylindrical part to the middle cubic part of the phantom for the Veronda-Westmann strain energy function.

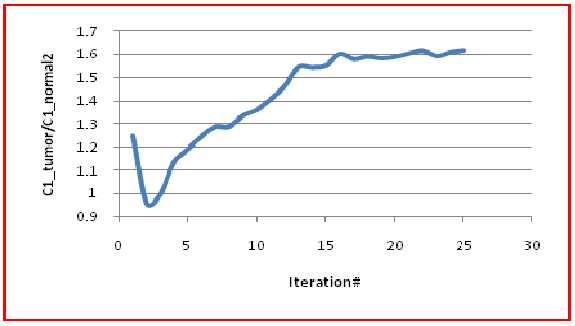

(a)

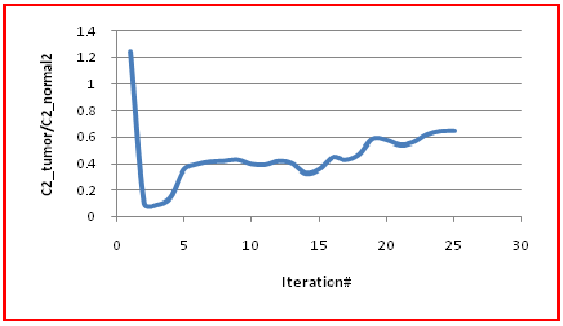

(b)

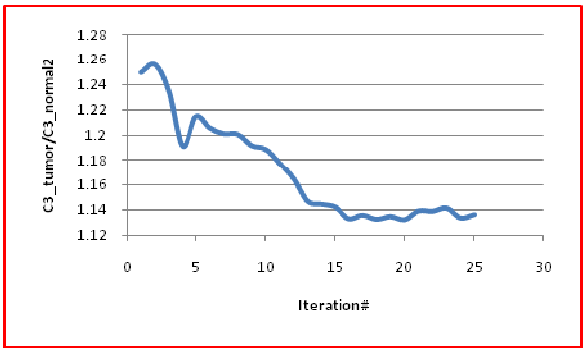

(c)

Figure 5-42. a, b, c) Convergence of the ratio of C1's, C2's and C3's of the tumor tissue to the fibroglandular tissue in the Veronda-Westmann form, respectively.

Figure 5-43 shows the ratio of the parameters reconstructed for the inner cylindrical part to the outer cubic part of the phantom for the Veronda-Westmann strain energy function.

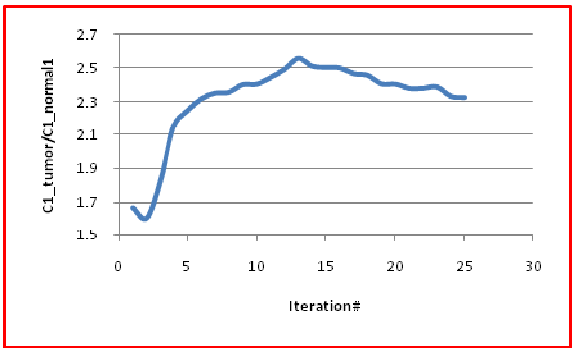

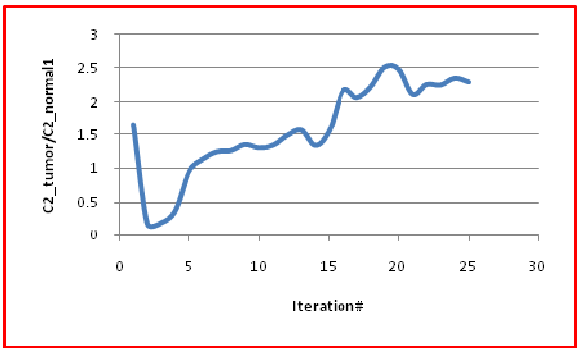

(a) (b)

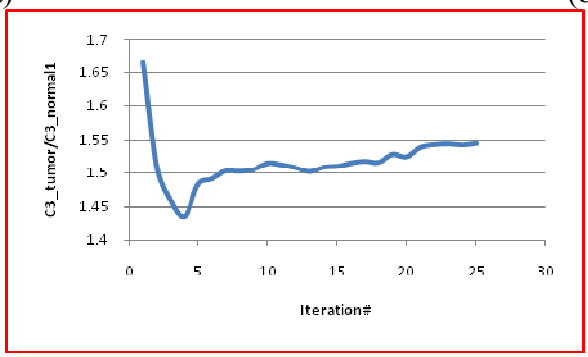

(c)

Figure 5-43. a, b, c) Convergence of the ratio of C1's, C2's and C3's of the tumor tissue to the adipose tissue in the Veronda-Westmann form, respectively.

Figure 5-44 shows the ratio of the parameters reconstructed for the middle cubic part to the outer cubic part of the phantom for the Veronda-Westmann strain energy function.

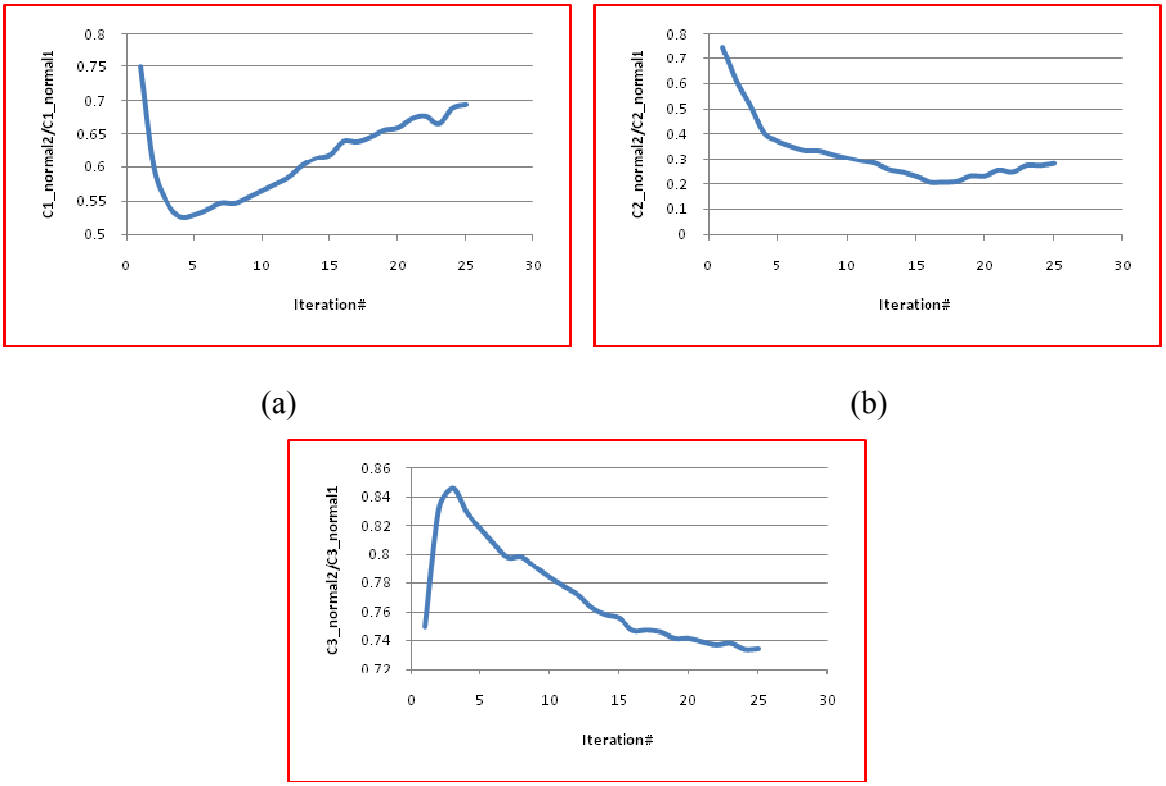

Figure 5-44. a, b, c) Convergence of the ratio of C1's, C2's and C3's of the fibroglandular tissue to the adipose tissue in the Veronda-Westmann form, respectively.

Table 5-12 gives the ratio of the C10's, C01's, C20's, C11's and C02's of the tumor tissue to the fibroglandular tissue, for both reconstruction and uniaxial test results and their error percentage for Polynomial model.

.

Table 5-12. Ratio of the C10's, C01's, C20's, C11's and C02's of the tumor tissue to the fibroglandular tissue, for both reconstruction and uniaxial test results and their error for the Polynomial model

	C_{10}_t/C_{10}_n2 (Polynomial)	C_{01}_t/C_{01}_n2 (Polynomial)	C_{20}_t/C_{20}_n2 (Polynomial)	C_{11}_t/C_{11}_n2 (Polynomial)	C_{02}_t/C_{02}_n2 (Polynomial)
Reconstructed	2.725	2.145	2.516	2.517	2.481
Uniaxial test	2.982	2.050	2.956	2.782	2.936
Error (%)	8.614	4.650	14.907	9.537	15.502

Table 5-13 gives the ratio of the C10's, C01's, C20's, C11's and C02's of the tumor tissue to the adipose tissue, for both reconstruction and uniaxial test results and their error percentage for the Polynomial model.

.

Table 5-13. Ratio of the C10's, C01's, C20's, C11's and C02's of the tumor tissue to the adipose tissue, for both reconstruction and uniaxial test results and their error for the Polynomial model

	C_{10}_t/C_{10}_n1 (Polynomial)	C_{01}_t/C_{01}_n1 (Polynomial)	C_{20}_t/C_{20}_n1 (Polynomial)	C_{11}_t/C_{11}_n1 (Polynomial)	C_{02}_t/C_{02}_n1 (Polynomial)
Reconstructed	3.170	3.545	11.608	11.554	10.973
Uniaxial test	3.561	3.843	11.025	10.75	11.137
Error (%)	10.975	7.769	5.289	7.483	1.480

Table 5-14 gives the ratio of the C10's, C20's and C30's of the tumor tissue to the fibroglandular tissue, for both reconstruction and uniaxial test results and their error percentage for the Yeoh model.

.

Table 5-14. Ratio of the C10's, C20's and C30's of the tumor tissue to the fibroglandular tissue, for both reconstruction and uniaxial test results and their error for the Yeoh model

	C_{10}_t/C_{10}_n2 (Yeoh)	C_{20}_t/C_{20}_n2 (Yeoh)	C_{30}_t/C_{30}_n2 (Yeoh)
Reconstructed	2.220	1.964	2.385
Uniaxial test	2.607	2.137	1.947
Error (%)	14.850	8.106	22.448

Table 5-15 gives the ratio of the C10's, C20's and C30's of the tumor tissue to the adipose tissue, for both reconstruction and uniaxial test results and their error percentage for the Yeoh model.

.

Table 5-15. Ratio of the C10's, C20's and C30's of the tumor tissue to the adipose tissue, for both reconstruction and uniaxial test results and their error for the Yeoh model

	C_{10}_t/C_{10}_n1 (Yeoh)	C_{20}_t/C_{20}_n1 (Yeoh)	C_{30}_t/C_{30}_n1 (Yeoh)
Reconstructed	4.098	5.371	9.563
Uniaxial test	4.478	4.769	8.296
Error (%)	8.472	12.633	15.278

Table 5-16 gives the ratio of the C1's, C2's and C3's of the tumor tissue to the fibroglandular tissue, for both reconstruction and uniaxial test results and their error percentage for the Veronda-Westmann model.

Table 5-16. Ratio of the C1's, C2's and C3's of the tumor tissue to the fibroglandular tissue, for both reconstruction and uniaxial test results and their error for the Veronda-Westmann model.

	C_1_t/C_1_n2 (Yeoh)	C_2_t/C_2_n2 (Yeoh)	C_3_t/C_3_n2 (Yeoh)
Reconstructed	1.616	0.654	1.136
Uniaxial test	1.378	0.566	1.291
Error (%)	17.243	15.518	12.001

Table 5-17 gives the ratio of the C1's, C2's and C3's of the tumor tissue to the adipose tissue, for both reconstruction and uniaxial test results and their error percentage for the Veronda-Westmann model.

Table 5-17. Ratio of the C1's, C2's and C3's of the tumor tissue to the adipose tissue, for both reconstruction and uniaxial test results and their error for Veronda-Westmann model

	C_1_t/C_1_n1 (Yeoh)	C_2_t/C_2_n1 (Yeoh)	C_3_t/C_3_n1 (Yeoh)
Reconstructed	2.329	2.299	1.546
Uniaxial test	2.116	2.833	1.662
Error (%)	10.065	18.845	6.999

6. Summary and Conclusions

Based on the fact that breast tissue abnormalities are associated with changes in their mechanical properties, the goal of this work was to develop a noninvasive technique to reconstruct breast tissues hyperelastic parameters *in vivo*. The motivation of this research is to improve specificity of elastography by adding hyperelasticity to the system. Our objective is to characterize the existing tumor assuming that we know its existence in the body. Our main interest is not detecting the presence of tumor, since it can be done accurately with conventional imaging techniques and linear elastography.

6.1. Hyperelastic elastography for breast tissues

To achieve our goal in this research, we used elastography. Unlike in classical elastography techniques in which the tissue is assumed to show linear mechanical behavior characterized by the Young's Modulus, in this work we are interested in parameters that characterize the tissue nonlinear behavior. Reconstructing tissues' Young's modulus is valid for only a small strain range. On the contrary, reconstructing the non-linear (hyperelastic) parameters of the tissue, as described in second chapter, is valid for the entire range of strain. For the breast, since the tissues are very soft, their deformation tends to be significant when they undergo small excitation. Therefore, modeling the non-linear behavior, which accounts for tissue intrinsic and geometric nonlinearities is very important.

6.2. Sensitivity and Specificity

It is shown that presence of pathology in the breast results in alteration of the mechanical properties of its tissue. Malignant or benign breast tumors are usually stiffer than normal breast tissues. Furthermore, among tumors, malignant breast tumors are significantly stiffer compared to benign tumors. Therefore, knowing the mechanical properties of breast tissues using elastography is not only capable of detecting presence of abnormality in the breast (sensitivity), it is capable of classifying the type the detected abnormality (specificity). The latter is a major weakness of all other imaging techniques. While the sensitivity and specificity of elastography techniques that image the Young's modulus or shear modulus are reasonably good, images they provide are sensitive to the amount of breast pre-compression applied during the the procedure. As mentioned earlier, given the nonlinear nature of breast tissues, the reconstructed Young's modulus is valid only for a small range of strain. If the strain range is altered as a result of applying a different pre-compression, the reconstructed Young's modulus will be totally different. Hence, an elastography technique that assumes tissue linear behavior can be associated with significant errors which may lead to inaccurate image. The first objective of my research was modeling the hyperelastic parameters of breast tissue that is expected to progress elastography for cancer diagnosis.

6.3. Choice of hyperelastic model

Several hyperelastic models are available for modeling tissues' nonlinear mechanics. A number of these models (Polynomial, Yeoh, Veronda-Westmann, Reduced Polynomial, Ogden, Mooney-Rivlin and Neo-Hookean) were described in the Theory Chapter. In this work, we used three of these models that are used extensively in modeling soft tissues.

These models are the Polynomial model with 5 parameters, the Yeoh model that has 3 parameters and the Veronda-Westmann model with 3 parameters. The Polynomial model with $N = 2$ (having 5 parameters) is a commonly used hyperelastic model for breast tissue modeling. The Yeoh model is also known as a model capable of simulating soft tissue mechanics with high accuracy. This model is only dependent on the first strain invariant and, therefore, is more stable than other models. The Veronda-Westmann model was first presented for skin modeling but it is becoming more popular in breast tissue simulation due to its exponential form. These three models are common models used in literature and all of them have been used for soft tissue modeling. These three models are used in this study and results for both numerical and experimental simulations are presented in the Results Chapter.

6.4. Meshing and displacement data acquisition

In order to reconstruct the parameters, as presented in the Methods Chapter, it is required to extract the tissue displacement data while compression is applied. In this work, we applied large amount of compression (around 30%) to the phantom in order for the deformation to enter the tissues' nonlinear regime. For the simulation stage, a phantom comprised of a cylinder connected to a hemisphere was used to represent a simplified breast geometry. This model has three different tissue types representing the Fat, Fibroglandular and tumor tissues present in a cancerous breast. The phantom was developed numerically using ABAQUS finite element solver. To measure the displacement field, the phantom was compressed using ABAQUS simulation and displacements were input from ABAQUS output files.

The experimental phantom is a cube with three tissue types. This phantom was constructed using Polyvinyl Alcohol (PVA). The phantom is made such that it satisfied plane stress state, thus only the displacements of the surface of the phantom are adequate for analysis. A grid of 25×24 was placed manually on the phantom and the displacements were measured manually by tracking each grid node on photos of the phantom taken before and after compression.

6.5. Reconstruction Technique

The hyperelastic parameters reconstruction was performed using an iterative approach presented in the Theory Chapter. The problem is formulated as an inverse problem in which the parameters are updated at each iteration until convergence is achieved. The input to the inverse problem is the tissue deformation gradient field. On the other hand an initial guess is used for the parameters and ABAQUS is employed to calculate the tissues' nodal stresses. Hence, at each iteration, the inverse problem is solved to obtain a new set of parameters. Next, this new set is used to calculate the new stress field. The process is repeated until convergence is achieved. The goal of our research was to prove the concept of the proposed technique. This analysis is the first step to provide a hyperelastic cancer diagnosis system to be used in clinical applications. We demonstrated that the hyperelastic behavior of soft tissues can be reconstructed *in vivo* using our algorithm. It is required to come up with a metric that is capable of translating the results of the reconstruction into a more clinically applicable framework. This is out of scope of our research in this thesis.

6.6. Numerical Simulation

In order to validate the proposed elastography technique, we first performed numerical simulation on the numerical phantom shown in Figure 5-1. The phantom is made such that it simulates a cancerous breast with simplified geometry. The goal of this work is to measure the hyperelastic properties of the tumor tissue. Therefore, in this simulation we assumed to know the hyperelastic properties of normal breast tissues. Samani *et al* [58] indicated that the hyperelastic parameters of the normal breast tissues can be measured independently. They reported these parameters for a Polynomial model of normal breast tissues. This information is used in the reconstruction technique to depict the effectiveness of the method in calculating the parameters for real breast tissues. The reconstruction algorithm was applied to the phantom using three different hyperelastic models. The Polynomial model with $N = 2$, the Yeoh model and the Veronda-Westmann model. The reconstruction showed encouraging results in constructing the hyperelastic properties of the tumor tissue. As reported in Tables 5-1, 5-2 and 5-3 all parameters were reconstructed with high accuracy. The results demonstrated that it is feasible to accurately reconstruct breast tissue hyperelastic parameters from measured displacement data.

The system of equation becomes ill-condition for the Polynomial model. Therefore, solving the inverse problem is not straight forward in this case. We used a novel regularization technique that uses three different regularizing methods sequentially during the iterative reconstruction process. The impact of using this regularization technique is reaching convergence in a relatively high number of iterations. Since regularization is used in each iteration, reconstruction errors are accumulated and the

final reconstructed values will have larger error percentage (the largest error is about 2%) compared to other methods. The advantage of using the Polynomial model is that it uses 5 parameters to model the mechanical behavior of the tissue and thus is capable of modeling the tissue with high accuracy. The other reason in our interest for using this model is its common use in modeling breast tissues.

For Yeoh model, all three parameters were reconstructed with error of less than 1% in a small number of iterations compared to the Polynomial model (less than half the number of iterations). Yeoh strain energy function is a hyperelastic model that is only dependent on the first strain invariant but it is capable of modeling soft tissues with accuracy close to that of Polynomial model [31]. The Polynomial model depends on strain invariants I_1 and I_2 while Yeoh model depends only on one strain invariant I_1. As discussed in the Methods Chapter, dependence on the second invariant makes the system unstable. The Yeoh model converges in less iterations than the Polynomial model with higher accuracy, therefore, eliminating I_2 dependent terms in the strain energy function results in higher stability in the system.

For the case of Veronda-Westmann model convergence was achieved in even smaller number of iteration than the Yeoh model with less than 1% error. This demonstrates the efficiency of the Veronda-Westmann model compared to the Yeoh model. Although Veronda-Westmann model like the Polynomial model is dependent in both I_1 and I_2 strain invariants whereas Yeoh model is only dependent on the I_1 strain invariant, its fast convergence can be attributed to the exponential form of the Veronda-Westmann. As can be seen in Figure 5-11 a, b and c, the parameter values approach their final value smoother than other models and in a few iterations.

6.7. Linear Phantom Study

To validate the method experimentally, we performed a phantom study. In our experiment, we used a cubic phantom comprised of three different tissue types. In order to simplify the 3-D phantom study, which can be time consuming and requires advanced imaging techniques to image the 3-D displacement field, we made the phantom such that is satisfies a plane stress state. As such, we only need the displacements of the surface nodes of the phantom which can be measured manually using two photos of the phantom taken before and after compression. The error introduced to the system by using this assumption was calculated by simulation. The results were reported in the Methods Chapter. These results showed that the error in the displacement is less than 5%, thus this assumption is reasonable. As first step, we constructed a phantom out of gelatin that exhibits linear mechanical behavior. This phantom is shown in Figure 4-1. We also performed uniaxial compression test on cylindrical samples of each tissue type to measure their mechanical properties (Young's modulus in this case) independently. The results of applying the reconstruction algorithm was reported in Table 5-5. The reconstruction results showed that the algorithm is capable of measuring the mechanical properties of the tissue. The error in the reconstruction was about 2%, which is very low especially taking into account the simlifying assumptions and the errors introduced to the system by manually extracting the displacement data.

6.8. Hyperelastic Phantom Study

The final and main step of this work was to reconstruct the hyperelastic parameters of the soft tissues experimentally. We constructed a phantom similar to the one we had in our linear phantom study step but using Polyvinyl Alcohol (PVA). This phantom is shown in

Figure 4-4. Similar to the linear case, we used cylindrical samples of each tissue type to measure their hyperelastic properties independently using uniaxial tests. Using the plane stress assumption, a mesh was placed on the surface of the phantom and the displacement data was extracted manually from pre- and post-compression photos of the phantom. We applied the reconstruction technique to the phantom to measure the absolute value of the parameters. In this case we did not assume to know the parameters of normal tissue types and tried to reconstruct the parameters for all three tissue types. The results of this showed large differences between the actual parameter values (obtained from uniaxial tests) and the reconstructed values as reported in Tables 5-9, 5-10 and 5-11. The reason for this difference is that we only have the displacement data and as described in the Results Chapter, it is not possible to reconstruct the absolute values of the parameters using only this data. Absolute value reconstruction requires tissue force information in addition to displacement information. Since in breast cancer detection and diagnosis, the absolute values of parameters are not of interest and the presence and type of abnormality can be determined by the ratio of these parameters, reconstruction of parameters relative values is sufficient. As reported in Tables 5-12, 5-13, 5-14, 5-15, 5-16 and 5-17 the relative reconstruction yields better results. The reconstructed ratios were constructed with less than 20% error.

For the Polynomial model, similar to the numerical study, we encountered an ill-conditioned system of equations. The same sequential regularization technique was used here and the algorithm was guided towards convergence. Again, convergence required large number of iterations and the error of the reconstruction was high due to the combination of regularization and experiment errors.

For the Yeoh model, although the number of iteration was less than the Polynomial model and the fact that it only uses the first strain invariant (I_1) we observed larger errors in the reconstructed ratios compared to the Polynomial model.

The Veronda-Westmann model converged in even fewer iterations but the error in the system is relatively higher than the Polynomial model but less than the Yeoh model. The error in all methods is less than 20%, which shows that the algorithm is capable of reconstructing the parameters with acceptable accuracy.

Figures 5-27, 5-30 and 5-33 show that, although the parameters are reconstructed with about 20% error, the stress-strain curves of the actual parameters versus the reconstructed parameters are very close to each other. This is due to the fact that the cost function of our inverse problem is formulated in a way that it minimizes the difference between the experimental and calculated stress versus strain relationship in a least squares manner. Therefore, the agreement between the experimental and calculated stress-strain curves was better than the parameters agreement in all models. This agreement is even higher in the beginning of the curves where the tissue is still in the linear portion of is mechanical behavior. Another fundamental difference between the reconstructed parameters and the parameters obtained from uniaxial test is that the reconstructed parameters are obtained from fitting the measured displacements to a complex loading situation where all tensor stress components are present. This is not the case with a uniaxial test where only one stress component is present. This fundamental difference accounts for part of the disagreement. The accuracy achieved in this phantom study is reasonably good considering the several issues in the experiments. We speculate that this accuracy is adequate for the purpose of breast cancer detection and diagnosis as

cancerous tissues are much significantly stiffer than normal tissues, and among tumors malignant tumors are stiffer than benign ones.

6.9. Choosing the best model

In this study we performed several analyses for Polynomial, Yeoh and Veronda-Westmann strain energy functions. We compared these models and the performance of the proposed constrained reconstruction technique for each model. The results of both experimental and numerical studies showed that all three models are capable of reconstructing the parameters with acceptable accuracy. Therefore all three models satisfy our first objective.

The accuracy of the models is comparable and taking into account that this research field is in its infancy and requires further research to identify the most appropriate model for various applications. Choosing the best model and making firm conclusion about suitability for various applications is out of the scope of this work.However, based on the simulated and experimental phantom studies we performed, the Veronda-Westmann model seems to be the best model. This model requires less number of iterations compared to other models, its accuracy in relatively reconstructing the parameters is acceptable and the main point of this model is that it provided the most stable system of equations in the inverse problem.

6.10. Problems and Issues of the Method

In this section the advantages and disadvantages of the method in addition to the problems in performing the experiments will be discussed.

6.10.1. Pros of the Method

The proposed reconstruction algorithm is relatively fast and requires small number of iterations to calculate the parameter values compared to optimization based methods. Other advantage of this method to optimization based methods is using the displacement data as input of the reconstruction technique and updating the parameters systematically based on the information extracted from the phantom, thus it is unlikely to get trapped in a local minimum. This is not the case with optimization based methods, especially for the Polynomial model that has 5 parameters, where the probability of convergence to a local minimum is high. The method is capable of reconstructing the ratios of the hyperelastic parameters efficiently. The error in the results does not affect the sensitivity or specificity of cancer diagnosis process because the contrast between the parameters in a cancerous tissue is expected to be significantly more than errors of the system.

6.10.2. Cons of the Method

One of the difficulties in applying the method to soft tissues is its requirement for extracting displacement data of the phantom. This is difficult to perform especially in 3-D space. In our case, since the goal was to prove the concept of the proposed technique, we used an idealization assumption to simplify the 3-D problem into a 2-D one. Given the breast's complex geometry, it is not possible to make such assumption in clinical applications. One possibility to address this issue is to use MR phase imaging techniques to acquire tissue displacement data. With other imaging modalities, e.g. US, it may be possible to acquire the displacements data using RF signal correlation techniques.

6.10.3. Other issues

There were other significant issues in implementing the method and performing the experiments that we faced and tried to minimize. However, their effects led to inevitable increase of the errors. The first problem of the experiments was the difference between the cylindrical samples of the tissues used in the uniaxial tests and the tissues themselves. This difference is mostly in the tumor tissue whose reconstruction was the goal of this work. The process of freezing and thawing involves cooling the tissue up to -20° and then warming it up to $+20^{\circ}$. This process is repeated a number of times to make the phantom. Since the tumor was embedded inside the phantom, its temperature does not follow temperature of the environmental chamber exactly whereas the temperature change of the cylindrical sample is the same as the chamber. Thus the properties of the tumor tissue in the phantom differ from the cylindrical phantom. The other source of error in the experiment is the phantom photo acquisition process. The photos are taken using a digital camera from a fixed distance. The error in the camera lens is also added to the system. As a result of this error the displacements of the point far from the center of the lens are different from their actual values. Another source of inconsistency between the results of reconstruction and uniaxial compression test is the tissue loading differences between the phantom's tissues and the cylindrical samples as was described earlier. The final problem of the method was extracting the displacement manually. This is prone to human errors. This problem is magnified where the displacements of the tissue is small. Since each node in the mesh placed on the phantom's surface was a small circular area and not an ideal point, identifying the theoretical node and tracking it was impossible. To minimize this error, we performed the displacement extraction process

several times (10 times) and by averaging these data for each node a better approximation for the displacement was achieved [59].

6.11. Future Work and Suggestions

In this work we developed a novel diagnosis method for breast cancer assessment. Here, we proved the concept of the method and tested its feasibility numerically and by phantom experiment. Future work may involve applying this method to real a breast. In this research we had geometric simplification; the geometry has to become more complex for the method to be applicable to breast tissues. For the experimental analysis we performed 2-D reconstruction, to make the method clinical this has to be extended to 3-D analysis which requires 3-D imaging and 3-D tissue displacement data acquisition. In this thesis we developed the method such that it is capable of reconstructing relative parameters. It would be more useful if the force information could be added to the system so that the absolute parameter values could be measured. Adding force information in addition to making the method capable of reconstructing the absolute parameter values may speed up the reconstruction process.

In this study we performed constrained reconstruction by assuming each tissue type to be homogeneous. This means having one set of parameters for the every point of each tissue type. For future work it is desirable to add some level of inhomogeneity to each tissue type to model the breast tissue more accurately. It would also be more desirable to use faster finite element solving tools especially with 3-D cases. Using image processing techniques such as optical flow for displacement data acquisition is another possibility that can be pursued for real-time implementation of this technique. Along these lines, we have developed an optical flow technique, which takes advantage of the tissues'

mechanical properties information. This method combines the conventional optical flow method with the parameter reconstruction method to improve the performance of optical flow for large deformations [60]. This has been done in 2-D and numerical validation of this idea has been performed [61-63]. Another possibility for future research is to extend this method to 3-D.

It is known that the Young's moduli of tumor tissues are higher than that of normal tissues. The ratio of these parameters can be used for classifying different tumor tissues. The same concept could be applied using the hyperelastic parameters of the tumor and normal tissues. For this purpose, a database of hyperelastic parameters of different tumor and normal tissues and the ratios of these parameters is required to classify different tumor types.

7. Appendix A.

7.1. Algebraic Grid Generation using Transfinite Interpolation

The TFI approach to grid generation is based on the concept of mapping a computational domain *C* (logical space) into a closed and bounded region defined in the physical domain *P*. TFI is simple in its implementation and only requires a unique mapping between the boundaries of the two domains $\vec{F} : \partial C \rightarrow \partial P$ be defined.

In 2D *C* takes the form of the unit square, i.e. $C : (\xi, \eta) \in [0,1]$. The mapping function

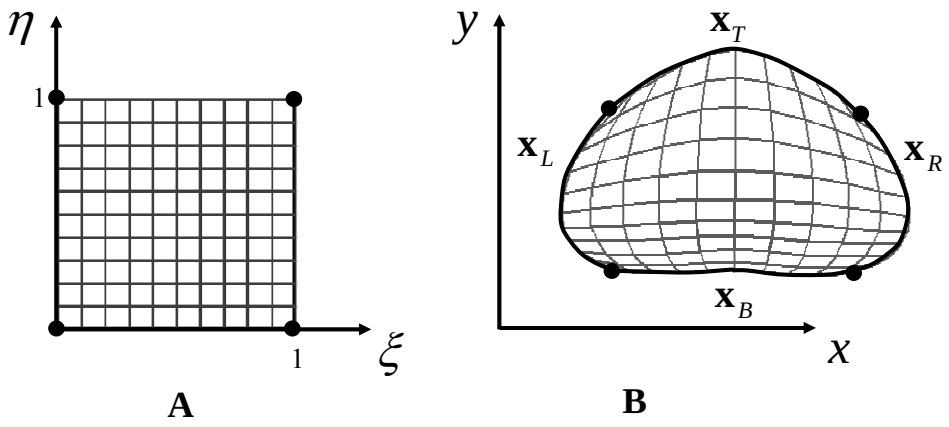

Figure 7-1. A unit square (logical space) (A). A prostate shaped physical space (B).

$\vec{F}$ is constructed by partitioning ∂P into four curves parameterized using the coordinates of ∂C(Figure 7-1):

$$\mathbf{x}_L = (x_L, y_L) = \vec{F}(0,\eta) \qquad \mathbf{x}_R = (x_R, y_R) = \vec{F}(1,\eta)$$
$$\mathbf{x}_B = (x_B, y_B) = \vec{F}(\xi,0) \qquad \mathbf{x}_T = (x_T, y_T) = \vec{F}(\xi,1) \qquad \text{7-1}$$

,

that are joined at four corners denoted by:

$$\mathbf{x}_{TR} = (x_{TR}, y_{TR}) = \vec{F}(1,1) \qquad \mathbf{x}_{BR} = (x_{BR}, y_{BR}) = \vec{F}(1,0)$$

$$\mathbf{x}_{TL} = (x_{TL}, y_{TL}) = \vec{F}(0,1) \qquad \mathbf{x}_{BL} = (x_{BL}, y_{BL}) = \vec{F}(0,0)$$

,

Using $\vec{F}$ (equation 7-1), we can now construct a TFI mapping function from *C* to *P* using the *vector-valued bilinear blended map*:

$$\mathbf{x}(\xi,\eta) = \begin{bmatrix} x(\xi,\eta) \\ y(\xi,\eta) \end{bmatrix} = \begin{array}{l} (1-\eta)\mathbf{x}_B + \eta\mathbf{x}_R + (1-\xi)\mathbf{x}_T \\ +\xi\mathbf{x}_R - \xi\eta\mathbf{x}_{TR} - \xi(1-\eta)\mathbf{x}_{BR} \\ -\eta(1-\xi)\mathbf{x}_{TL} - (1-\xi)(1-\eta)\mathbf{x}_{BL}. \end{array} \qquad 7\text{-}2$$

In order to generate the vertices of a grid over the closed shape in Cartesian domain *P* (Figure 7-1 B) an $N \times N$ computational grid $\mathbf{x}_c = \left(i \cdot \frac{1}{N-1}, j \cdot \frac{1}{N-1} \right)$, $i, j, k = 0,1,\ldots,N-1$ is defined and then mapped into *P* using equation. 7-2. It is important to note that when $\mathbf{x}_c$ is a rectilinear grid this technique only requires that $\vec{F}$ be defined for the vertices on the outer surface of $\mathbf{x}_c$.

In 3D, *C* takes the form of a unit cube, i.e. $C : (\xi,\eta,\zeta) \in [0,1]$. The mapping function $\vec{F}$ is constructed by partitioning ∂P into six surfaces adjoining surfaces parameterized using the coordinates of ∂C (Figure 7-2):

$$\mathbf{x}_N = \vec{F}(\xi,1,\zeta) \qquad \mathbf{x}_E = \vec{F}(1,\eta,\zeta)$$

$$\mathbf{x}_S = \vec{F}(\xi,0,\zeta), \qquad \mathbf{x}_W = \vec{F}(0,\eta,\zeta), \qquad 7\text{-}3$$

$$\mathbf{x}_B = \vec{F}(\xi,\eta,0), \qquad \mathbf{x}_T = \vec{F}(\xi,\eta,1),$$

The six parametric surfaces defined in equation 7-2 have twelve compatible edges,

$$\mathbf{x}_{SW} = \vec{F}(0,0,\zeta), \ \mathbf{x}_{NW} = \vec{F}(1,0,\zeta), \ \mathbf{x}_{SE} = \vec{F}(0,1,\zeta), \ \mathbf{x}_{NE} = \vec{F}(1,1,\zeta),$$

$$\mathbf{x}_{BW} = \vec{F}(0,\eta,0),\ \mathbf{x}_{TW} = \vec{F}(0,\eta,1),\ \mathbf{x}_{BE} = \vec{F}(1,\eta,0),\ \mathbf{x}_{TE} = \vec{F}(1,\eta,1),$$

$$\mathbf{x}_{BS} = \vec{F}(\xi,0,0),\quad \mathbf{x}_{TS} = \vec{F}(\xi,0,1),\quad \mathbf{x}_{BN} = \vec{F}(\xi,1,0),\ \mathbf{x}_{TN} = \vec{F}(\xi,1,1),$$

and eight corners,

$$\mathbf{x}_{WBS} = \vec{F}(0,0,0),\ \mathbf{x}_{WST} = \vec{F}(0,0,1),\ \mathbf{x}_{WNT} = \vec{F}(0,1,0),\ \mathbf{x}_{WNT} = \vec{F}(0,1,1),$$

$$\mathbf{x}_{ESB} = \vec{F}(1,0,0),\quad \mathbf{x}_{EST} = \vec{F}(1,0,1),\ \mathbf{x}_{ENB} = \vec{F}(1,1,0),\quad \mathbf{x}_{ENT} = \vec{F}(1,1,1),$$

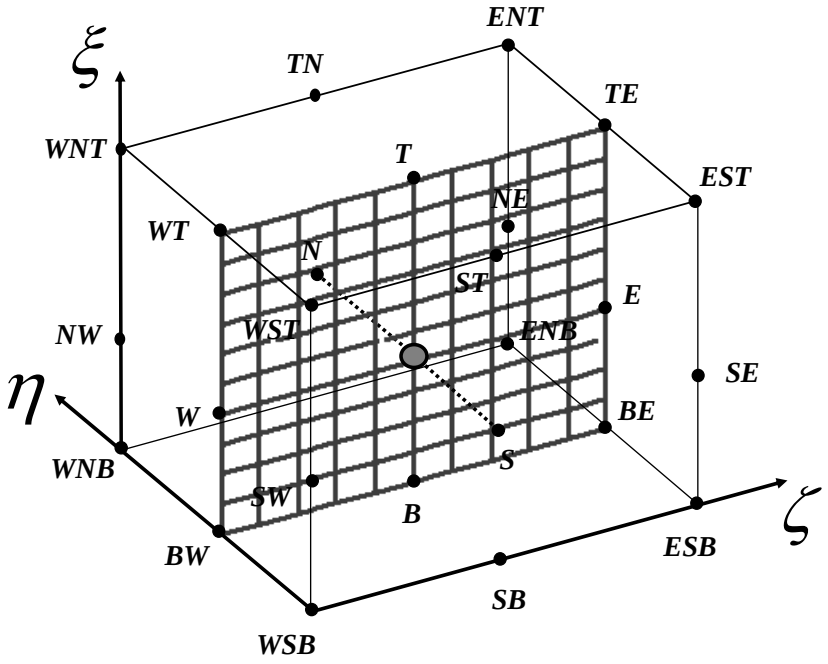

Figure 7-2. Computational grid used to compute 3D TFI mapping.

After $\vec{F}$ has been defined, an interpolating function $\mathbf{x}(\xi,\eta\zeta)$ can be constructed that will map the inside unit cube into *P* by extending equation7-3 into 3D (Fig 7-2):

$$\mathbf{x}(\xi,\eta,\zeta) = \begin{bmatrix} x(\xi,\eta,\zeta) \\ y(\xi,\eta,\zeta) \\ z(\xi,\eta,\zeta) \end{bmatrix} = \mathbf{x}_1 + \mathbf{x}_2 + \mathbf{x}_3 - \mathbf{x}_{12} - \mathbf{x}_{13} - \mathbf{x}_{23} + \mathbf{x}_{123} \qquad 7\text{-}4$$

where,

$\mathbf{x}_1 = (1-\xi)\mathbf{x}_W + \xi\mathbf{x}_E$, $\mathbf{x}_2 = (1-\eta)\mathbf{x}_S + \eta\mathbf{x}_N$,

$\mathbf{x}_3 = (1-\zeta)\mathbf{x}_B + \zeta\mathbf{x}_T$,

$\mathbf{x}_{12} = (1-\xi)(1-\eta)\mathbf{x}_{SW} + (1-\xi)\eta\mathbf{x}_{NW} + \xi(1-\eta)\mathbf{x}_{SE} + \xi\eta\mathbf{x}_{NE}$,

$\mathbf{x}_{13} = (1-\xi)(1-\zeta)\mathbf{x}_{BW} + (1-\xi)\zeta\mathbf{x}_{TW} + \xi(1-\zeta)\mathbf{x}_{BE} + \xi\zeta\mathbf{x}_{TE}$,

$\mathbf{x}_{23} = (1-\eta)(1-\zeta)\mathbf{x}_{BS} + (1-\eta)\zeta\mathbf{x}_{TS} + \eta(1-\zeta)\mathbf{x}_{BN} + \eta\zeta\mathbf{x}_{TN}$,

$$\begin{aligned}\mathbf{x}_{123} &= (1-\xi)(1-\eta)(1-\zeta)\mathbf{x}_{WBS} + (1-\xi)(1-\eta)\zeta\mathbf{x}_{WST} \\ &+ (1-\xi)\eta(1-\zeta)\mathbf{x}_{WNB} + (1-\xi)\eta\zeta\mathbf{x}_{WNT} + \xi(1-\eta)(1-\zeta)\mathbf{x}_{ESB} \\ &+ \xi(1-\eta)\zeta\mathbf{x}_{EST} + \xi\eta(1-\zeta)\mathbf{x}_{ENB} + \xi\eta\zeta\mathbf{x}_{ENT}\end{aligned}$$

In order to generate the vertices of a grid over the closed shape, the Cartesian domain *P*, an $N \times N \times N$ computational grid $\mathbf{x}_c = \left(i \cdot \frac{1}{N-1}, j \cdot \frac{1}{N-1}, k \cdot \frac{1}{N-1} \right)$ is defined and then mapped into *P* using equation 7-4.

Bibliography

[1] World Health Organization International Agency for Research on Cancer (June 2003). "World Cancer Report". Retrieved on 2008-02-03.

[2] World Health Organization (February 2006). "Fact sheet No. 297: Cancer". Retrieved on 2007-04-26

[3] Cancer Society, http://www.cancer.ca/.

[4] L. S. Wilson, D. E. Robinson and M. J. Dadd, "Elastography - The movement begins," *Physics in Medicine and Biology,* vol. 45, pp. 1409-1421, 2000.

[5] J. Ophir, I. Cespedes, H. Ponnekanti, Y. Yazdi and X. Li, "Elastography: A quantitative method for imaging the elasticity of biological tissues," *Ultrasonic Imaging,* vol. 13, pp. 111-134, 1991.

[6] A. R. Skovoroda, S. Y. Emelianov and M. O'Donnell, "Tissue elasticity reconstruction based on ultrasonic displacement and strain images," *IEEE Transactions on Ultrasonics, Ferroelectrics, and Frequency Control,* vol. 42, pp. 747-765, 1995.

[7] A. Samani and D. Plewes, "An inverse problem solution for measuring the elastic modulus of intact *ex vivo* breast tissue tumors," *Physics in Medicine and Biology,* vol. 52, pp. 1247-1260, 2007.

[8] R. Righetti, M. Righetti, A. T. Kumar, J. Ophir, , T. A. Krouskop, "The feasibility of estimating and imaging the mechanical behavior of poroelastic materials using axial strain elastography", *Physics in Medicine and Biology* 52 (11), art. no. 020, 2007, pp. 3241-3259.

[9] L. Gao, K. J. Parker, R. M. Lerner and S. F. Levinson, "Imaging of the elastic properties of tissue - A review," *Ultrasound in Medicine and Biology,* vol. 22, pp. 959-977, 1996.

[10] C. U. Devi, R. S. B. Chandran, R. M. Vasu and A. K. Sood, "Elastic property estimation using ultrasound assisted optical elastography through remote palpation-A simulation study," in 2006, *Proceedings of SPIE - The International Society for Optical Engineering*, 2006, 6164.

[11] A. Viidik, "Biomechanics and functional adaptation of tendons and joint ligaments," *Studies on the Anatomy and Function of Bone and Joints,* pp. 17-39, 1966

[12] Y. Fung C, “Biomechanics-Mechanical Properties of Living Tissues.” 1981, Springer Verlag Inc., New York.

[13] I. Cespedes, J. Ophir, H. Ponnekanti and N. Maklad, "Elastography: Elasticity imaging using ultrasound with application to muscle and breast *in vivo*," *Ultrasonic Imaging,* vol. 15, pp. 73-88, 1993.

[14] C. W. Washington and M. I. Miga. "Modality Independent Elastography: Preliminary Results.", Proceedings of SPIE - The International Society for Optical Engineering 5370 II, 2004, pp. 1380-1387.

[15] M. Drangova, Y. Zhu, B. Bowman, N. J. Pelc, **“**In vitro verification of myocardial motion tracking from phase-contrast velocity data”, *Magnetic Resonance Imaging* 16 (8), 1998, pp. 863-870

[16] A. Manduca, T. E. Oliphant, M. A. Dresner, J. L. Mahowald, S. A. Kruse, E. Amromin, J. P. Felmlee, J. F. Greenleaf and R. L. Ehman, "Magnetic resonance elastography: Non-invasive mapping of tissue elasticity," *Medical Image Analysis,* vol. 5, pp. 237-254, 2001.

[17] P. E. Barbone and A. A. Oberai, "Elastic modulus imaging: Some exact solutions of the compressible elastography inverse problem," *Physics in Medicine and Biology,* vol. 52, pp. 1577-1593, 2007.

[18] E. Konofagou and J. Ophir, "A new elastographic method for estimation and imaging of lateral displacements, lateral strains, corrected axial strains and Poisson's ratios in tissues," *Ultrasound in Medicine and Biology,* vol. 24, pp. 1183-1199, 1998.

[19] F. Kallel and M. Bertrand, "Tissue elasticity reconstruction using linear perturbation method," *IEEE Transactions on Medical Imaging,* vol. 15, pp. 299-313, 1996.

[20] A. R. Skovoroda, S. Y. Emelianov, M. A. Lubinski, A. P. Sarvazyan and M. O'Donnell, "Theoretical analysis and verification of ultrasound displacement and strain imaging," *IEEE Transactions on Ultrasonics, Ferroelectrics, and Frequency Control,* vol. 41, pp. 302-313, 1994.

[21] S. Y. Emelianov, A. R. Skovoroda, M. A. Lubinski and M. O'Donnell, "Reconstructive elasticity imaging," *Acoustical Imaging,* vol. 21, pp. 241-252, 1995.

[22] C. Sumi, A. Suzuki and K. Nakayama, "Estimation of shear modulus distribution in soft tissue from strain distribution," *IEEE Transactions on Biomedical Engineering,* vol. 42, pp. 193-202, 1995.

[23] M. M. Doyley, P. M. Meaney and J. C. Bamber, "Evaluation of an iterative reconstruction method for quantitative elastography," *Physics in Medicine and Biology,* vol. 45, pp. 1521-1540, 2000.

[24] D. B. Plewes, J. Bishop, A. Samani and J. Sciarretta, "Visualization and quantification of breast cancer biomechanical properties with magnetic resonance elastography," *Physics in Medicine and Biology,* vol. 45, pp. 1591-1610, 2000.

[25] A. Samani, I. Sack and D. B. Plewes, "Constrained nonlinear elasticity reconstruction technique for breast MRI elastography," *Proc. ISMRM 11th Annual Meeting,* pp. 773, 2003.

[26] H. Mehrabian and A. Samani, "An iterative hyperelastic parameters reconstruction for breast cancer assessment," in *Progress in Biomedical Optics and Imaging - Proceedings of SPIE*, 2008, 6916.

[27] A. Samani, J. Bishop and D. B. Plewes, "A constrained modulus reconstruction technique for breast cancer assessment," *IEEE Transactions on Medical Imaging,* vol. 20, pp. 877-885, 2001.

[28] A. R. Skovoroda, M. A. Lubinski, S. Y. Emelianov and M. O'Donnell, "Reconstructive elasticity imaging for large deformations," *IEEE Transactions on Ultrasonics, Ferroelectrics, and Frequency Control,* vol. 46, pp. 523-535, 1999.

[29] G. N. Maksym and J. H. T. Bates, "A distributed nonlinear model of lung tissue elasticity," *Journal of Applied Physiology,* vol. 82, pp. 32-41, 1997.

[30] P. S. Wellman, R. D. Howe, N. Dewagan, M. A. Cundari, E. Dalton and K. A. Kern, "Tactile imaging: A method for documenting breast masses," in 1999, pp. 1131. *Annual International Conference of the IEEE Engineering in Medicine and Biology - Proceedings*, 1999, 2, 1131

[31] G. Zhang, "Geometric and material nonlinearity in tensioned wires of an external fixator," *Clinical Biomechanics,* vol. 19, pp. 513-518, 2004.

[32] S. Srinivasan, R. Righetti and J. Ophir, "Trade-offs between the axial resolution and the signal-to-noise ratio in elastography," *Ultrasound in Medicine and Biology,* vol. 29, pp. 847-866, 2003.

[33] T. Varghese, J. Ophir and T. A. Krouskop, "Nonlinear stress-strain relationships in tissue and their effect on the contrast-to-noise ratio in elastograms," *Ultrasound in Medicine and Biology,* vol. 26, pp. 839-851, 2000.

[34] H. T. Liu, L. Z. Sun, G. Wang and M. W. Vannier, "Analytic modeling of breast elastography," *Medical Physics,* vol. 30, pp. 2340-2349, 2003.

[35] T. Hu and J. P. Desai, "Characterization of soft-tissue material properties: Large deformation analysis," in Lecture Notes in Computer Science (including subseries Lecture Notes in Artificial Intelligence and Lecture Notes in Bioinformatics) 2004, pp. 28-37.

[36] J. Sciarretta, A. Samani, J. Bishop and D. B. Plewes, "MR validation of soft tissue mimicing phantom deformation as modeled by nonlinear finite element analysis," *Medical Physics,* vol. 29, pp. 65-72, 2002.

[37] F. A. Duck, *Physical Properties of Tissues: A Comprehensive Reference Book.* London: Academic Press, 1990,

[38] T. A. Krouskop, T. M. Wheeler, F. Kallel, B. S. Garra and T. Hall, "Elastic moduli of breast and prostate tissues under compression," *Ultrasonic Imaging,* vol. 20, pp. 260-274, 1998.

[39] R. Q. Erkamp, S. Y. Emelianov, A. R. Skovoroda and M. O'Donnell, "Nonlinear elasticity imaging: Theory and phantom study," *IEEE Transactions on Ultrasonics, Ferroelectrics, and Frequency Control,* vol. 51, pp. 532-539, 2004.

[40] M. O'Donnell, S. Y. Emelianov, A. R. Skovoroda, M. A. Lubinski, W. F. Weitzel and R. C. Wiggins, "Quantitative elasticity imaging," in 1993, pp. 893-903. *Proceedings of the IEEE Ultrasonics Symposium*, 1993, 2, 893-903

[41] T. Varghese and J. Ophir, "Performance optimization in elastography: Multicompression with temporal stretching," *Ultrasonic Imaging,* vol. 18, pp. 193-214, 1996.

[42] R. Sinkus, S. Weiss, E. Wigger, J. Lorenzen, M. Dargatz and C. Kuhl, "Nonlinear elastic tissue properties of the breast measured by MR-elastography: Initial *in vitro* and *in vivo* results," *Proc. ISMRM 10th Annual Meeting,* pp. 33, 2002.

[43] P. A. L. S. Martins, R. M. N. Jorge and A. J. M. Ferreira, "A comparative study of several material models for prediction of hyperelastic properties: Application to silicone-rubber and soft tissues," *Strain,* vol. 42, pp. 135-147, 2006.

[44] N. H. Gokhale, P. E. Barbone and A. A. Oberai, "Solution of the nonlinear elasticity imaging inverse problem: The compressible case," *Inverse Problems,* vol. 24, 2008.

[45] G. A. Holzapfel and R. W. Ogden, *Biomechanics of Soft Tissue in Cardiovascular Systems.* New York: Springer Wien, 2003.

[46] G. A. Holzapfel, *Nonlinear Solid Mechanics: A Continuum Approach for Engineering.* Chichester; New York: Wiley, 2000.

[47] L. R. G. Treloar, "The elasticity of a network of long-chain molecules. I," *Transactions of the Faraday Society,* vol. 39, pp. 36-41, 1943. 1943.

[48] R. Ogden W, *Non-Linear Elastic Deformations.* Mineola, NY, USA: Dover Publications Inc., 1984.

[49] D. R. Veronda and R. A. Westmann, "Mechanical characterization of skin-Finite deformations," *Journal of Biomechanics,* vol. 3, pp. 111-122,IN9,123-124, 1970.

[50] H. M. Yin, L. Z. Sun, G. Wang and M. W. Vannier, "Modeling of elastic modulus evolution of cirrhotic human liver," *IEEE Transactions on Biomedical Engineering,* vol. 51, pp. 1854-1856, 2004.

[51] R. H. Byrd, R. B. Schnabel and G. A. Shultz, "Approximate Solution of the Trust Region Problem my Minimization Over Two-Dimensional Subspaces." *Mathematical Programming, Series B,* vol. 40, pp. 247-263, 1988.

[52] T. Steihaug, "The conjugate gradient method and trust regions in large scale optimization," *SIAM J. Numer. Anal.,* vol. 20, pp. 626-637, 1983.

[53] M. A. Branch, T. F. Coleman and Y. Li, "Subspace, interior, and conjugate gradient method for large-scale bound-constrained minimization problems," *SIAM Journal of Scientific Computing,* vol. 21, pp. 1-23, 1999.

[54] A. Samani, J. Bishop, C. Luginbuhl and D. B. Plewes, "Measuring the elastic modulus of *ex vivo* small tissue samples," *Physics in Medicine and Biology,* vol. 48, pp. 2183-2198, 2003.

[55] V. L. Rvachev, T. I. Sheiko, V. Shapiro and I. Tsukanov, "Transfinite interpolation over implicitly defined sets," *Technical Report SAL,* 2000.

[56] T. J. Horgan and M. D. Gilchrist, "Influence of FE model variability in predicting brain motion and intracranial pressure changes in head impact simulations," *International Journal of Crashworthiness,* vol. 9, pp. 401-418, 2004.

[57] M. I. Miga, "A new approach to elastography using mutual information and finite elements," *Physics in Medicine and Biology,* vol. 48, pp. 467-480, 2003.

[58] A. Samani and D. Plewes, "A method to measure the hyperelastic parameters of *ex vivo* breast tissue samples," *Physics in Medicine and Biology,* vol. 49, pp. 4395-4405, 2004.

[59] H. Mehrabian and A. Samani, " Constrained hyperelastic parameters reconstruction of PVA phantom undergoing large deformation," in *Progress in Biomedical Optics and Imaging - Proceedings of SPIE*, 2009, 7261

[60] H. Mehrabian, H. Karimi, A. Samani, " Accurate optical flow field estimation using mechanical properties of soft tissues," in *Progress in Biomedical Optics and Imaging - Proceedings of SPIE*, 2009, 7262

[61] P. Anandan, "A computational framework and an algorithm for the measurement of visual motion," *International Journal of Computer Vision,* vol. 2, pp. 283-310, 1989.

[62] B. K. P. Horn and B. G. Schunck, "Determining optical flow," *Artificial Intelligence,* vol. 17, pp. 185-203, 1981.

[63] J. Kim and T. Sikora, "Hybrid recursive energy-based method for robust optical flow on large motion fields," in *Proceedings - International Conference on Image Processing*, ICIP, 2005, 1, 129-132

CURRICULUM VITA

Name	Hatef Mehrabian
Post-Secondary Education and Degrees	Universoty of Tehran, Tehran, Tehran, Iran Sept 2002 - June 2006, B.A. The University of Western Ontario, London, Ontario, Canada Jan 2007 - Dec 2008, M.E.Sc.
Honors and Awards	Western Engineering Graduate Scholarship (WES) University of Western Ontario, London, ON, Canada Jan 2007 - Dec 2008
Related Work Experience	Teaching Assistant The University of Western Ontario Jan 2007 – Dec 2008

Publications

Journal Papers

H. Mehrabian and A. Samani, "Performance Evaluation of Several Hyperelastic Models in Reconstructing the Non-linear Behavior of Soft Tissues", to be submitted to the Journal of Physics in medicine and Biology

H. Mehrabian and A. Samani, "Soft Tissue Hyperelastic Parameter Reconstruction Technique for Breast Cancer Assessment", to be submitted to the Journal of Physics in medicine and Biology

Conference Papers

H. Mehrabian and A. Samani, " Constrained hyperelastic parameters reconstruction of PVA phantom undergoing large deformation," in Progress in Biomedical Optics and Imaging - Proceedings of SPIE, 2009, 7261

H. Mehrabian, H. Karimi, A. Samani, " Accurate optical flow field estimation using mechanical properties of soft tissues," in Progress in Biomedical Optics and Imaging - Proceedings of SPIE, 2009, 7262

H. Mehrabian and A. Samani, "An iterative hyperelastic parameters reconstruction for breast cancer assessment," in Progress in Biomedical Optics and Imaging - Proceedings of SPIE, 2008, 6916.

H. Mehrabian and P. Hashemi-Tari, "Pupil Boundary Detection for Iris Recognition Using Graph Cuts", Image and Vision Computing New Zealand (IVCNZ), December, 2007, Hamilton, New Zealand.

H. Mehrabian, A. Poursaberi, B. N. Araabi, "Feature Extraction for Iris Recognition Using Gabor Filters and Daubechies2 Wavelet Transform and Sensitivity Analysis", 4th Iranian Conference on Machine Vision and Image Processing (MVIP) conference, February 2007, Mashhad, Iran.

H. Mehrabian, A. Poursaberi, B. N. Araabi, "Iris boundary detection for iris recognition using Laplacian mask and Hough transform", 4th Iranian Conference on Machine Vision and Image Processing (MVIP) conference, February 2007, Mashhad, Iran.

A. Ashouri and **H. Mehrabian**, "Optimizing Fuzzy Controller for Reverse Pendulum System Using Genetic Algorithm". 2nd ECESYMP paper contest, Tehran, Iran, February 2006.